Spring 5-1-2020

Design and Fabrication of Biaxial Hyperbolic Metamaterials

Changkee Hong

Design and Fabrication of Biaxial Hyperbolic Metamaterials

A Thesis

Submitted to the Faculty

of

Rose-Hulman Institute of Technology

by

Changkee Hong

In Partial Fulfillment of the Requirements for the Degree

of

Master of Science in Optical Engineering

May 2020

ROSE-HULMAN INSTITUTE OF TECHNOLOGY

Final Examination Report

Changkee Hong — Name

Optical Engineering - Dual Degree — Graduate Major

Thesis Title **Design and Fabrication of Biaxial Hyperbolic Metamaterials**

DATE OF EXAM: **May 15, 2020**

EXAMINATION COMMITTEE:

	Thesis Advisory Committee	Department
Thesis Advisor:	Hossein Alisafaee	PHOE
	Azad Siahmakoun	PHOE
	Wonjong Joo	SNUST

PASSED X **FAILED** _____

ABSTRACT

Changkee Hong

M.S.O.E.

Rose-Hulman Institute of Technology

May 2020

Design and Fabrication of Biaxial Hyperbolic Metamaterials

Thesis Advisor: Dr. Hossein Alisafaee

This thesis describes a new method for fabrication of biaxial hyperbolic metamaterials (BHMMs) using layered structures consisting of oblique angle deposited (OAD) titanium dioxide (TiO_2) and copper (Cu). An oblique angle deposition (OAD) technique was utilized to deposit dielectric layer composed of nanocolumnar structures in order to provide biaxial property. The biaxial hyperbolic dispersion of the fabricated BHMM was characterized via profilometer and variable angle spectroscopic ellipsometry (VASE) measurements for wavelength between 381 nm and 894 nm. For the fabricated BHMM, a noticeable difference of 0.13 ± 0.001 between the in-plane permittivity components and dual epsilon-near-zero (ENZ) regions which are separated by 6.7 nm were observed. The experimental characterization results through both VASE and profilometer have been in good agreement with the predictions of effective medium approximation (EMA). The proposed fabrication method is efficient for rapid procedures to obtain BHMMs, and this potentially provides basis for further research in nanophotonics applications.

Keywords: Hyperbolic Metamaterials, Biaxial Hyperbolic Metamaterials, Oblique Angle Deposition, Glancing Angle Deposition, Effective Medium Approximation, Ellipsometry

The thesis is dedicated to my parents, Seonglok Hong and Misoon Jeong.

ACKNOWLEDGEMENTS

I would like to profoundly thank my thesis supervisor, Dr. Hossein Alisafaee. I appreciate his willingness to advise and discuss anything throughout the research. His guidance, insight and enthusiasm helped me to overcome all the hard moments during my research. I am also deeply thankful to Dr. Azad Siahmakoun who gave me a great opportunity of research internship to improve my research ability. Dr. Wonjong Joo at Seoul National University of Science and Technology have always supported me to complete this thesis.

Dr. Maarij Syed, Dr. Scott Kirkpatrick, Dr. Daniel Marincel and Brian Fair gave me great guidances for the fabrication steps of biaxial hyperbolic metamaterials in MiNDS fabrication facility, I am indebted to them as well. Moreover, I would also like thank Dr. Galen Duree, Pamela Hamilton, Roger Sladek, Ben Webster as well as all of the staff and faculty at Rose-Hulman Institute of Technology.

For my classmates Jake Joo and James Dilts, I deeply appreciate what we have done together on coursework and research.

Finally, I am truly grateful to my family in Republic of Korea for their blind faith and support until this honorable moment.

TABLE OF CONTENTS

Contents

LIST OF FIGURES

Figure **Page**

LIST OF TABLES

Table **Page**

LIST OF ABBREVIATIONS

BHMMs	Biaxial Hyperbolic Metamaterials
BOV	Bridging Oxygen Vacancies
BP	Black Phosphorus
DI Water	Deionized Water
EBPVD	Electron-Beam Physical Vapor Deposition
EM	Electro-Magnetic
EMA	Effective Medium Approximation
ENZ	Epsilon-Near-Zero
HMMs	Hyperbolic Metamaterials
MSE	Root Mean Squared Error
OAD	Oblique Angle Deposition
PVD	Physical Vapor Deposition
RCA	Radio Corporation of America
SPs	Surface Plasmons
SPPs	Surface Plasmon Polaritons
SE	Spectroscopic Ellipsometry
SEM	Scanning Electron Microscopy
TIR	Total Internal Reflection
VASE	Variable Angle Spectroscopic Ellipsometry

LIST OF SYMBOLS

English Symbols

A	Cauchy Parameter (Approximated Amplitude for Refractive Index)
a_i	Semiaxis in i-direction of Ellipsoidal Particles
a_j	Semiaxis in j-direction of Ellipsoidal Particles
a_k	Semiaxis in k-direction of Ellipsoidal Particles
B	Cauchy Parameter (Shape or Curvature of Refractive Index)
$\boldsymbol{B}$	Magnetic Flux Density
C	Ellipsometer Data ($\sin(2\Psi)\cos(\Delta)$)
C	Cauchy Parameter (Shape or Curvature of Refractive Index)
c_0	Speed of Light in Vacuum
C_a	$2\gamma\cos(\Delta)/D_a$
C_{ps}	$2\gamma_{ps}\cos(\Delta_{ps})/D_a$
C_{sp}	$2\gamma_{sp}\cos(\Delta_{sp})/D_a$
$\boldsymbol{D}$	Electric Flux Density
D_a	$(1+\gamma^2+\gamma_{ps}^2+\gamma_{sp}^2)$
$\boldsymbol{E}$	Electric Field
$\boldsymbol{E_0}$	Magnitude of Electric Field
$\boldsymbol{E}_{ext}$	External Electric Field
f	Fill Fraction of Constituent Material in the Composite
$\boldsymbol{H}$	Magnetic Field
$\boldsymbol{H_0}$	Magnitude of Magnetic Field
I_{+45°	Light Intensity of Linear Polarization at +45°
I_{-45°	Light Intensity of Linear Polarization at -45°
I_L	Light Intensity of Left-Circular Polarization
I_R	Light Intensity of Right-Circular Polarization

I_x	Light Intensity of Linear Polarization in the x-direction
I_y	Light Intensity of Linear Polarization in the y-direction
k	Wave Vector
$\tilde{k}$	Extinction Coefficient
k_0	ω/c_0
L	Lorentz Depolarization Factor
$\boldsymbol{M}$	Magnetization Density
$\tilde{n}$	Refractive Index
N	Ellipsometer Data ($\cos(2\Psi)$)
$\tilde{N}_{complex}$	Complex Refractive Index
N_a	$(1-\gamma^2-\gamma_{ps}^2-\gamma_{sp}^2)/D_a$
$n_{x,principal}$	Principal Refractive Index in x-direction
$n_{y,principal}$	Principal Refractive Index in y-direction
$n_{z,principal}$	Principal Refractive Index in z-direction
p	Filling Ratio of Metal in a Unit Cell
$\boldsymbol{P}$	Polarization Density
r	Position
r_p	Reflectivity of p-polarized Light
r_s	Reflectivity of s-polarized Light
S	Ellipsometer Data ($\sin(2\Psi)\sin(\Delta)$)
S_0	Total Light Intensity of $\mathrm{I}_x + I_y$
S_1	Total Light Intensity of $\mathrm{I}_x - I_y$
S_2	Total Light Intensity of $\mathrm{I}_{+45^\circ} - \mathrm{I}_{-45^\circ}$
S_3	Total Light Intensity of $\mathrm{I}_R - I_L$
S_a	$2\gamma\sin(\Delta)/D_a$
S_{ps}	$2\gamma_{ps}\sin(\Delta_{ps})/D_a$
S_{sp}	$2\gamma_{sp}\sin(\Delta_{sp})/D_a$
t	Time
T	Intensity Transmission

t_d	Thickness of Dielectric Layer
t_m	Thickness of Metal Layer
u	Any of Components of $\boldsymbol{E}$ or $\boldsymbol{H}$

Greek Symbol

α	Deposition Angle (Vapor Flux Angle)
α_{ps}	$2\gamma_{ps}/D_a$
α_{sp}	$2\gamma_{sp}/D_a$
β	Column Axis Angle
β_1	$(C_{sp}C_{ps}+S_{sp}S_{ps})D_a/2$
β_2	$(S_{sp}C_{ps}-C_{sp}S_{ps})D_a/2$
γ	$\tan\Psi$
γ_{ps}	$\tan\Psi_{ps}$
γ_{sp}	$\tan\Psi_{sp}$
Δ	Phase
Δn	In-plane Birefringence
ε	Electric Permittivity
ϵ	Electric Permittivity Tensor
ε_0	Electric Permittivity in Free Space
$\varepsilon_{complex}$	Complex Electric Permittivity
$\varepsilon_{constituent}$	Electric Permittivity of Constituent Material
ε_d	Electric Permittivity of Dielectric Layer
$\varepsilon_{effective}$	Effective Permittivity of Effective Medium
ε_{host}	Electric Permittivity of Host Material
ε_m	Electric Permittivity of Metal Layer
ε_{OADx}	Permittivity of OAD Dielectric in x-axis
ε_{OADy}	Permittivity of OAD Dielectric in y-axis

ε_{OADz}	Permittivity of OAD Dielectric in z-axis
ε_{xx}	Effective Permittivity in Principal x-axis
ε_{yy}	Effective Permittivity in Principal y-axis
ε_{zz}	Effective Permittivity in Principal z-axis
ζ_1	$(CC_{ps}+SS_{ps})D_a/2$
ζ_2	$(CS_{ps}-SC_{ps})D_a/2$
θ	Second Component of Euler Angles
κ	Screening Factor
λ	Wavelength
μ	Magnetic Permeability
μ_0	Magnetic Permeability in Free Space
ξ_1	$(CC_{sp}+SS_{sp})D_a/2$
ξ_2	$(CS_{sp}-SC_{sp})D_a/2$
ρ	r_p/r_s
ϕ	First Component of Euler Angles
ψ	Third Component of Euler Angles
Ψ	$\tan^{-1}(\rho/\mathrm{e}^{i\Delta})$
ω	Angular Frequency

1. INTRODUCTION

Optical metamaterials exhibit distinguished properties such as negative refraction which are unattainable with conventional media, and they have been widely investigated with the development of nanofabrication techniques [1, 2]. Especially, hyperbolic metamaterials (HMMs) have played a central role in nanophotonics since they can be used to access and manipulate the near-field of a light emitter or a light scatterer [1]. The excitation of coupled surface plasmons (SPs) enables HMMs to show this interesting feature [1]. SPs are collective oscillation of electrons at the boundary between metal and dielectric [1]. In the case of layered structure composed of subwavelength metal and dielectric layers, the boundaries between metal and dielectric are flat, and the metal surfaces allow propagating surface plasmon polaritons (SPPs) [1]. Electromagnetic (EM) field brings the excitation of coherent SPs and is bound to the plasmonic boundaries in the subwavelength layered structure [1]. This enables a collective response which can be interpreted as hyperbolic dispersion relation through Effective Medium Approximation (EMA) [1].

HMMs have been widely investigated to use as metamaterials for partial focusing of radiation [3], metamaterials nanolens [4], nanowire-based broadband HMM for nanophotonic chips and metamaterial-based flat lenses [5], HMM cavities with dipole excitation for quantum optics and on-chip quantum computing [6, 7], photonic spin Hall effect in HMMs for spin-dependent beam splitters [8], semiconductor HMMs based on Si:InAs/AlSb for thermophotovoltaics and thermal emission management [9], and nano-grooved HMMs for fast and efficient photon collection [10]. Furthermore, applications of HMMs exceeds beyond nanophotonics realm, covering such as Unruh effect [11], magneto-optical effects [12], generation and focusing of terahertz photons [13, 14], hyperlens [15, 16], and nanolithography [4].

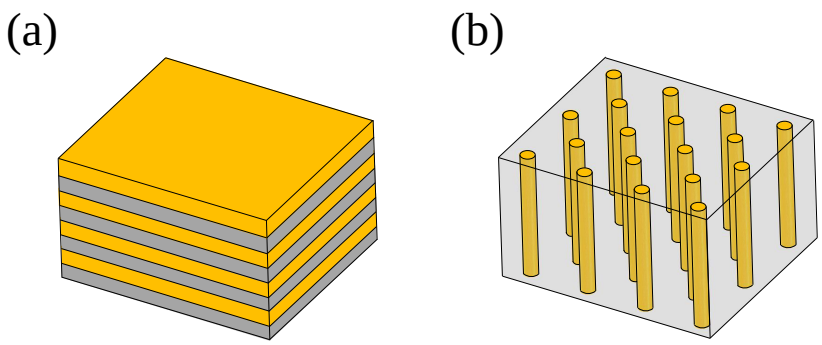

Figure 1.1: Schematics of metamaterials made of (a) stack of metallic (gold) and dielectric (grey) layers and (b) metallic nanowires (gold) embedded in a dielectric host (grey). Reproduced from Ref. [1].

It is interesting that HMMs have hyperbolic dispersion relation which can act both metallic and dielectric as a function of light propagation direction [1]. Theoretically, the structure dimensions of HMMs should be much smaller than incident wavelength, so the dimension of unit cell should be under 100 nm for visible wavelength spectrum in order to apply effective medium approximation (EMA) for design purposes [1].

Conventional HMMs are made of either a subwavelength stack of alternating metallic and dielectric layers or a lattice of metallic nanowires embedded in a dielectric host (Fig. 1.1) [1]. While fabrication of nanowires is quite complex since it needs extremely high aspect ratio, deposition of stack of layers is relatively simple [1]. Therefore, most of the experimental investigations have been focused on layered HMMs with normal deposition of materials due to its simplicity of fabrication [16–19], however, HMMs with biaxial constituent materials has scarcely been studied. The biaxial HMMs (BHMMs) which have asymmetric hyperbolic dispersion are attractive for vortex beam generation carrying an orbital angular momentum [20] and for the spin-controllable excitation of surface waves [21].

Although BHMMs have great potential to be utilized in such applications, most of BHMMs

have been investigated only in theoretical predictions [22] or in finite-element simulations for such interesting applications. This indicates that the major challenge remains in the fabrication of BHMMs. Taking this into account, fabrication and analysis of BHMMs will be covered throughout this thesis along with special technique called oblique angle deposition (OAD) which enables the BHMMs to have birefringent characteristics. S. Wang et al. had previously measured birefringence of OAD titanium dioxide (TiO_2) as a function of deposition angle [23], and they figured out the maximum birefringence of OAD TiO_2 occured at deposition angle between 65° and 70°. Therefore, OAD TiO_2 deposition with 70° was utilized to fabricate BHMM. An example application of OAD TiO_2 is the polarizing beam splitter which has been introduced by our group for the separation of two states of polarization [24]. The previous successful research on OAD TiO_2 led the researcher to further research on the application of OAD TiO_2 to BHMMs. To the best of our knowledge, this research would be the first time for the fabrication of BHMMs in this approach. Designed BHMM was made of a single layer of copper (Cu) and OAD TiO_2 at subwavelength scale in order to apply effective medium approximation (EMA) to extract hyperbolic dispersion relation of the BHMM. Among various methods to measure the permittivity tensor of HMMs, including total internal reflection (TIR) ellipsometry [25] and spectroscopic ellipsometry (SE) [26, 27], SE has strengths on its simple and quick measurement. Fabricated BHMM was characterized via variable angle spectroscopic ellipsometry (VASE) to extract permittivity tensors in x-, y-, z-directions. Theoretical predictions through EMA and measurement results of both VASE and profilometer were compared for experimental validity. Fabrication of BHMMs using OAD technique and measurement via VASE provide relatively rapid and efficient way to achieve such devices, and may encourage further research on applications of BHMMs.

Chapter 2 provides the backgrounds for design, fabrication and characterization of BHMM

including Maxwell's equations, wave equation, refractive index, permittivity, anisotropic media, hyperbolic metamaterials, effective medium approximation, oblique angle deposition and ellipsometry. Chapter 3 presents design procedures for the fabrication of BHMMs. Chapter 4 describes the fabrication process of BHMMs step by step using Cu and OAD TiO_2. RCA (Radio Corporation of America) clean, quick clean, e-beam physical vapor deposition will be covered. Chapter 5 explains experimental characterization including ellipsometric measurements and profilometer measurements. Chapter 6 includes the discussions on comparison between theoretical simulation and experimental results. Chapter 7 includes the conclusions of the thesis, and proposes future research to advance research on BHMMs such as simulation of their optical behavior and increasing the number of unit cell to supports high-k states.

2. THEORY AND BACKGROUND

2.1. Maxwell's Equations

James Clerk Maxwell mathematically integrated relations between electric field and magnetic field into four simple equations: Maxwell's Equations, which are the basic in electromagnetic theory of optics. There are terms for electric field $\boldsymbol{E}$, magnetic field $\boldsymbol{H}$, electric flux density $\boldsymbol{D}$, magnetic flux density $\boldsymbol{B}$, polarization density $\boldsymbol{P}$ and magnetization density $\boldsymbol{M}$ [28]. Plane wave can be expressed as [28]

$$\boldsymbol{E} = \boldsymbol{E_0} e^{i(\omega t - \boldsymbol{k}\cdot\boldsymbol{r})}, \tag{2.1}$$

$$\boldsymbol{H} = \boldsymbol{H_0} e^{i(\omega t - \boldsymbol{k}\cdot\boldsymbol{r})}, \tag{2.2}$$

where $\boldsymbol{E}_0$ is magnitude of electric field, $\boldsymbol{H}_0$ is magnitude of magnetic field, λ is wavelength, $\boldsymbol{k}$ is wavevector which is $2\pi/\lambda$, $\boldsymbol{r}$ is position, ω is angular frequency and t is time. The equations related to electric, magnetic flux densities and electric, magnetic fields are described as [28]

$$\boldsymbol{D} = \varepsilon_0 \boldsymbol{E} + \boldsymbol{P}, \tag{2.3}$$

$$\boldsymbol{B} = \mu_0 \boldsymbol{H} + \mu_0 \boldsymbol{M}, \tag{2.4}$$

where $\varepsilon_0 \approx (1/36\pi) \times 10^{-9}\ F/m$ is electric permittivity in free space and $\mu_0 = (4\pi) \times 10^{-7}\ H/m$ is magnetic permeability in free space. The four Maxwell's equations in free space in differential forms are [28]

$$\nabla \times \boldsymbol{H} = \varepsilon_0 \frac{\partial \boldsymbol{E}}{\partial t}, \tag{2.5}$$

$$\nabla \times \boldsymbol{E} = -\mu_0 \frac{\partial \boldsymbol{H}}{\partial t}, \tag{2.6}$$

$$\nabla \cdot \boldsymbol{E} = 0, \tag{2.7}$$

$$\nabla \cdot \boldsymbol{H} = 0. \tag{2.8}$$

2.2. Wave Equation

A wave equation is a necessary condition for $\boldsymbol{E}$ and $\boldsymbol{H}$ to satisfy Maxwell's equations [28]. The wave equation in free space is described as [28]

$$\nabla^2 u - \frac{1}{c_0^2}\frac{\partial^2 u}{\partial t^2} = 0, \tag{2.9}$$

where u represents any of components of $\boldsymbol{E}$ or $\boldsymbol{H}$ and the speed of light in vacuum,

$$c_0 = \frac{1}{\sqrt{\varepsilon_0 \mu_0}} \approx 3 \times 10^8 m/s. \tag{2.10}$$

Superposition could be conducted since both Maxwell's equations and wave equation are linear [28].

2.3. Refractive Index and Permittivity

In general, complex refractive index is defined as [29]

$$\tilde{N}_{complex} = \tilde{n} + i\tilde{k} = \sqrt{\mu \varepsilon_{complex}}, \tag{2.11}$$

where $\tilde{n}$ is refractive index, $\tilde{k}$ is extinction coefficient and μ is magnetic permeability. Both of $\tilde{n}$ and $\tilde{k}$ are called optical constants [29]. $\tilde{k}$ could be ignored for lossless materials such as dielectric and μ can have value of 1 for non-magnetic materials [29]. Complex electric permittivity is defined as [29]

$$\varepsilon_{complex} = \varepsilon_1 + i\varepsilon_2 = (\tilde{n} + i\tilde{k})^2, \tag{2.12}$$

and this relation yields

$$\varepsilon_1 = \tilde{n}^2 - \tilde{k}^2, \tag{2.13}$$

$$\varepsilon_2 = 2\tilde{n}\tilde{k}. \tag{2.14}$$

2.4. Oblique Angle Deposition (OAD)

Oblique angle deposition (OAD) method allows fabrication of nanostructured columnar structures. Such nanocolumnar structures have birefringence characteristics in the plane of the layer [30]. In the OAD process, the substrate is tilted with respect to normal deposition direction [30]. Then, atomic vapor is condensed on the substrate and forms microscopic nuclei [30]. Since vapor cannot be condensed immediately behind the nuclei, as a result, a small shadow region forms behind the nuclei and causes growth of nanocolumns with voids among them [30]. Fig. 2.1 (a) and (b) represents deposition angle α (vapor flux angle) and column axis angle β. Fig. 2.1 (c) and (d) demonstrate biaxial index ellipsoid of the OAD films [30]. Based on Eq. (2.23), an index ellipsoid of the OAD films which have three different principal indices n_i, n_j, and n_k can be described as

$$\frac{i^2}{{n_i}^2} + \frac{j^2}{{n_j}^2} + \frac{k^2}{{n_k}^2} = 1. \tag{2.15}$$

There are two empirical equations for the estimation of column axis angle as a function of deposition angle: tangent rule and cosine rule. The tangent rule is defined as [23, 31]

$$\tan\beta = 0.5\,\tan\alpha. \tag{2.16}$$

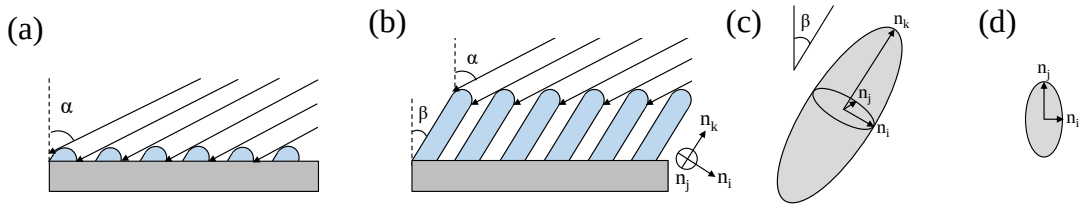

Figure 2.1: A schematic of OAD process. (a) atomic vapor is condensed on the substrate with deposition angle α (vapor flux angle) and forms nuclei with shadow region just behind the nuclei and (b) nanocolumnar structures are grown with an column axis angle β with the i-, j-, k-principal axes. (c) The OAD nanocolumnar structures leads to biaxial anisotropic ellipsoid at an angle of β with a refractive index tensor with three distinct principal indices n_i, n_j, and n_k and (d) its top view from k-axis of the ellipsoid (c). Reproduced from Ref. [30].

The cosine rule is defined as [23, 32, 33]

$$\beta = \alpha - \arcsin\left(\frac{1-\cos\alpha}{2}\right). \tag{2.17}$$

Among them, the cosine rule could calculate the column axis angle β more successfully if deposition angle α is higher than 70° [23]. Biaxial HMM which will be designed in Chap. 3 requires higher in-plane birefringence in order to obtain bigger difference in effective permittivities ε_{xx} and ε_{yy} (Eqs. (2.29)-(2.30)). The maximum in-plane birefringence Δn of OAD TiO_2 is known as 0.065 at deposition angle α of 70° [23]. Therefore, the cosine rule is used to estimate column axis angle in our BHMM design. Based on the cosine rule (Eq. (2.17)), the column axis angle is calculated as 51°.

2.5. Anisotropic Media

Electric flux density $\boldsymbol{D}$ in a linear anisotropic dielectric medium is described as [28]

$$D_i = \sum_j \varepsilon_{ij} E_j \ (\boldsymbol{D} = \boldsymbol{\epsilon}\boldsymbol{E}), \tag{2.18}$$

where $i, j = 1, 2, 3$ for x, y, z components. From the above equation, electric permittivity tensor of second rank $\boldsymbol{\epsilon}$ which is a 3×3 matrix can be achieved. For more details, Eq. (2.18) is expanded to

$$\begin{aligned} D_x &= \varepsilon_{11}E_x + \varepsilon_{12}E_y + \varepsilon_{13}E_z, \\ D_y &= \varepsilon_{21}E_x + \varepsilon_{22}E_y + \varepsilon_{23}E_z, \\ D_z &= \varepsilon_{31}E_x + \varepsilon_{32}E_y + \varepsilon_{33}E_z, \end{aligned} \tag{2.19}$$

which can be converted to matrix form as

$$\begin{pmatrix} D_x \\ D_y \\ D_z \end{pmatrix} = \begin{pmatrix} \varepsilon_{11} & \varepsilon_{12} & \varepsilon_{13} \\ \varepsilon_{21} & \varepsilon_{22} & \varepsilon_{23} \\ \varepsilon_{31} & \varepsilon_{32} & \varepsilon_{33} \end{pmatrix} \begin{pmatrix} E_x \\ E_y \\ E_z \end{pmatrix}. \tag{2.20}$$

Off-diagonal elements of permittivity tensor $\boldsymbol{\epsilon}$ can be zero after matrix diagonalization. The diagonalized permittivity tensor $\boldsymbol{\epsilon}$ is

$$\boldsymbol{\epsilon} = \begin{pmatrix} \varepsilon_{xx} & 0 & 0 \\ 0 & \varepsilon_{yy} & 0 \\ 0 & 0 & \varepsilon_{zz} \end{pmatrix}. \tag{2.21}$$

Based on Eq. (2.21), principal axes can be defined as $x_{principal}$, $y_{principal}$ and $z_{principal}$. Principal refractive indices $n_{x,principal}$, $n_{y,principal}$ and $n_{z,principal}$ can be achieved using the permittivities ε_1, ε_2 and ε_3 in Eq. (2.21) as

$$n_{x,principal} = \sqrt{\varepsilon_{xx}/\varepsilon_0}, \quad n_{y,principal} = \sqrt{\varepsilon_{yy}/\varepsilon_0}, \quad n_{z,principal} = \sqrt{\varepsilon_{zz}/\varepsilon_0}, \tag{2.22}$$

where ε_0 is permittivity of free space. In the coordinate system with principal axes, index ellipsoid is defined as

$$\frac{x^2}{{n_{x,principal}}^2} + \frac{y^2}{{n_{y,principal}}^2} + \frac{z^2}{{n_{z,principal}}^2} = 1. \tag{2.23}$$

Isotropic, uniaxial and biaxial materials can be determined based on the three principal refractive indices $n_{x,principal}$, $n_{y,principal}$ and $n_{z,principal}$ [28]. Isotropic materials have all the same three principal refractive indices. Uniaxial materials have two same principal refractive indices among the three, and these are not equal to the other. Biaxial materials have all different three principal refractive indices.

2.6. Effective Medium Approximation

Effective Medium Approximation (EMA) is regularly used to model composite materials into one macroscopic homogeneous material in order to obtain an acceptable result using properties of the constituent materials. A condition to apply EMA is the thickness of each layer should be much smaller than the wavelength of incident light (Fig. 2.2) [34].

There are two common EMA models: Maxwell-Garnett EMA and Bruggeman EMA. Bruggeman EMA has a specialty in modeling percolation over Maxwell-Garnett EMA [36]. For example, Bruggeman EMA was applied to model metal-insulator transition which was treated as percolation [37]. The metal-insulator transition is the process of growth of metallic domain on insulating domain, and it forms inhomogeneous composite which contains metallic and insulating domains [37]. Maxwell-Garnett EMA describes the bulk effective permittivity of a composite material which is composed of host material and inclusion material [34]. An assumption posed on Maxwell-Garnett EMA is low-volume fraction of the conductive materials [36]. The Maxwell-Garnett EMA can specifically be applied to metallic/dielectric layered structure where metal can be regarded as inclusion and dielectric can be considered as host material [34]. Since design of biaxial HMMs (See details in Chap. 3) has small fraction (20%) of metal layer over dielectric layer, the Maxwell-Garnett EMA would be applied for modeling. Maxwell-Garnett EMA with shape

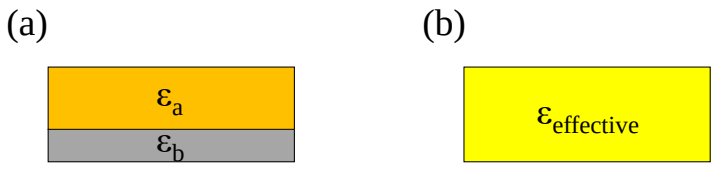

Figure 2.2: (a) Two layers of ε_a and ε_b which are much smaller than the wavelength of incident light can be regarded as (b) one effective medium with $\varepsilon_{effective}$. Reproduced from Ref. [35].

factors is defineds as [34]

$$\frac{\varepsilon - \varepsilon_{host}}{\varepsilon + \kappa\varepsilon_{host}} = f\frac{\varepsilon_{constituent} - \varepsilon_{host}}{\varepsilon_{constituent} + \kappa\varepsilon_{host}}, \tag{2.24}$$

where ε_{host} is permittivity of host material, $\varepsilon_{constituent}$ is permittivity of constituent material which is not host material, f is filling fraction of constituent material in the composite, and κ is screening factor determined by shape and orientation of the inclusions. The screening factor κ is related to Lorentz depolarization factor L as [34]

$$\kappa = (1-L)/L. \tag{2.25}$$

The Lorentz depolarization factor can be described as [34]

$$L_i = \int_0^\infty \frac{a_i a_j a_k ds}{2(s+{a_i}^2)^{3/2}(s+{a_j}^2)^{1/2}(s+{a_k}^2)^{1/2}}, \tag{2.26}$$

where a_i, a_j, and a_k are semiaxes of ellipsoidal particles. κ screening factor will be infinity when L depolarization factor is near zero for perpendicular direction to surface normal, and κ screening factor will be zero when L depolarization factor is one for parallel direction to surface normal (Fig. 2.3) [38].

For uniaxial HMMs composed of multiple layers of metal and dielectric, L depolarization factor of zero is put into Eq. (2.24) for x- and y-directions (perpendicular direction to surface

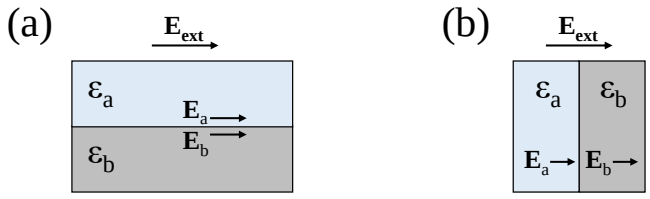

Figure 2.3: Cross-sections of a layered structure with (a) the parallel configuration of no screening charges (depolarization factor = 1) and (b) the perpendicular configuration of maximum screening charges (depolarization factor = 0) with respect to the external electric field E_{ext}. Reproduced from Ref. [38].

normal), and L depolarization factor of one is put into Eq. (2.24) for z-direction (parallel direction to surface normal) yield [1, 39]

$$\varepsilon_{xx} = \varepsilon_{yy} = p \cdot \varepsilon_m + (1-p) \cdot \varepsilon_d, \tag{2.27}$$

$$\varepsilon_{zz} = \left(\frac{p}{\varepsilon_m} + \frac{1-p}{\varepsilon_d} \right)^{-1}, \tag{2.28}$$

where ε_d is permittivity of dielectric, ε_m is permittivity of metal, and filling ratio $p = t_m/(t_m+t_d)$ is volume ratio of metal in a unit cell where t_d is thickness of dielectric layer and t_m is thickness of metal layer. For the BHMM which will be designed using isotropic Cu layer and biaxial oblique angle deposited (OAD) TiO_2 layer, the components of the permittivity tensor of OAD dielectric in x-, y-, z-directions are ε_{OADx}, ε_{OADy}, ε_{OADz}. The effective permittivity tensors of BHMM in x-, y-, z-directions can be expressed as [22, 39, 40]

$$\varepsilon_{xx} = \frac{\varepsilon_m \cdot p + \varepsilon_{OADx}}{p+1}, \tag{2.29}$$

$$\varepsilon_{yy} = \frac{\varepsilon_m \cdot p + \varepsilon_{OADy}}{p+1}, \tag{2.30}$$

$$\varepsilon_{zz} = \frac{p+1}{\frac{p}{\varepsilon_m} + \frac{1}{\varepsilon_{OADz}}}. \tag{2.31}$$

Fig. 2.4 describes permittivities of OAD TiO_2 in x-, y-, z-directions and permittivity of Cu. Although an index ellipsoid of OAD film described in Fig. 2.1c is tilted with an column axis angle β, we will extract optical constants and permittivities of OAD TiO_2 in laboratory frame of x-, y-, z-directions in order to apply the permittivities into Eqs. (2.29)-(2.31). Extraction of optical constants and permittivities of OAD TiO_2 in laboratory frame will be explained in Sec. 5.1.2.

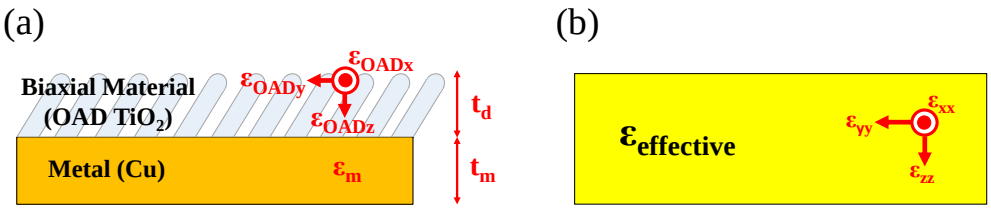

Figure 2.4: (a) A schematic of BHMM with permittivities of OAD TiO_2 in x-, y-, z-directions and permittivity of Cu and (b) its effective medium analyzed by EMA with effective permittivities in x-, y-, z-directions.

2.7. Hyperbolic Metamaterials (HMMs)

The plane wave expression at Eqs. (2.1) and (2.2) are inserted to two curl Maxwell's equation in free space at Eqs. (2.5) and (2.6). Then, two equations can be obtained as

$$\boldsymbol{k} \times \boldsymbol{E} = \omega \mu_0 \boldsymbol{H}, \tag{2.32}$$

$$\boldsymbol{k} \times \boldsymbol{H} = -\omega \epsilon \boldsymbol{E}. \tag{2.33}$$

Eigenvalue equation could be obtained after put Eq. (2.32) into Eq. (2.33) as

$$\boldsymbol{k} \times (\boldsymbol{k} \times \boldsymbol{E}) + \omega^2 \mu_0 \epsilon \boldsymbol{E} = 0, \tag{2.34}$$

which could be expanded in matrix form as

$$\begin{pmatrix} {k_0}^2 \varepsilon_{xx} - {k_y}^2 - {k_z}^2 & k_x k_y & k_x k_z \\ k_x k_y & {k_0}^2 \varepsilon_{yy} - {k_x}^2 - {k_z}^2 & k_y k_z \\ k_x k_z & k_y k_z & {k_0}^2 \varepsilon_{zz} - {k_x}^2 - {k_y}^2 \end{pmatrix} \begin{pmatrix} E_x \\ E_y \\ E_z \end{pmatrix} = 0, \tag{2.35}$$

where $k_0 = \omega / c_0$ is the magnitude of wavevector.

For uniaxial media ($\varepsilon_{xx} = \varepsilon_{yy} \neq \varepsilon_{zz}$) with optical axis in z-direction, nontrivial solutions to Eq. (2.35) yield dispersion relation as

$$\left({k_x}^2 + {k_y}^2 + {k_z}^2 - \varepsilon_{xx} {k_0}^2 \right) \left(\frac{{k_x}^2 + {k_y}^2}{\varepsilon_{zz}} + \frac{{k_z}^2}{\varepsilon_{xx}} - {k_0}^2 \right) = 0. \tag{2.36}$$

In Eq. (2.36), the first term describes waves polarized in the x-y plane (ordinary or TE wave) and second term explains waves polarized in an optical axis plane (extraordinary or TM wave) [1]. Isotropic media with $0 < \varepsilon_{xx} = \varepsilon_{yy} = \varepsilon_{zz}$ have bounded isofrequency surface (Fig. 2.5a). Anisotropic media with $0 < \varepsilon_{xx} = \varepsilon_{yy} < \varepsilon_{zz}$ have elongated bounded isofrequency surface (Fig. 2.5b). Hyperbolic dispersion relation for extraordinary polarization in uniaxial media can be obtained if either ε_{xx} or ε_{zz} is negative. Materials having the hyperbolic dispersion relation are called hyperbolic metamaterials (HMMs). Two types of HMMs exist: Type I ($\varepsilon_{xx} > 0$, $\varepsilon_{zz} < 0$) which has a two-fold hyperboloid (Fig. 2.5c) and Type II ($\varepsilon_{xx} < 0$, $\varepsilon_{zz} > 0$) has a one-sheet hyperboloid (Fig. 2.5d) [1].

For biaxial hyperbolic metamaterials (BHMMs), hyperbolic dispersion relations could be obtained through Eq. (2.35) with three cases: $k_x = 0$, $k_y = 0$ and $k_z = 0$. Two types of biaxial

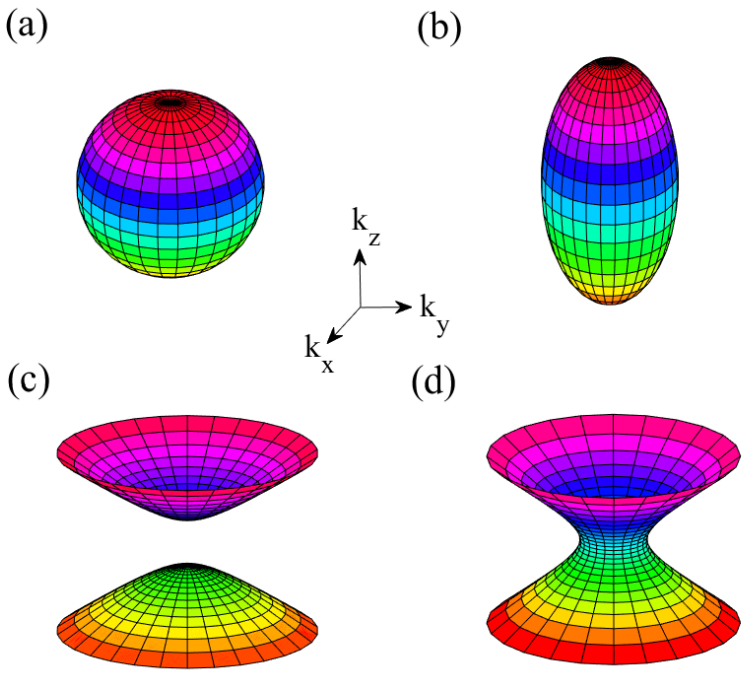

Figure 2.5: Isofrequency surface of (a) isotropic media ($0 < \varepsilon_{xx} = \varepsilon_{yy} = \varepsilon_{zz}$), (b) anisotropic media ($0 < \varepsilon_{xx} = \varepsilon_{yy} < \varepsilon_{zz}$), uniaxial HMMs with (c) Type I ($\varepsilon_{xx}>0$, $\varepsilon_{zz}<0$) and (d) Type II ($\varepsilon_{xx}<0$, $\varepsilon_{zz}>0$) hyperbolic dispersions.

hyperbolic metamaterials (BHMMs) are defined as: Type I BHMMs ($\varepsilon_{xx} > 0$, $\varepsilon_{yy} > 0$, $\varepsilon_{zz} < 0$, $\varepsilon_{xx} \neq \varepsilon_{yy}$) which have an asymmetric two-fold hyperboloid (Fig. 2.6) and Type II BHMMs ($\varepsilon_{xx} < 0$, $\varepsilon_{yy} < 0$, $\varepsilon_{zz} > 0$, $\varepsilon_{xx} \neq \varepsilon_{yy}$) which have an asymmetric one-sheet hyperboloid (Fig. 2.7). MATLAB codes for calculation of asymmetric hyperbolic dispersion relations of BHMMs are described in Appendix. A.1.

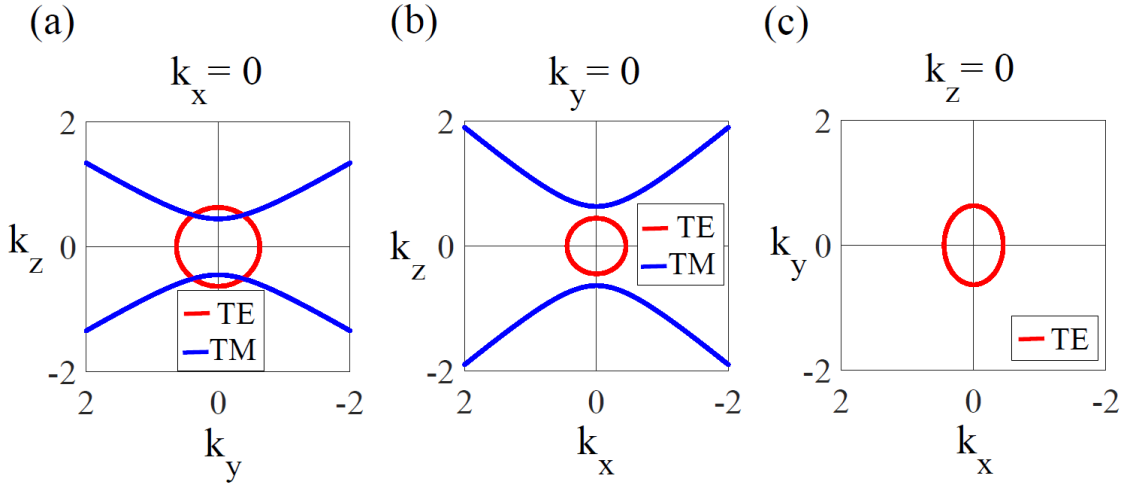

Figure 2.6: Isofrequency surface of Type I BHMMs ($\varepsilon_{xx} > 0$, $\varepsilon_{yy} > 0$, $\varepsilon_{zz} < 0$, $\varepsilon_{xx} \neq \varepsilon_{yy}$) with ε_{xx} = 0.4, ε_{yy} = 0.2, ε_{zz} = -0.5: (a) its view from k_x-axis, (b) k_y-axis and (c) k_z-axis.

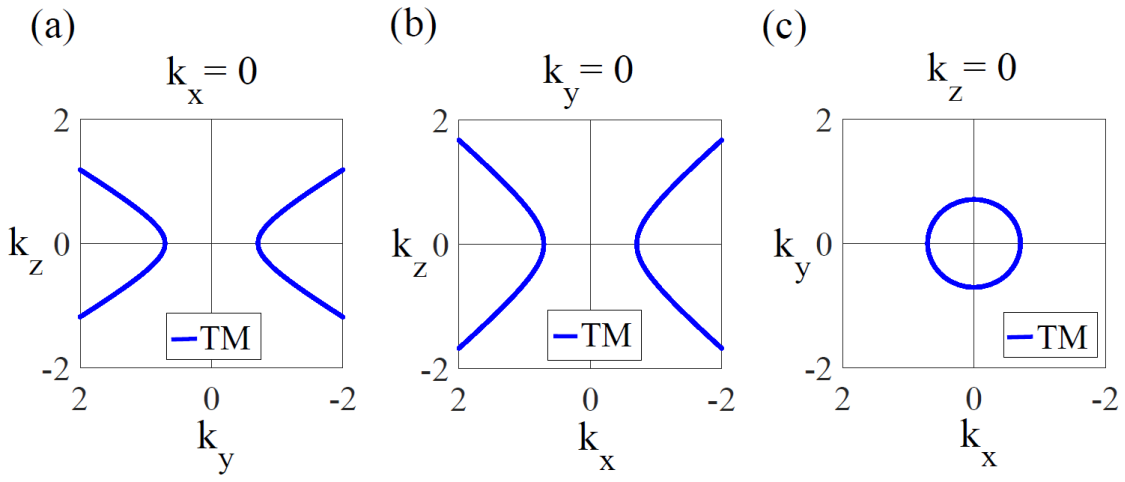

Figure 2.7: Isofrequency surface of Type II BHMMs ($\varepsilon_{xx} < 0$, $\varepsilon_{yy} < 0$, $\varepsilon_{zz} > 0$, $\varepsilon_{xx} \neq \varepsilon_{yy}$) with ε_{xx} = -0.4, ε_{yy} = -0.2, ε_{zz} = 0.5: (a) its view from k_x-axis, (b) k_y-axis and (d) k_z-axis.

2.8. Ellipsometry

Ellipsometry is non-destructive optical measurement system which can mainly extract optical constants and thickness of thin films. The polarized beam is illuminated onto the sample, and the change in polarization state of the beam caused by reflection or transmission will be analyzed via the system (Fig. 2.8) [41]. The change in polarization state is characterized as [41]

$$\tan(\Psi)e^{i\Delta} = \rho = \frac{r_p}{r_s}, \tag{2.37}$$

where r_p is reflectivity for p-polarized light, r_s is reflectivity for s-polarized light, $\tan(\Psi)$ is magnitude of the reflectivity ratio, and Δ is phase.

Ellipsometry model fitting process will be conducted through N, C, and S. The N, C, and S are the non-zero elements of the isotropic Mueller matrix, and are related to Ψ and Δ. The N, C, and S have strengths that the values are always defined and bounded between -1 and 1, and are linearly related to the intensity harmonics measured by ellipsometry [41].

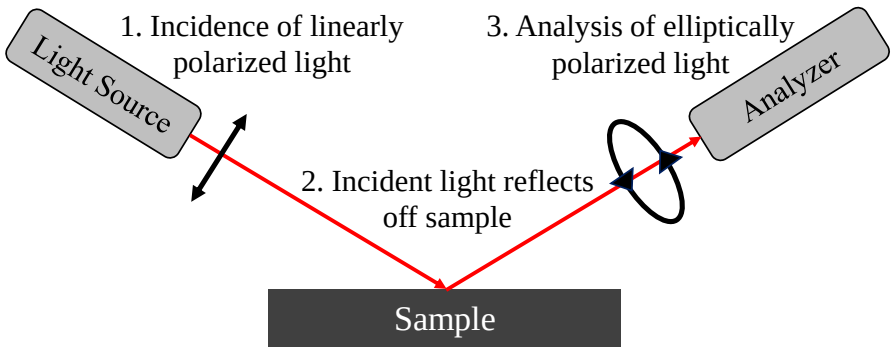

Figure 2.8: A schematic of ellipsometry measurement process with x-, y-, z-axes of laboratory frame of reference. Incident linearly polarized light reflects off the sample, and changed polarization status such as elliptical polarization is measured via detector. Reproduced from Ref. [41]

Root Mean Squared Error (MSE) in the ellipsometry model is defined as

$$MSE = \sqrt{\frac{1}{3n-m}\sum_{i=1}^{n}[(N_{R_i}-N_{G_i})^2+(C_{R_i}-C_{G_i})^2+(S_{R_i}-S_{G_i})^2]} \times 1000, \tag{2.38}$$

where n is number of wavelengths, m is number of fit parameters, parameters subscripted with R are measured data, and parameters subscripted with G are model generated data. Lower MSE value means better fit between measured and model generated SE data.

Cauchy dispersion relation is described as

$$n(\lambda) = A + \frac{B}{\lambda^2} + \frac{C}{\lambda^4}, \tag{2.39}$$

where A is approximate amplitude for refractive index, B and C are for shape or curvature of refractive index as a function of wavelengths. Transparent films, such as dielectrics, are analyzed mostly via Cauchy model [41]. Biaxial dielectric films such as OAD TiO_2 also could be analyzed via Cauchy model in x-, y-, z-directions, and biaxial characteristics (optical constants) with the tilted optical axes can be extracted using three Euler angle terms (ϕ, θ, and ψ) which are to rotate the orientation of optical axes relative to the ellipsometer measurement orientation Fig. 2.9 [41]. In case the directions (angles) of optical axes are known, VASE would yield better results with the Euler angles.

(a) φ: Rotation of x and y axes about z axis

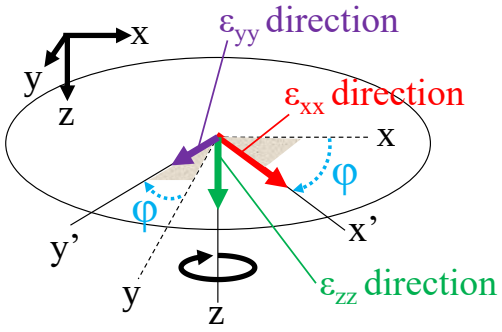

(b) θ: Rotation of y' and z axes about x' axis

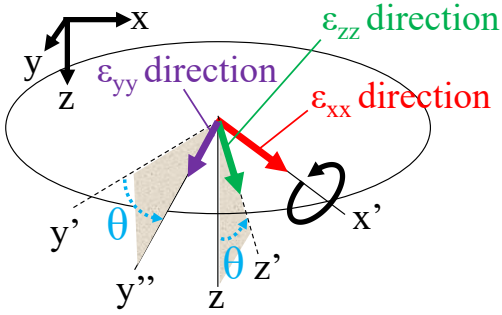

(c) ψ: Rotation of x' and y'' axes about z' axis

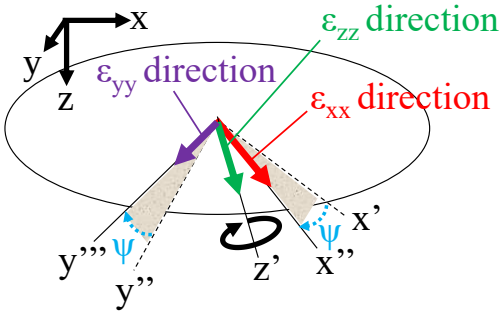

Figure 2.9: A schematic of rotation of Euler angles. (a) ϕ is to rotate x- and y-axes about z-axis. (b) θ is to rotate y'- and z-axes about x'-axis. (c) ψ is to rotate x'- and y''-axes again about z'-axis. Reproduced from Ref. [42].

2.9. Stokes Parameters

Stokes parameters (vectors) are utilized for the description of light polarization [43]. Optical elements are described by Mueller matrix in the Stokes parameters representation. The four Stokes parameters are described as

$$S_0 = I_x + I_y, \tag{2.40}$$

$$S_1 = I_x - I_y, \tag{2.41}$$

$$S_2 = I_{+45^\circ} - I_{-45^\circ}, \tag{2.42}$$

$$S_3 = I_R - I_L. \tag{2.43}$$

S_0 is the total light intensity by summation of the light intensities of linear polarization in the x-direction (I_x) and y-direction (I_y). S_1 is the light intensity where I_y is subtracted from I_x. S_2 is the light intensity where the light intensity of linear polarization at -45° ($I_{-45}{}^\circ$) is subtracted from the light intensity at +45° ($I_{+45}{}^\circ$). S_3 is the light intensity where the light intensity of left-circular polarization (I_L) is subtracted from the light intensity of right-circular polarization (I_R).

2.10. Mueller Matrix

The transformation of a Stokes vector can be described as 4×4 matrix which is called a Mueller matrix [43].

For an isotropic media, the Mueller matrix can be expressed as [41]

$$M_{Isotropic} = \begin{bmatrix} 1 & -N & 0 & 0 \\ -N & 1 & 0 & 0 \\ 0 & 0 & C & S \\ 0 & 0 & -S & C \end{bmatrix}. \tag{2.44}$$

N, C, and S are defined as [41]

$$N = \cos(2\Psi), \tag{2.45}$$

$$C = \sin(2\Psi)\cos(\Delta), \tag{2.46}$$

$$S = \sin(2\Psi)\sin(\Delta), \tag{2.47}$$

where Ψ and Δ are ellipsometry parameters which were covered in Sec. 2.8.

For an anisotropic media, the Mueller matrix is [44]

$$M_{Anisotropic} = \begin{bmatrix} 1 & -N_a - \alpha_{ps} & C_{sp} + \zeta_1 & S_{sp} + \zeta_2 \\ -N_a - \alpha_{sp} & 1 - \alpha_{sp} - \alpha_{ps} & -C_{sp} + \zeta_1 & -S_{sp} + \zeta_2 \\ C_{ps} + \xi_1 & -C_{ps} + \xi_1 & C_a + \beta_1 & S_a + \beta_2 \\ -S_{ps} + \xi_2 & S_{ps} + \xi_2 & -S_a + \beta_2 & C_a - \beta_1 \end{bmatrix}. \tag{2.48}$$

The terms in Eq. 2.48 are defined as [44]

$$N_a = (1 - \gamma^2 - \gamma_{ps}^2 - \gamma_{sp}^2)/D_a \tag{2.49}$$

$$\gamma = \tan\Psi \tag{2.50}$$

$$\gamma_{ps} = \tan\Psi_{ps} \tag{2.51}$$

$$\gamma_{sp} = \tan\Psi_{sp} \tag{2.52}$$

$$D_a = (1 + \gamma^2 + \gamma_{ps}^2 + \gamma_{sp}^2) \tag{2.53}$$

$$S_a = 2\gamma \sin(\Delta)/D_a \tag{2.54}$$

$$C_a = 2\gamma \cos(\Delta)/D_a \tag{2.55}$$

$$S_{ps} = 2\gamma_{ps} \sin(\Delta_{ps})/D_a \tag{2.56}$$

$$C_{ps} = 2\gamma_{ps} \cos(\Delta_{ps})/D_a \tag{2.57}$$

$$S_{sp} = 2\gamma_{sp}\,\sin(\Delta_{sp})/D_a \tag{2.58}$$

$$C_{sp} = 2\gamma_{sp}\,\cos(\Delta_{sp})/D_a \tag{2.59}$$

$$\alpha_{sp} = 2\gamma_{sp}/D_a \tag{2.60}$$

$$\alpha_{ps} = 2\gamma_{ps}/D_a \tag{2.61}$$

$$\beta_1 = (C_{sp}C_{ps} + S_{sp}S_{ps})D_a/2 \tag{2.62}$$

$$\beta_2 = (S_{sp}C_{ps} - C_{sp}S_{ps})D_a/2 \tag{2.63}$$

$$\zeta_1 = (CC_{ps} + SS_{ps})D_a/2 \tag{2.64}$$

$$\zeta_2 = (CS_{ps} - SC_{ps})D_a/2 \tag{2.65}$$

$$\xi_1 = (CC_{sp} + SS_{sp})D_a/2 \tag{2.66}$$

$$\xi_2 = (CS_{sp} - SC_{sp})D_a/2 \tag{2.67}$$

3. DESIGN

In contrast to conventional HMMs, biaxial HMMs (BHMMs) incorporate a birefringent element and have asymmetric hyperbolic dispersion. One of recent studies had proposed BHMMs composed of black phosphorus (BP) as an anisotropic material and gold (Au) thin films [22]. However, the study was confined to only theoretical demonstration and left real fabrication and measurements on its optical behavior.

The design goal of BHMMs was set to have quick and reliable fabrications and measurements. The materials selected for the design of BHMM were regularly accessible metal and dielectric of copper (Cu) and oblique angle deposited titanium dioxide (OAD TiO_2). The OAD technique substantially eases the achievement of biaxial components with only a 70-degree stage in physical vapor deposition (PVD) process. Variable angle spectroscopic ellipsometry (VASE) was used to extract optical constants of biaxial HMMs. On top of that, thickness of biaxial HMMs was measured physically with profilometer. Both VASE data and profilometer data would give reliability on the results.

Effective medium approximation (EMA) was utilized to analyze biaxial hyperbolic dispersion. EMA has a condition which is the period of the structure should be much smaller than the incident wavelengths [34]. VASE measures optical constants in the wavelength range of $381 \sim 894$ nm, so the structural dimension should be under 100 nm. In addition, the portion of OAD TiO_2 must be large enough within the period to obtain a considerable biaxial property of HMMs. Moreover, selection of fill factor, which is the thickness ratio between metal and dielectric, was also considered to have ENZ (epsilon-near-zero) around 632.8 nm (Helium-neon laser wavelength). Taking all the factors into consideration, the portion of OAD TiO_2 was set as 80% and the period

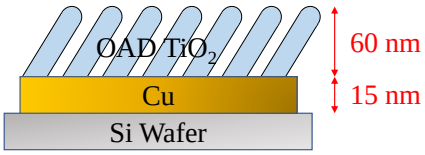

Figure 3.1: A schematic of design of biaxial hyperbolic metamaterial (BHMM). 15 nm of Cu layer would be first deposited onto the Si wafer and 60 nm of OAD TiO_2 would be deposited onto the Cu layer. The top layer should OAD TiO_2 in order to prevent Cu oxidation.

thickness was determined as 75 nm with 60 nm of OAD TiO_2 and 15 nm of Cu (20% of total thickness) (Fig. 3.1). In order to prevent oxidation of the designed BHMM, OAD TiO_2 layer would be deposited on top of Cu layer. While the normally deposited Cu layer could be modeled in the CompleteEASE program (J. A. Woollam) using default 'Cu.mat (From Palik I: pp. 284-285, 207-1823 nm)' [45] as described in Fig. 3.2, there is no model for OAD TiO_2. Optical constants of a single layer of OAD TiO_2 are required to calculate EMA for biaxial HMMs. In order to extract the optical constants, a single layer deposition of OAD TiO_2 was conducted prior to calculation. In addition, a normal TiO_2 single layer was also deposited onto sodalime glass wafer for the compari-

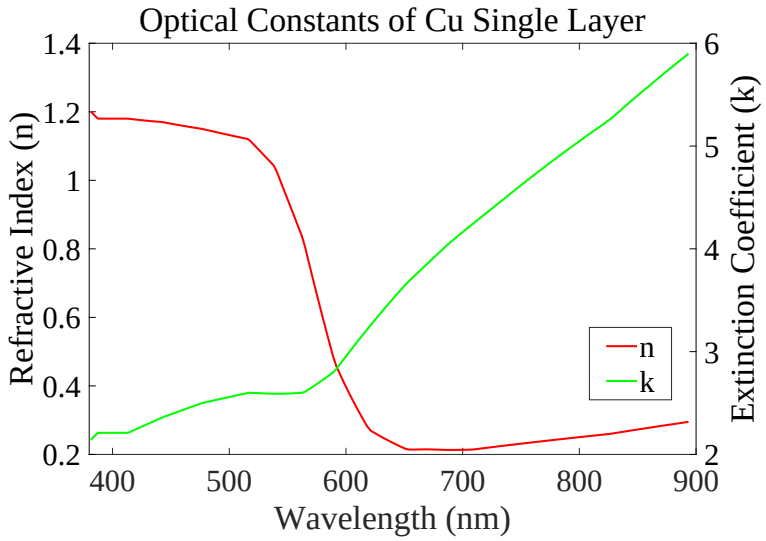

Figure 3.2: Optical constants of a Cu single layer which is default Palik's model in CompleteEASE program.

son between normal TiO_2 and OAD TiO_2. After the depositions, refractive index of a normal TiO_2 single layer was extracted via isotropic Cauchy model in the CompleteEASE program as shown in Fig. 3.3, which would be explained in more detail in Sec. 5.1.1. Using the optical constants of a Cu single layer and a normal TiO_2 single layer, permittivities and optical constants of Cu/TiO_2 uniaxial HMM were calculated through EMA using Eqs. (2.27)-(2.28) with 15 nm of Cu and 60 nm of normal TiO_2 (Fig. 3.4 and Fig. 3.5). MATLAB codes for calculation of permittivities of the uniaxial HMM are described in Appendix. A.2. Refractive index of OAD TiO_2 in x-, y-, z-directions were extracted via biaxial Cauchy model and utilized for EMA (Fig. 3.6), which would be discussed in detail at Sec. 5.1.2. Using Eqs. (2.29)-(2.31), the permittivities and optical constants of the designed Cu/OAD TiO_2 BHMM could be calculated via EMA as shown in Fig. 3.7 and Fig. 3.8 with 15 nm of Cu and 60 nm of OAD TiO_2. MATLAB codes for calculation of permittivities of the BHMM are described in Appendix. A.3. The designed BHMM has ENZ region near 625 nm with in-plane permittivity difference of 0.13 and acts as Type II hyperbolic metamaterial after 625 nm. The resulting composition provides a biaxial hyperbolic dispersion according to theoretical predictions of EMA as described.

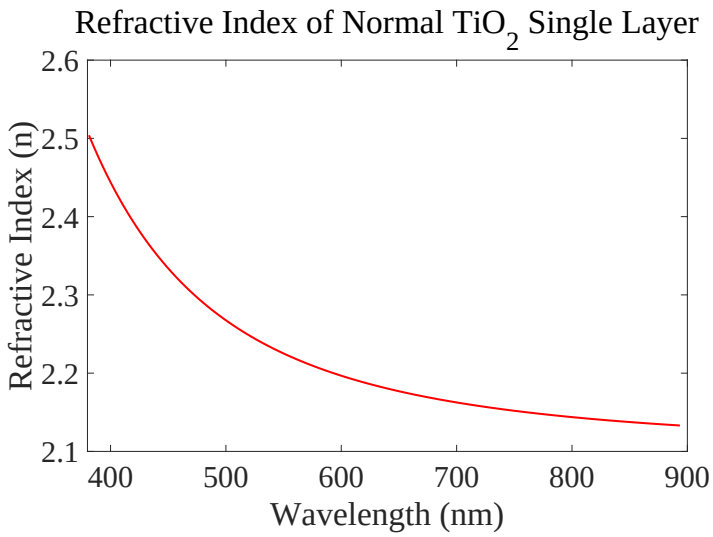

Figure 3.3: Optical constants of a normal TiO_2 single layer of 61.4 $\pm$ 0.05 nm which was measured and analyzed with Cauchy model in ellipsometry.

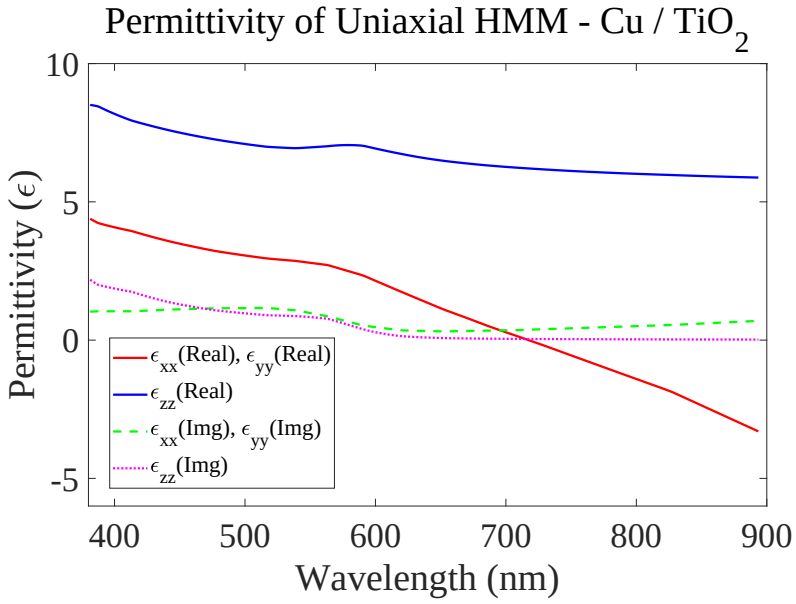

Figure 3.4: EMA calculation of permittivities of uniaxial hyperbolic metamaterial composed of 15 nm of Cu and 60 nm of normal TiO_2 using Eq. (2.27) and Eq. (2.28).

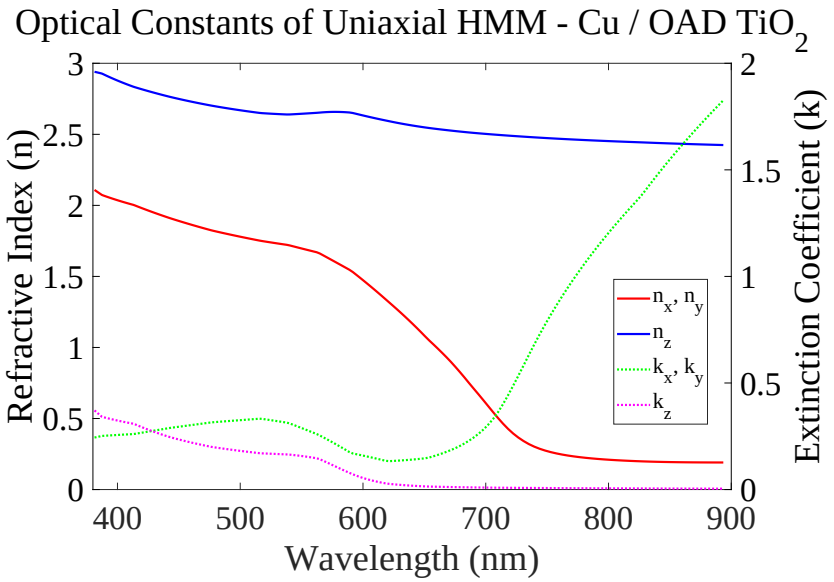

Figure 3.5: EMA calculation of optical constants of uniaxial hyperbolic metamaterial composed of 15 nm of Cu and 60 nm of OAD TiO_2.

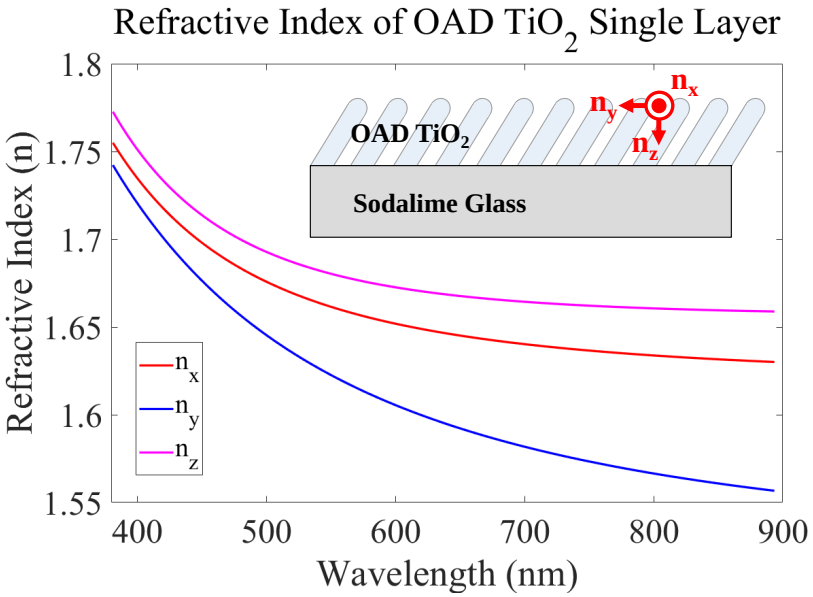

Figure 3.6: Optical constants of an OAD TiO_2 single layer of 52.5 $\pm$ 1.3 nm which was measured and analyzed with biaxial Cauchy model in ellipsometry.

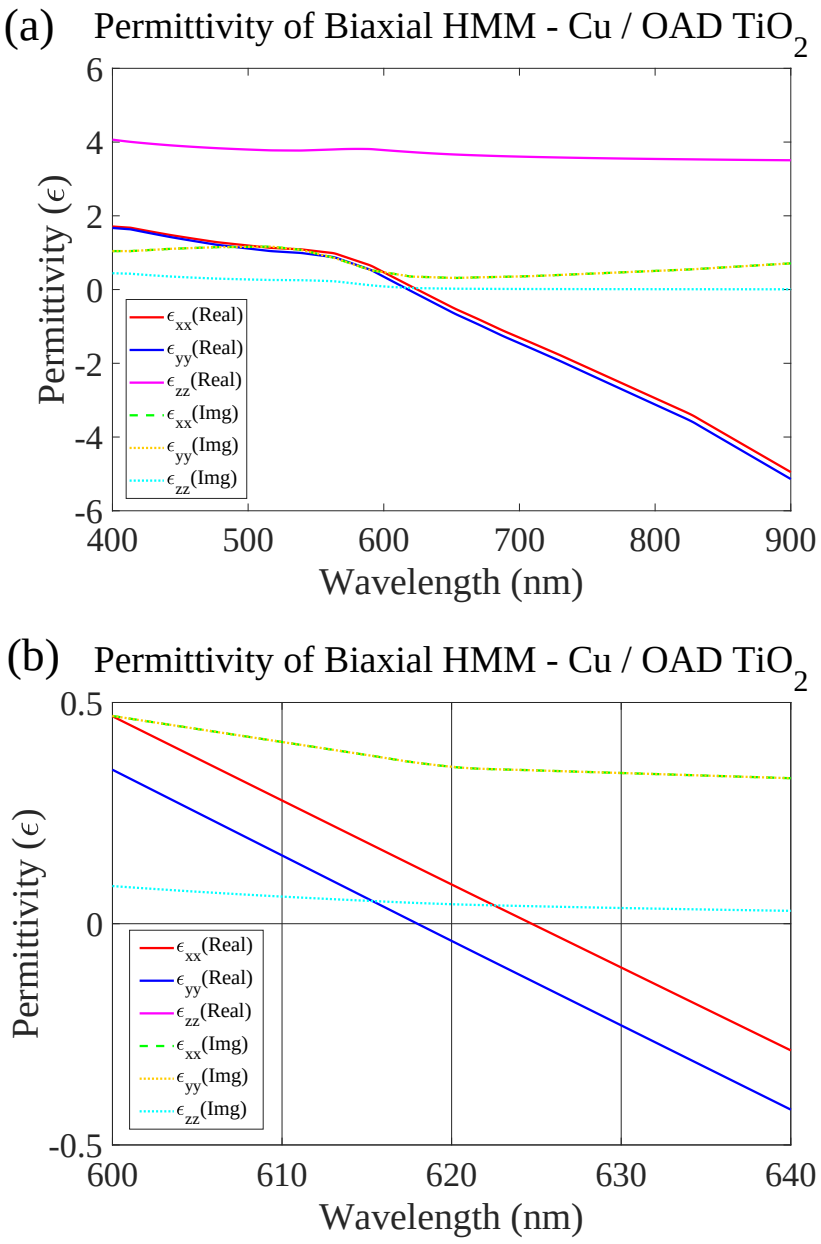

Figure 3.7: (a) EMA calculation of permittivities of biaxial hyperbolic metamaterial composed of 15 nm of Cu and 60 nm of OAD TiO_2 using Eqs. (2.29)-(2.31). (b) Zoomed graph of (a) from 600 nm to 640 nm. After 625 nm, the BHMM acts as Type II hyperbolic metamaterial. In-plane permittivity difference of 0.13 is observed.

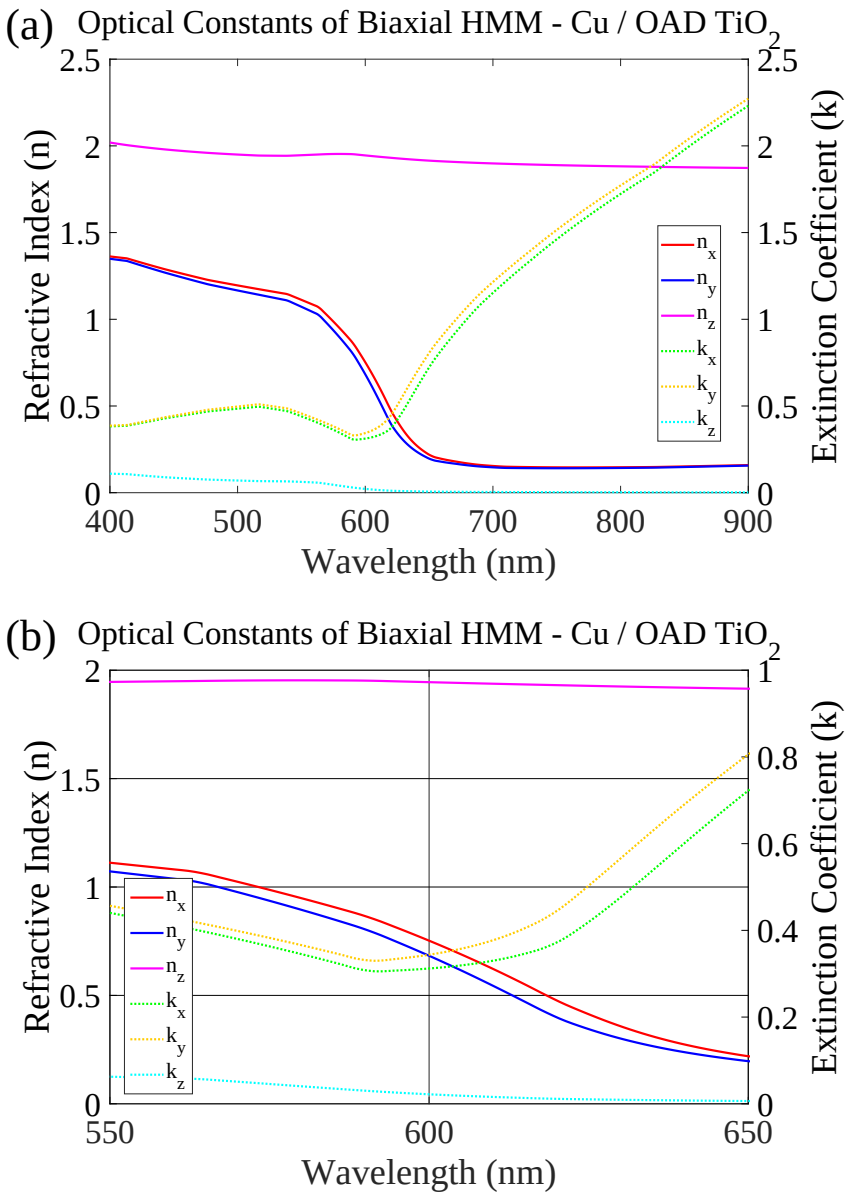

Figure 3.8: (a) EMA calculation of optical constants of biaxial hyperbolic metamaterial composed of 15 nm of Cu and 60 nm of OAD TiO_2. (b) Zoomed graph of (a) from 550 nm to 650 nm.

4. FABRICATION

Designed biaxial hyperbolic metamaterial (BHMM) was fabricated through the deposition of copper (Cu) and oblique angle deposited (OAD) titanium dioxide (TiO_2) using electron-beam physical vapor deposition (EBPVD) system (Fig. 4.1).

4.1. RCA Clean for Si Wafer

The contamination of bare silicon (Si) wafer is from certain organics, inorganics, ions, and metals. The RCA (Radio Corporation of America) clean processes are required to remove the contamination and composed of two steps: RCA 1 clean for organic dirts and RCA 2 clean for metal ions.

Figure 4.1: PVD 75 EBPVD system (Kurt J. Leskser) for the depositions of films.

4.1.1. RCA 1 Clean Process

To remove organic impurities, the RCA 1 clean process is essential. RCA 1 solution is composed of ammonium hydroxide (NH_4OH), hydrogen peroxide (H_2O_2), and deionized water (DI Water). Metal tweezers were used to handle the wafer in RCA 1 process. First, 30 ml of NH_4OH was added to 150 ml of DI Water in a Petri dish. Then, the Petri dish was heated to between 70°C and 80°C on hotplate. The next step was to add 30 ml of H_2O_2 into the Petri dish. The bare silicon wafer was then immersed into the Petri dish for ten minutes. Finally, the wafer was rinsed with DI water, and spin-dried.

4.1.2. RCA 2 Clean Process

The purpose of the RCA 2 process is to remove metal ions. RCA 2 solution is composed of hydrochloric acid (HCl), hydrogen peroxide (H_2O_2), and deionized water (DI Water). Plastic tweezers were used to handle the wafer in RCA 2 process. First, 30 ml of HCl was added to 180 ml of DI Water. Then, the Petri dish was heated to between 70°C and 80°C on hotplate. The next step was to add 30 ml of H_2O_2 into the Petri dish. The Si wafer processed in RCA 1 clean process was then immersed into the Petri dish for ten minutes. Finally, the wafer was rinsed with DI water, and spin-dried.

4.2. Quick Clean for Sodalime Glass Wafer

Sodalime glass wafers were used to deposit a single layer of TiO_2, OAD TiO_2, and Cu to extract their optical constants. Before the deposition, acetone was firstly used to remove organics and greases. However, the acetone leaves some contaminants on the wafer because of its high evaporation rate. The next step was to use methanol since it is efficient to take away residues and

Figure 4.2: Acetone, methanol, isopropanol and DI water for quick clean of sodalime glass.

contaminants of acetone. Then, isopropanol was utilized to rinse remained methanol and acetone. Finally, the wafer was further cleaned with DI water, and spin-dried (Fig. 4.2).

4.3. EBPVD Process

EBPVD is essential process to deposit Cu layer and OAD TiO_2 layer. A schematic of overall process is described in Fig. 4.3. An electron gun is placed outside of deposition region to prevent contamination from evaporant.

4.3.1. Preparations

The deposition process was conducted via Kurt J. Lesker PVD 75 system. The graphite crucible (Kurt J. Lesker) was used to contain the evaporation materials. Two types of wafer were used: Silicon wafer and sodalime glass wafer. Sodalime glass wafer (University Wafer, Thickness: 500 μm, Diameter: 100 mm) was used to examine a normal TiO_2 single layer, an OAD TiO_2 single layer and a Cu single layer. Silicon wafer (University Wafer, p-type, 0-100 ohm-cm, <100>, 1-side polished, Diameter: 100 mm, Thickness: 525 +/- 25 μm, Grade: Test Wafer) was to fabricate biaxial HMMs. Two materials were prepared: Copper (Cu) pellets (Kurt J. Lesker, 99.99% Pure,

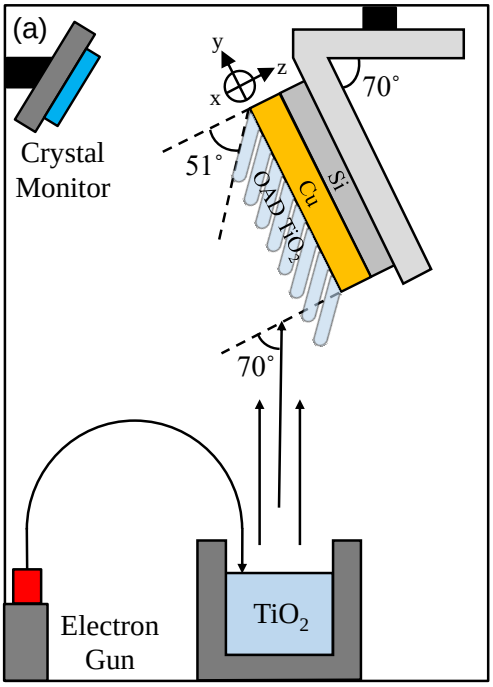

Figure 4.3: A schematic of fabrication of BHMMs using EBPVD system. Oblique angle deposition of TiO_2 was conducted with substrate placed at an angle of 70° resulting in nanocolumnar structures at 51° with respect to the substrate's normal based on Eq. (2.17). Electron beam from the electron gun is bent by magnetic field in order to avoid contamination of electron gun from evaporant.

1/8" diameter $\times$ 1/8" long) and titanium dioxide (TiO_2) pieces (Kurt J. Lesker, 99.9% Pure, 1-4 mm pieces). Finally, a 70-degree stage was utilized to deposit OAD TiO_2 layer.

4.3.2. Deposition of a Single Layer of Normal TiO_2

Although the normal deposition of TiO_2 was actually not necessary for BHMMs, the process was conducted in order to compare normally deposited TiO_2 and OAD TiO_2. First, the graphite crucible was filled three-fourths with TiO_2 pieces. In case the material is not filled enough, a hole would be formed at the center of the materials in the crucible (Fig. 4.4). Then, the sodalime glass wafer was mounted onto the EBPVD stage (Fig. 4.5). Next, the EBPVD chamber was vacuumed down to 5.00×10^{-5} Torr with cooling system on. The target thickness was set to 60 nm in the

Figure 4.4: The hole at the center of TiO_2 crucible materials because of lack of filled materials.

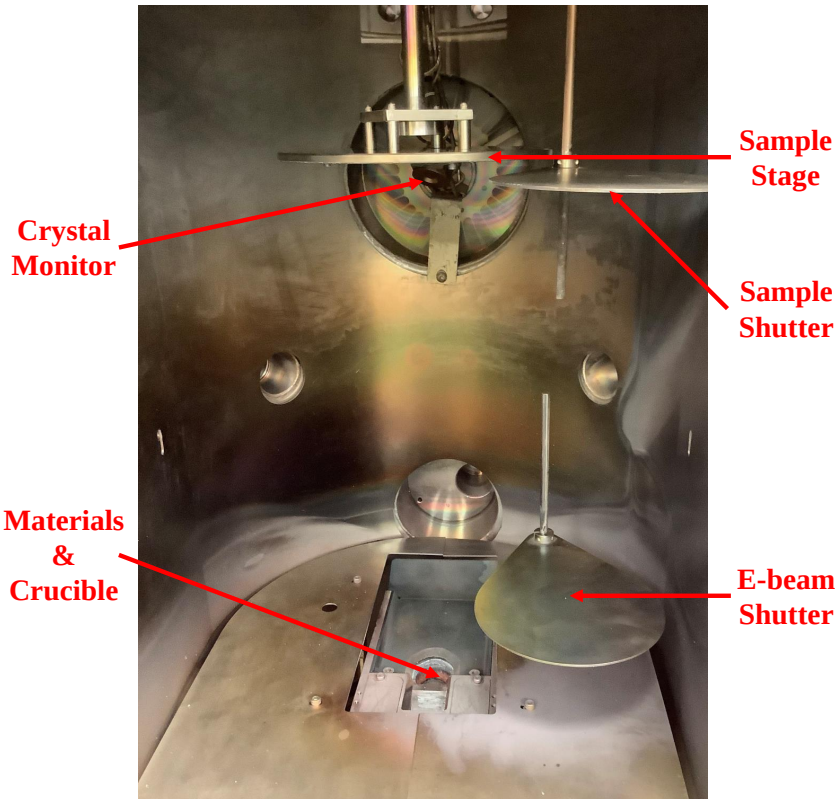

Figure 4.5: Configuration of TiO_2 normal deposition in EBPVD system.

control panel, and the starting deposition rate was set to 0.1 Å/s which is the smallest deposition rate in the EBPVD system. The settings for both of normal TiO_2 and OAD TiO_2 depositions are described in Table 4.1. The starting deposition rates of 0.5 Å/s and 1 Å/s were also conducted, but the EBPVD system shut off during the deposition process with a spike in the crucible. This is because TiO_2 adsorbs water well due to bridging oxygen vacancies (BOV) [46], N_{BOV} (concentration of bridging oxygen vacancies) of 5% which is exposed to 0.1 L could be fully hydroxylated within a few minutes even at relatively low vacuum conditions of 2.25×10^{-10} Torr [46, 47]. Typical base operating pressure in the EBPVD system is 5×10^{-5} Torr, so the surface of TiO_2 materials is likely to be fully coated with water which is remained in the chamber under the pressure. Heating the

Table 4.1: EBPVD settings for normal TiO_2 and OAD TiO_2 deposition.

Tab	Setting
Layer Tab	SetPt = 0.10 Å/s
	Final Thick. = 0.600 kÅ
Deposit Tab	P term = 2
	I term = 1.3 sec
	D term = 0.06 sec
Pre Condition Tab	Ramp 1 Power = 0.75%
	Ramp 1 Time = 15.00 Sec
	Soak 1 Time = 30.00 Sec
	Ramp 2 Power = 1.50%
	Ramp 2 Time = 15.00 Sec
	Soak 2 Time = 30.00 Sec
Post Condition Tab	Ramp Time = 60.00 Sec
Source/Sensor Tab	Sensor Tooling (%) = 100.0
	Max. Power = 10.00%
Error Tab	Crystal Fail = Enabled (3 Counts)

TiO_2 materials via EBPVD system causes the water boil off at the surface of TiO_2 materials, and this would make a spike due to the boiling water. Thus, it is required to set the starting deposition rate of TiO_2 as the lowest and increase the rate gradually until 0.3 Å/s in order to give enough time to evaporate the water. To start the deposition, E-beam was turned on with 1% setpoint. The deposition rate was stabilized at 0.1 Å/s at the running time of 25 minutes, then the rate was changed to 0.2 Å/s. At the running time of 45 minutes, the rate was increased to 0.3 Å/s. Finally, the deposition of a single layer of TiO_2 was completed at the running time of 93 minutes. The time required for the deposition of TiO_2 was quite fluctuating which might be caused by water adsorbing characteristics of TiO_2 material. Total two samples were fabricated. The thickness and optical constants of the samples were characterized via VASE in Sec. 5.1.1.

4.3.3. Deposition of a Single Layer of OAD TiO_2

Before the fabrication of BHMM, a single layer of OAD TiO_2 was deposited to extract its optical constants for EMA calculations. The thickness of OAD TiO_2 would not be uniform because the slanted 70-degree stage causes different path length from the crucible to the substrate, so it is required to verify the thickness of the fabricated single layer of OAD TiO_2 with input thickness (Fig. 4.6). All the process was same with the process of normally deposited TiO_2 except requirement of the 70-degree stage. The 70-degree stage was custom-made in house which can hold the wafer properly at a 70-degree to the normal direction. A sodalime glass wafer was mounted on the stage, and the system was vacuumed down to 5.00×10^{-5} Torr with cooling system on. The initial setting for OAD TiO_2 deposition is described in Table 4.1. The target thickness was 60 nm, and the starting deposition rate was set to 0.1 Å/s because of the same reason with the process of normally deposited TiO_2 single layer (Sec. 4.3.2). The deposition rate was gradually increased until 0.3 Å/s.

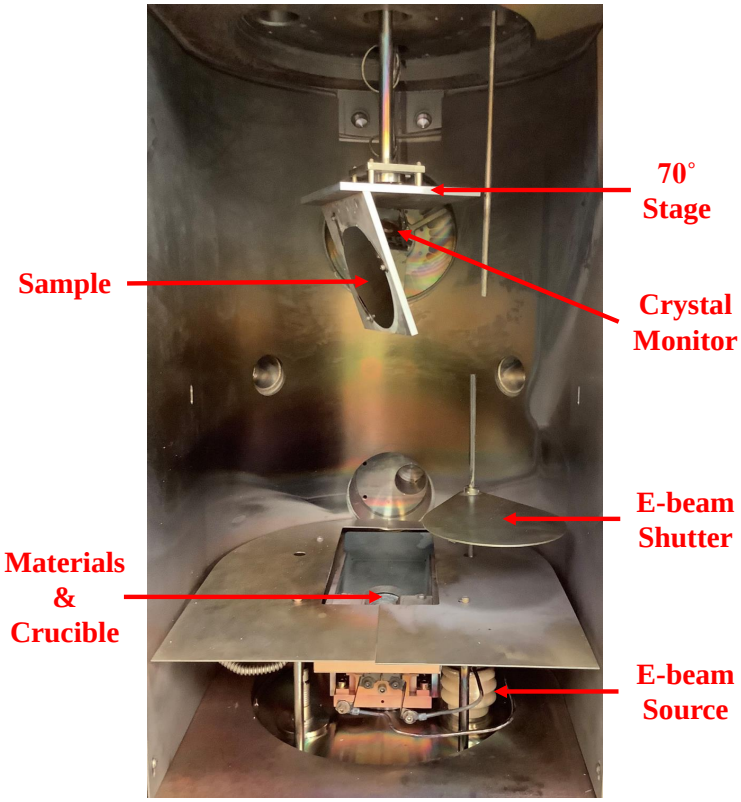

Figure 4.6: Configuration of OAD TiO_2 deposition in EBPVD system. Slanted shape of 70-degree stage causes different path length from the crucible to the slanted substrate, so the OAD film thickness is not uniform.

To start the deposition, E-beam was turned on with 1% setpoint. After stabilization of the deposition rate of 0.1 Å/s at the running time of 25 minutes, the rate was changed to 0.2 Å/s. Then, the rate was increased to 0.3 Å/s at the running time of 45 minutes. Finally, the deposition of a single layer of OAD TiO_2 was completed at the running time of 87 minutes. The time required for the deposition of OAD TiO_2 was fluctuating which might be caused by water adsorbing characteristics of TiO_2 materials (Sec. 4.3.2). The fabrication result is shown in Fig. 4.7. Total two samples were fabricated. The thickness and optical constants of the samples would be characterized via VASE in Sec. 5.1.2.

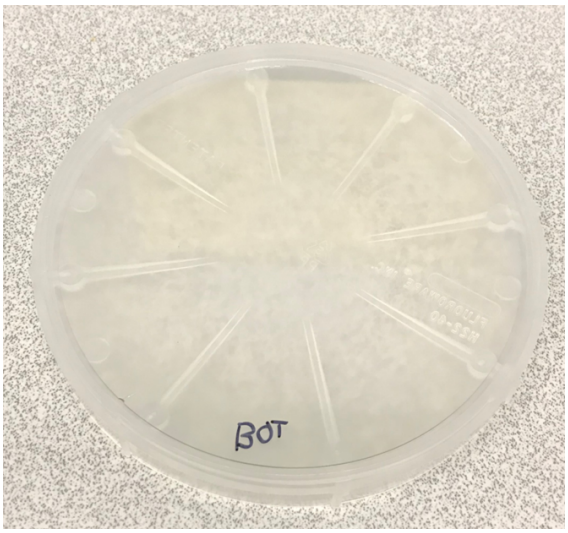

Figure 4.7: The fabricated OAD TiO_2 60 nm single layer on sodalime glass.

4.3.4. Deposition of a Single Layer of Cu

The deposition of a single layer of Cu is required to verify if optical constants of the thin Cu layer are well matched with optical constants of bulk Cu. First, the graphite crucible was filled three-fourths with Cu pellets. Next, the sodalime glass wafer was mounted onto the EBPVD stage and the EBPVD chamber was vacuumed down to 5.00×10^{-5} Torr with cooling system on. The initial setting for Cu deposition is described in Table 4.2. The target thickness was set to 15 nm in the control panel, and the starting deposition rate was set to 0.5 Å/s. To start the deposition, E-beam was turned on with 2% setpoint. The deposition process was completed at the running time of 6 minutes. The fabrication result is shown in Fig. 4.8. Total two samples were fabricated. The thickness and optical constants of the samples would be characterized via VASE using default Cu model in the CompleteEASE program in Sec. 5.1.3.

Table 4.2: EBPVD settings for Cu deposition.

Tab	Setting
Layer Tab	SetPt = 0.50 Å/s
	Final Thick. = 0.150 kÅ
Deposit Tab	P term = 25
	I term = 1.0 sec
	D term = 0.01 sec
Pre Condition Tab	Ramp 1 Power = 2.00 %
	Ramp 1 Time = 30.00 Sec
	Soak 1 Time = 60.00 Sec
	Ramp 2 Power = 4.00 %
	Ramp 2 Time = 30.00 Sec
	Soak 2 Time = 90.00 Sec
Post Condition Tab	Ramp Time = 0.00 Sec
Source/Sensor Tab	Sensor Tooling (%) = 100.0
	Max. Power = 30.00 %
Error Tab	Crystal Fail = Enabled (3 Counts)

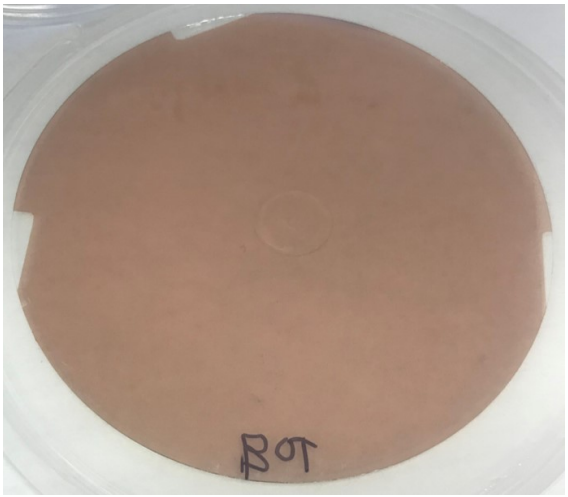

Figure 4.8: The fabricated single Cu layer of 15 nm on sodalime glass.

4.3.5. Fabrication of Biaxial HMMs using Cu and OAD TiO_2

The designed biaxial HMM consists of Cu and OAD TiO_2 on top of a Si wafer. In contrast with previous used sodalime glass wafer, Si wafer was used as substrate in order to get a cleaner surface of the substrate with RCA clean. To prevent oxidation of Cu layer, Cu was firstly deposited onto the Si wafer and then OAD TiO_2 layer was covered the Cu layer. First, RCA cleaned Si wafer was mounted on the EBPVD stage for the deposition of 15 nm Cu layer. With the same condition covered in Sec. 4.3.4, the 15 nm Cu layer was deposited onto the Si wafer. The next step was to replace the EBPVD stage for the normal deposition with 70-degree stage. Then, the OAD TiO_2 layer was deposited with the same process which was covered in Sec. 4.3.3. The fabrication result is shown in Fig. 4.9. Graded color was observed since OAD TiO_2 layer is not uniform over the wafer because of the tilted 70-degree stage in the deposition process. The fabricated BHMM is composed of 15 nm of Cu and 60 nm of OAD TiO_2. Total two samples were fabricated. The thickness and optical constants of the samples would be characterized via VASE using biaxial EMA models in x-, y-, z-directions in CompleteEASE program in Sec. 5.1.4.

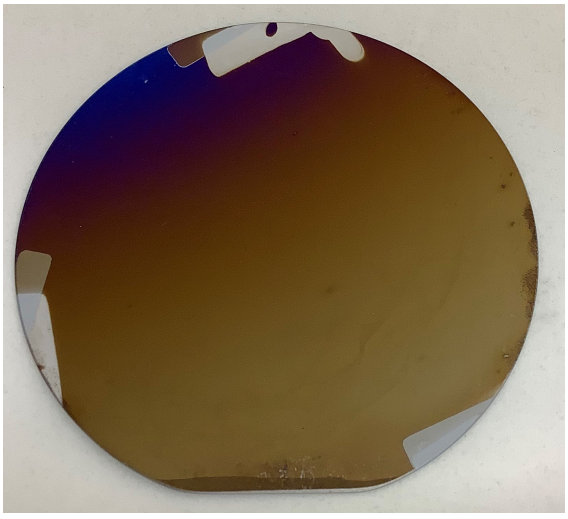

Figure 4.9: The fabricated BHMM composed of OAD TiO_2/Cu/Si. Graded color was observed because of the tilted 70-degree stage in the OAD deposition process.

5. CHARACTERIZATION

5.1. Variable Angle Spectroscopic Ellipsometry (VASE)

A variable angle spectroscopic ellipsometry (VASE) was utilized to measure optical constants and thickness. The α-SE J. A. Woollam variable angle spectroscopic ellipsometry system with CompleteEASE ellipsometry program version 4.72 was utilized for the sample characterization (Fig. 5.1). The first step was to measure single layers of TiO_2, OAD TiO_2 and Cu with VASE, and then optical constants of the three single layers were extracted to apply them to EMA model of the biaxial HMM. Afterwards, the fabricated biaxial HMM was measured.

Figure 5.1: α-SE J. A. Woollam variable angle spectroscopic ellipsometry system [48]

5.1.1. Measurements of single normal TiO_2 layer

The single layer of normal TiO_2 on top of a sodalime glass wafer was measured via VASE. The three angle measurement with 65-, 70-, and 75-degree was conducted since it helps to use entire delta (Δ) domain and to average the data. After the measurement, the model for single normal TiO_2 sample was created. Details of the model parameters are provided in Fig. 5.2 and

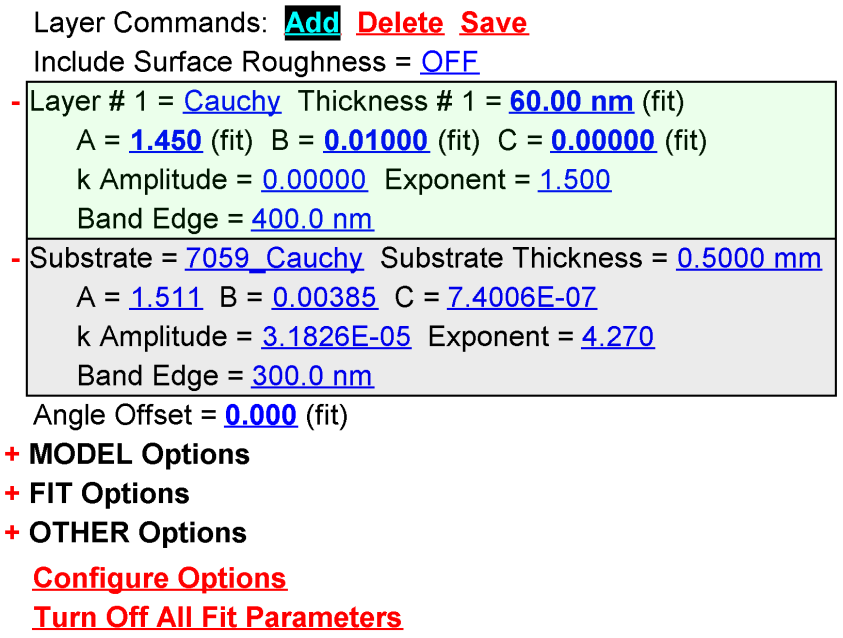

Figure 5.2: VASE Model for normal TiO_2 single layer with fit on thickness, angle offset and Cauchy parameters of A, B, C.

Table 5.1: VASE Model for normal TiO_2 single layer.

Basic Model	Glass with Transparent Film (with Backside reflection).mod
Layer 1	Cauchy Film (Fit on A, B, C)
Substrate	7059_Cauchy substrate, thickness : 0.5 mm
Angle Offset	Fit on

Table 5.1.

The 'Glass with Transparent Film (with Backside reflection)' model was used in CompleteEASE program (J. A. Woollam). The model had the substrate as '7059_Cauchy' whose optical constants are representative of many glass substrates [41]. For the transparent substrate, it is likely to have the light reflected from the back surface of the substrate. This backside reflection was corrected by the CompleteEASE based on collected depolarization data [41]. Since the thickness of

the sodalime glass wafer is 0.5 mm, put this value into 'Substrate Thickness' in the model. Then, 'Cauchy Film' was set to the layer on top of the substrate since the TiO_2 single layer is dielectric material. Cauchy coefficients *A*, *B*, *C*, thickness of the 'Cauchy Film' was being fitted. 'Angle Offset' specifies an offset to the nominal angle of incidence specified in the experimental data [41] and was being fitted as well. Extinction coefficient *k* was assumed as zero and was not fitted in this process since dielectrics are non-conductors, so their extinction coefficient in the VASE model was zero. A total of three measurements were conducted on three different spots of the sample for comparison and credibility. The fit results are described in Table 5.2. For the measurements on three different spots, thickness was fitted as 61.4 $\pm$ 0.05 nm with MSE of 3.88, 61.2 $\pm$ 0.04 nm with MSE of 3.76, and 61.3 $\pm$ 0.05 nm with MSE of 4.24 respectively. The three results were similar one another with low MSE, and the target thickness of 60 nm is well matched with the ellipsometric results, so the results are reliable. Δ and Ψ values of the three measurement spots are described in Figures 5.3-5.5. *N*, *C*, and *S* data of the three measurement spots are shown in Figures 5.6-5.8. Optical constants of normal TiO_2 single layer were extracted as shown in Figures 5.9-5.11. Uniqueness fit on thickness was conducted as shown in Figures 5.12-5.14.

Table 5.2: Fit results of normal TiO_2 single layer.

	Measurement Spot 1	**Measurement Spot 2**	**Measurement Spot 3**
MSE	3.88	3.76	4.24
Thickness	61.4 $\pm$ 0.05 nm	61.2 $\pm$ 0.04 nm	61.3 $\pm$ 0.05 nm
A	2.103 $\pm$ 0.002	2.106 $\pm$ 0.002	2.114 $\pm$ 0.002
B	0.0139 $\pm$ 0.001	0.0133 $\pm$ 0.001	0.0135 $\pm$ 0.001
C	0.0053 $\pm$ 0.0001	0.0055 $\pm$ 0.0001	0.0056 $\pm$ 0.0002
Angle Offset	-0.3° $\pm$ 0.02°	-0.3° $\pm$ 0.02°	-0.3° $\pm$ 0.02°

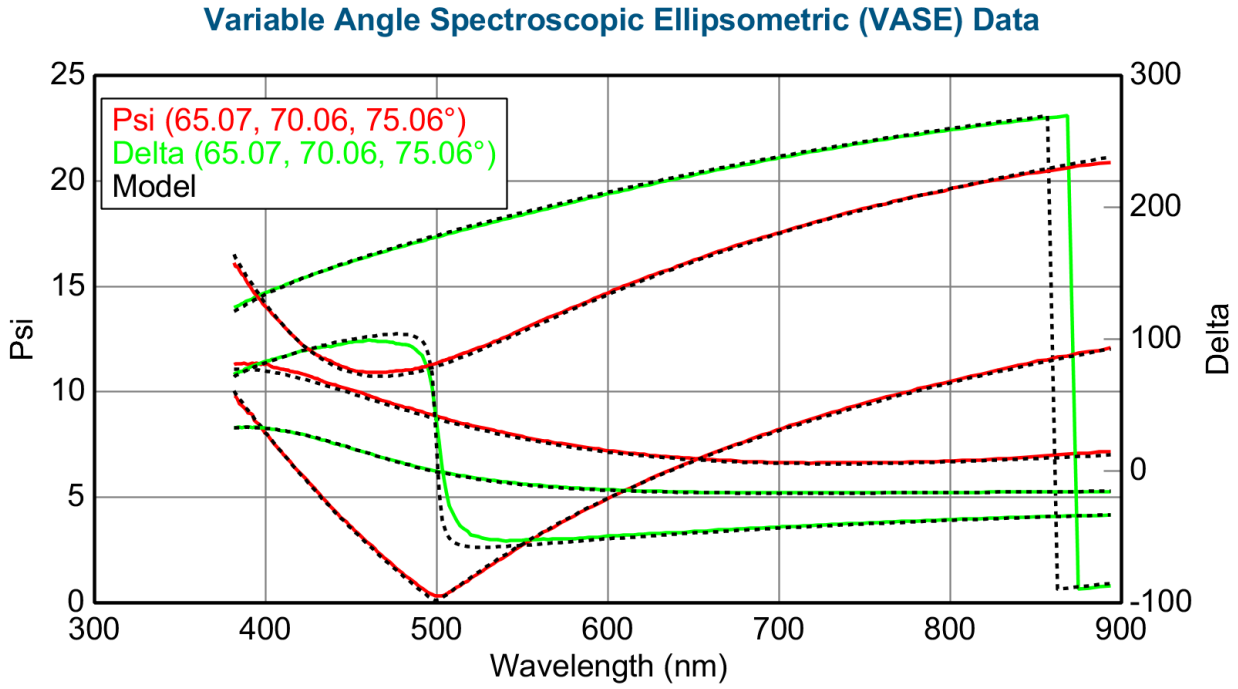

Figure 5.3: Δ and Ψ of normal TiO_2 single layer at measurement spot 1.

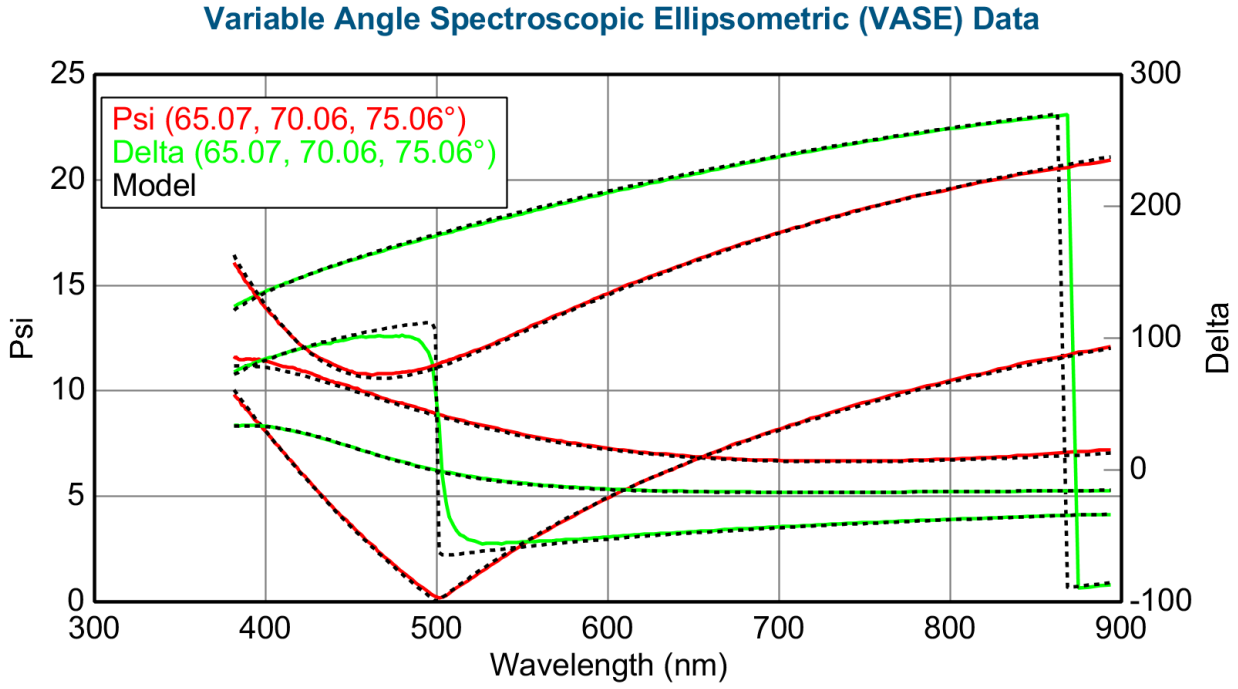

Figure 5.4: Δ and Ψ of normal TiO_2 single layer at measurement spot 2.

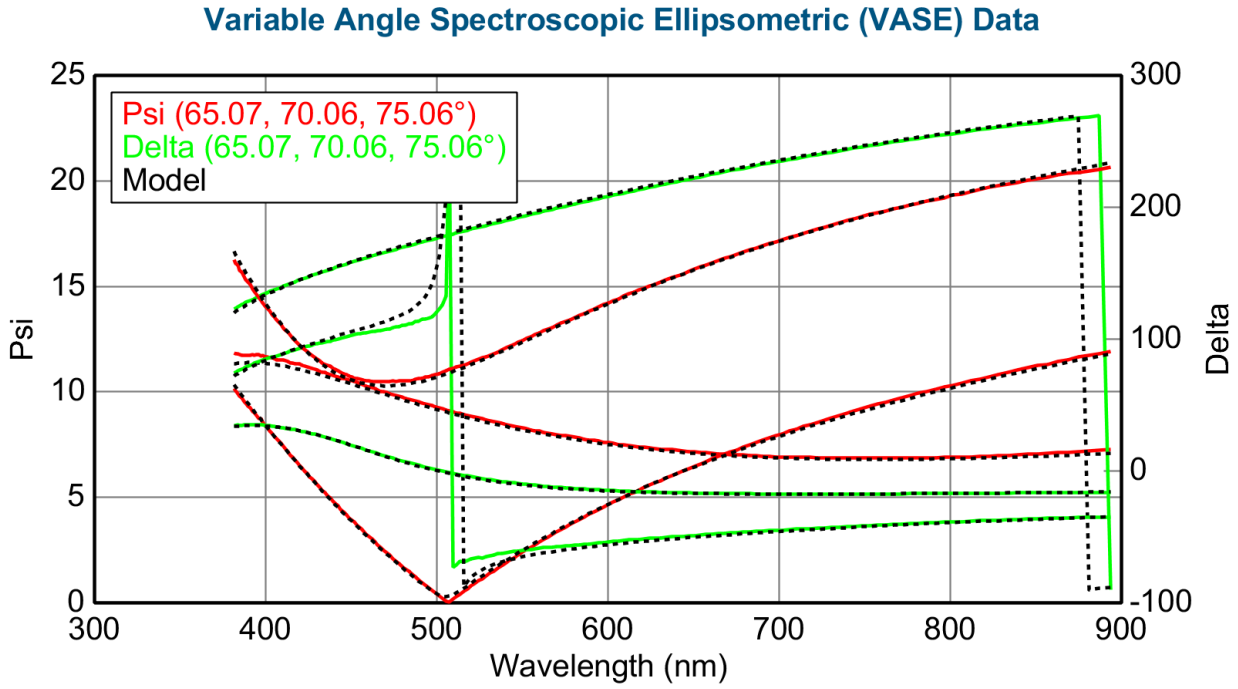

Figure 5.5: Δ and Ψ of normal TiO_2 single layer at measurement spot 3.

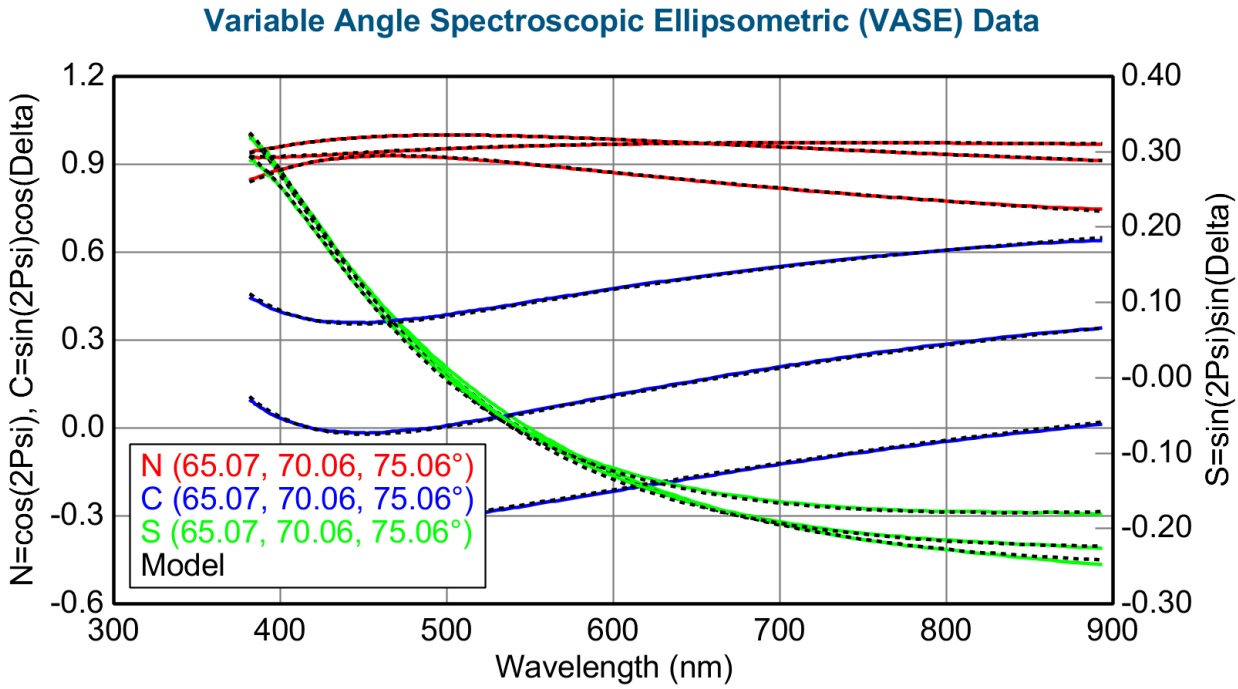

Figure 5.6: *N*, *C*, *S* data of normal TiO_2 single layer at measurement spot 1.

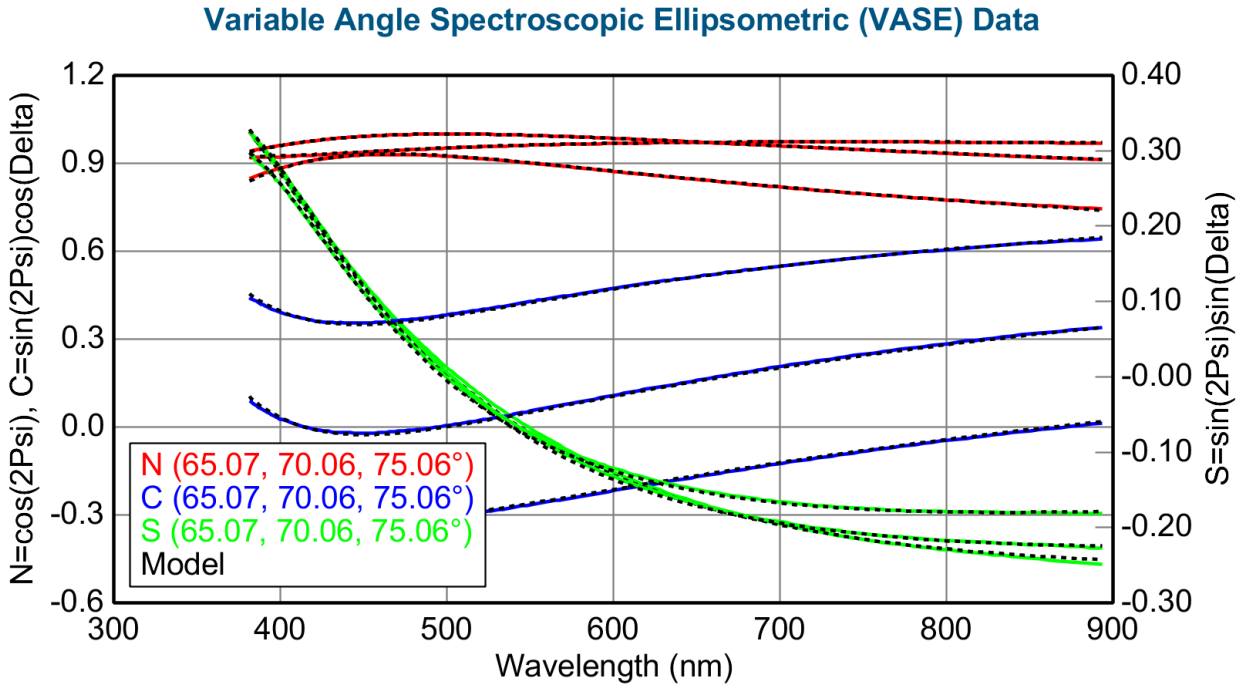

Figure 5.7: *N*, *C*, *S* **data of normal TiO_2 single layer at measurement spot 2.**

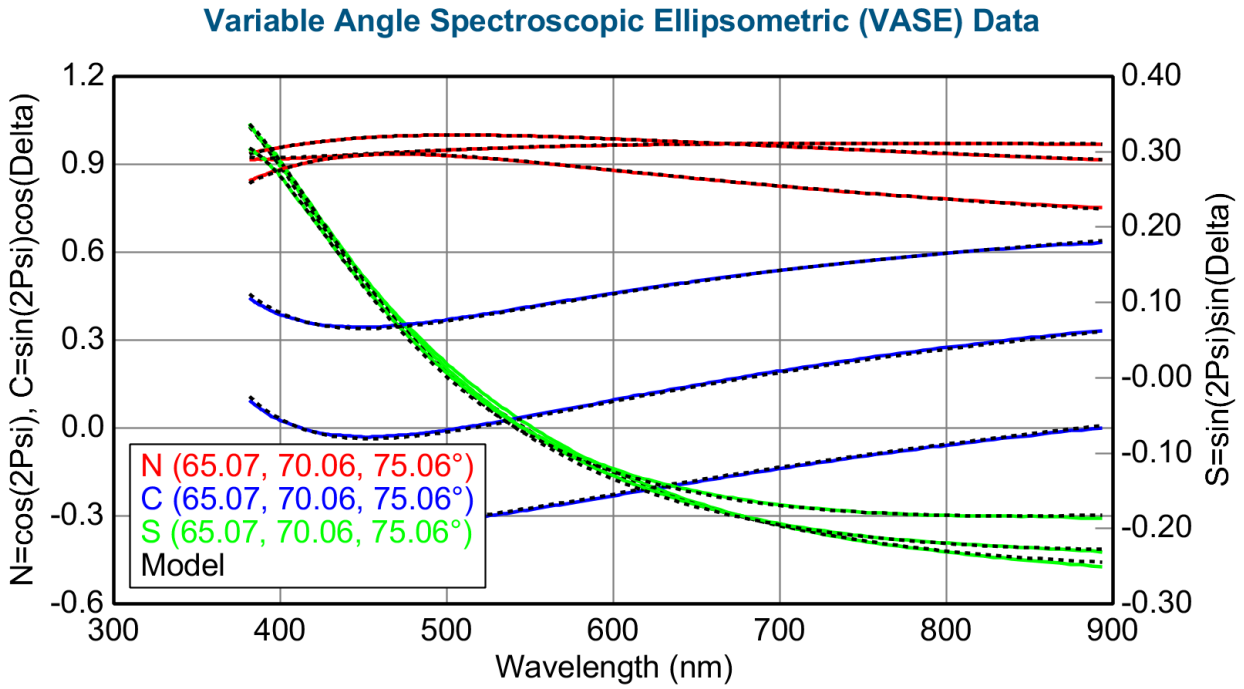

Figure 5.8: *N*, *C*, *S* **data of normal TiO_2 single layer at measurement spot 3.**

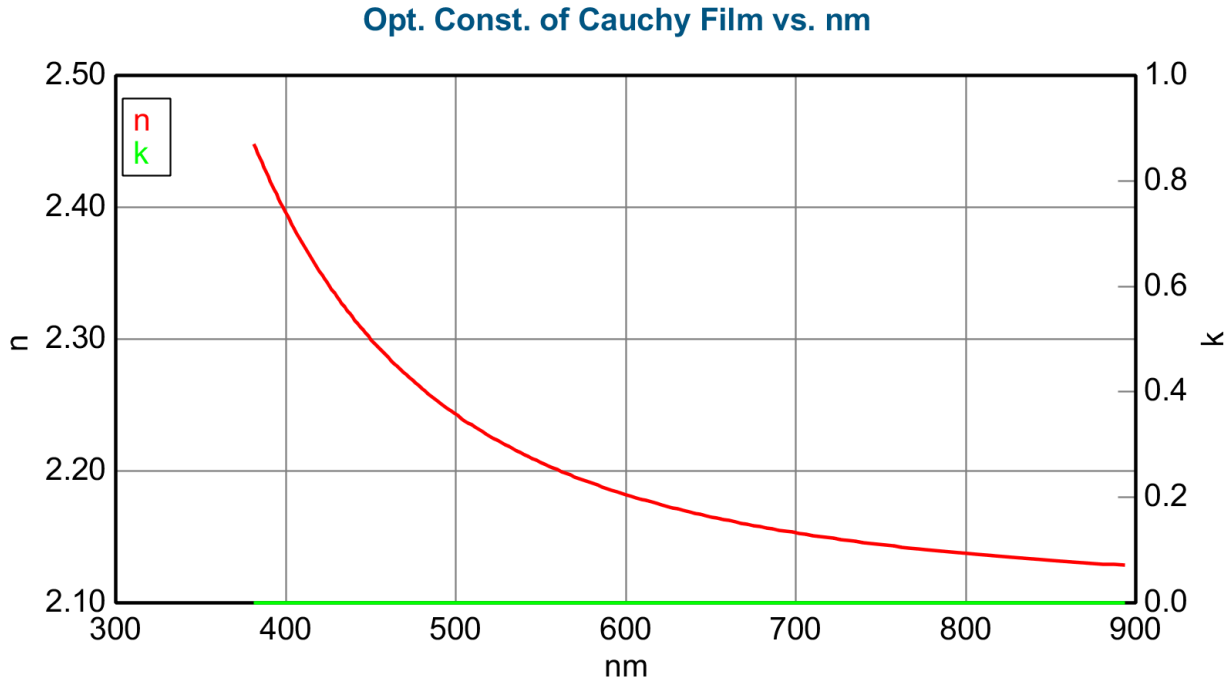

Figure 5.9: Optical constants of normal TiO_2 single layer at measurement spot 1.

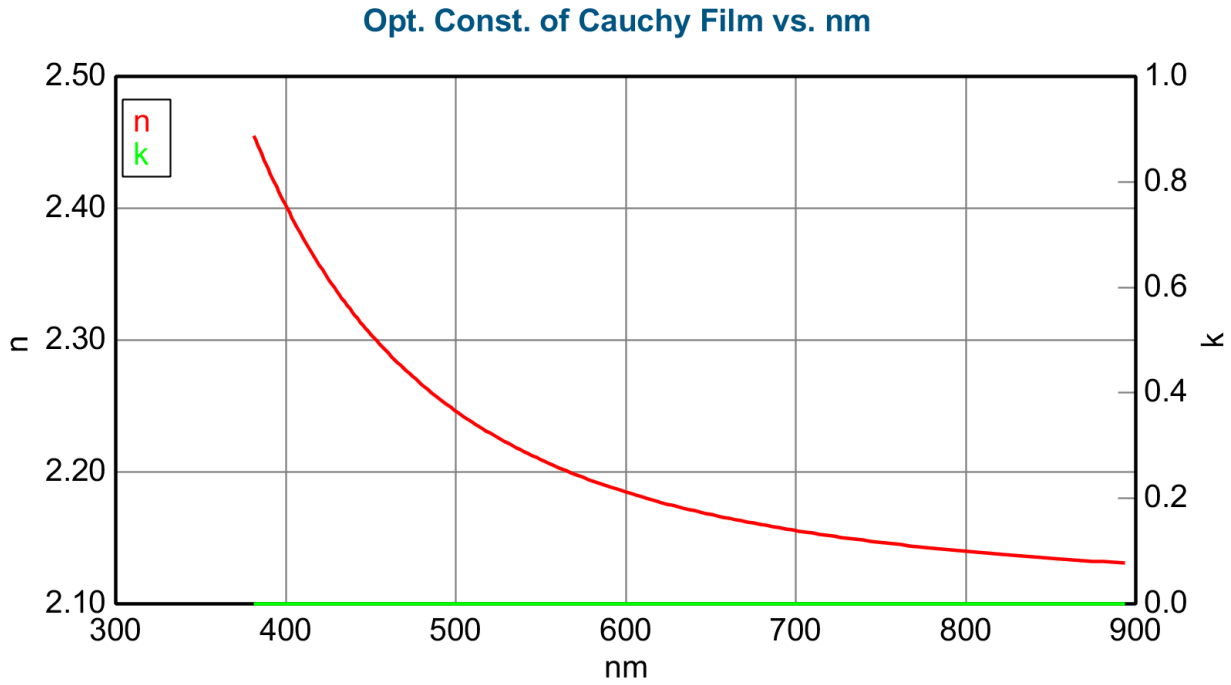

Figure 5.10: Optical constants of normal TiO_2 single layer at measurement spot 2.

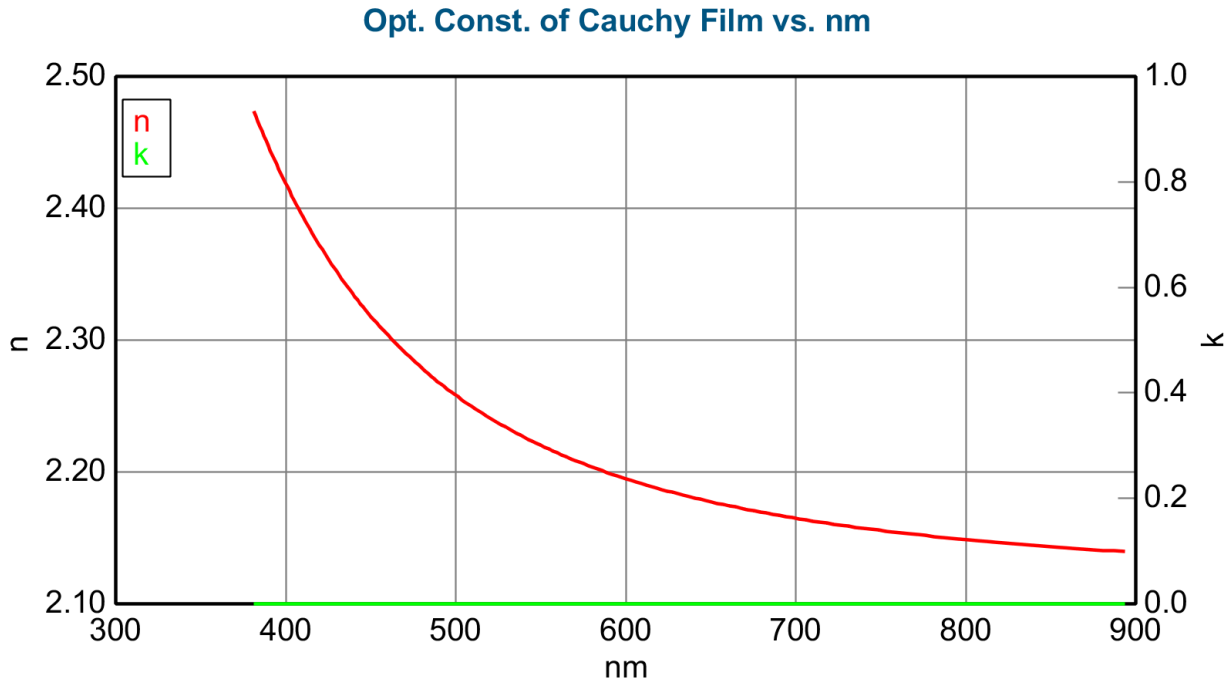

Figure 5.11: Optical constants of normal TiO_2 single layer at measurement spot 3.

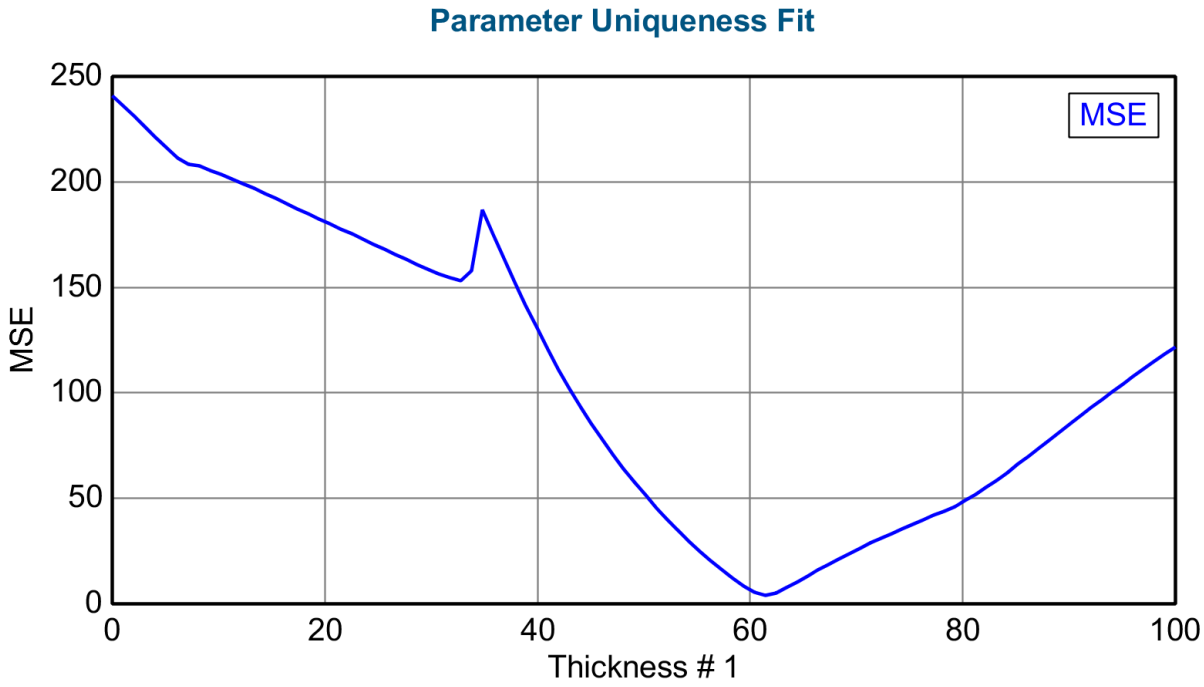

Figure 5.12: Uniqueness fit of normal TiO_2 single layer from 0 to 100 nm at measurement spot 1.

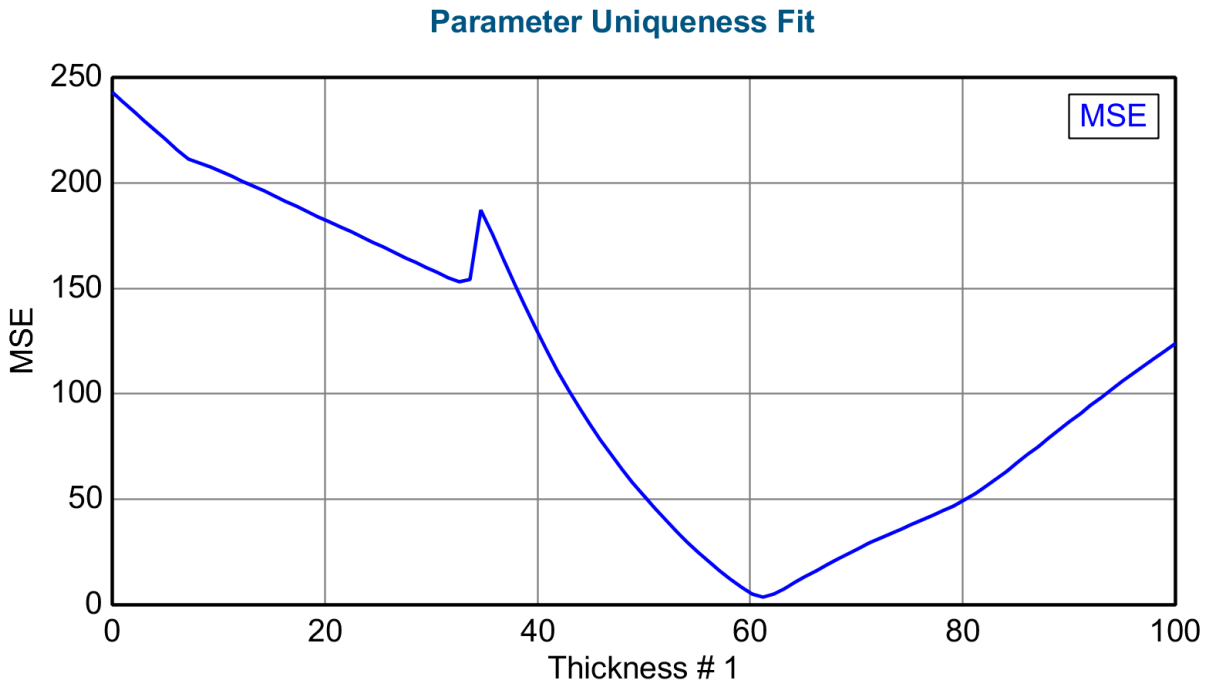

Figure 5.13: Uniqueness fit of normal TiO_2 single layer from 0 to 100 nm at measurement spot 2.

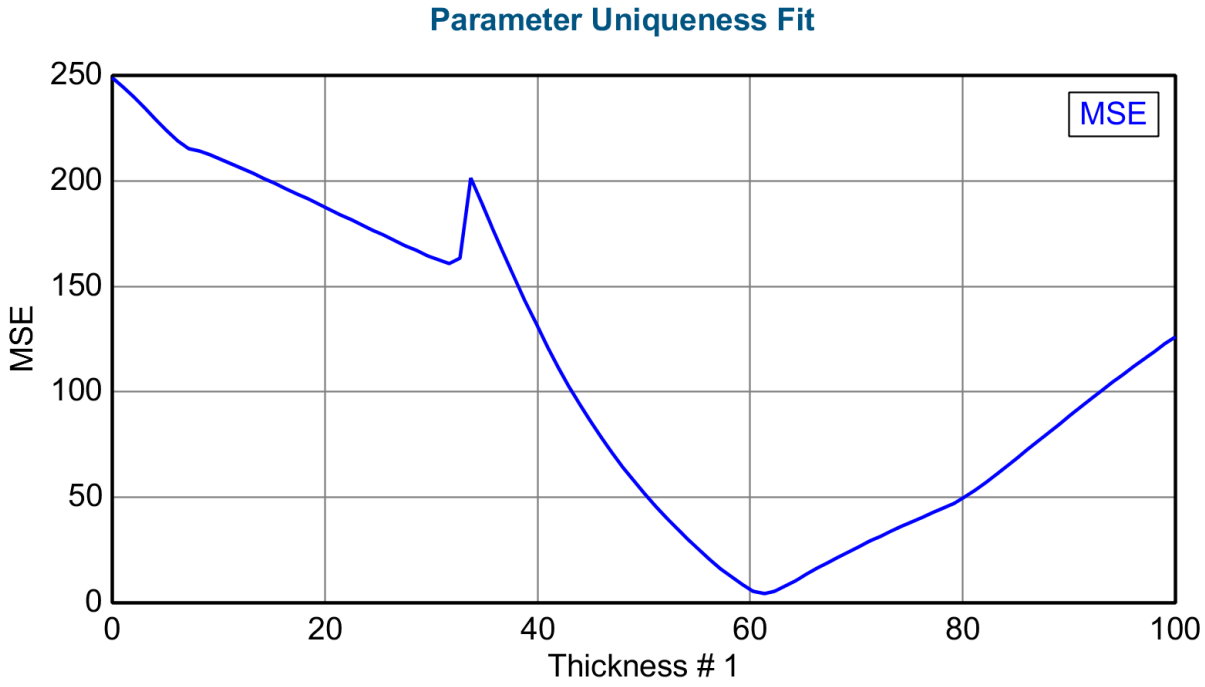

Figure 5.14: Uniqueness fit of normal TiO_2 single layer from 0 to 100 nm at measurement spot 3.

5.1.2. Measurements of single OAD TiO_2 layer

Column axis angle β of OAD TiO_2 nanocolumnar structures at deposition angle α of 70° was calculated as 51° in Chap. 2.4. Our research group had previously taken SEM (Scanning Electron Microscopy) image of polarizing beam splitter composed of normal TiO_2 and OAD TiO_2 with deposition angle α of 70°, and the calculation of 51° is in a good agreement with the SEM image [24]. The single OAD TiO_2 layer on top of a sodalime glass wafer was measured via VASE with three angle measurement (65-, 70-, 75-degree). Details of the model parameters are provided in Table 5.3 and Fig. 5.15. Next, the 'Glass with Transparent Film (with Backside reflection)' model was chosen in the CompleteEASE program. The substrate was chosen as '7059_Cauchy' with inclusion of 0.5 mm thickness for correcting backside reflection in the program. Then, 'Cauchy Film' was changed to 'Biaxial' layer to extract n_x, n_y, and n_z. Under the 'Biaxial' layer in the model, 'Cauchy Film' was applied to 'E_x', 'E_y', 'E_z' components with all the A, B, C parameters fit on. 'Angle Offset' was being fitted as well. 'Euler Angles' are composed of ϕ, θ, ψ which are terms to rotate the orientation of optical axes relative to the ellipsometer measurement orientation (Fig. 2.9). All

Table 5.3: VASE Model for OAD TiO_2 single layer.

Basic Model	Glass with Transparent Film (with Backside reflection).mod
Layer 1	Biaxial E_x = Cauchy Film (Fit on A, B, C) E_y = Cauchy Film (Fit on A, B, C) E_z = Cauchy Film (Fit on A, B, C)
Substrate	7059_Cauchy substrate, thickness : 0.5 mm
Angle Offset	Fit on

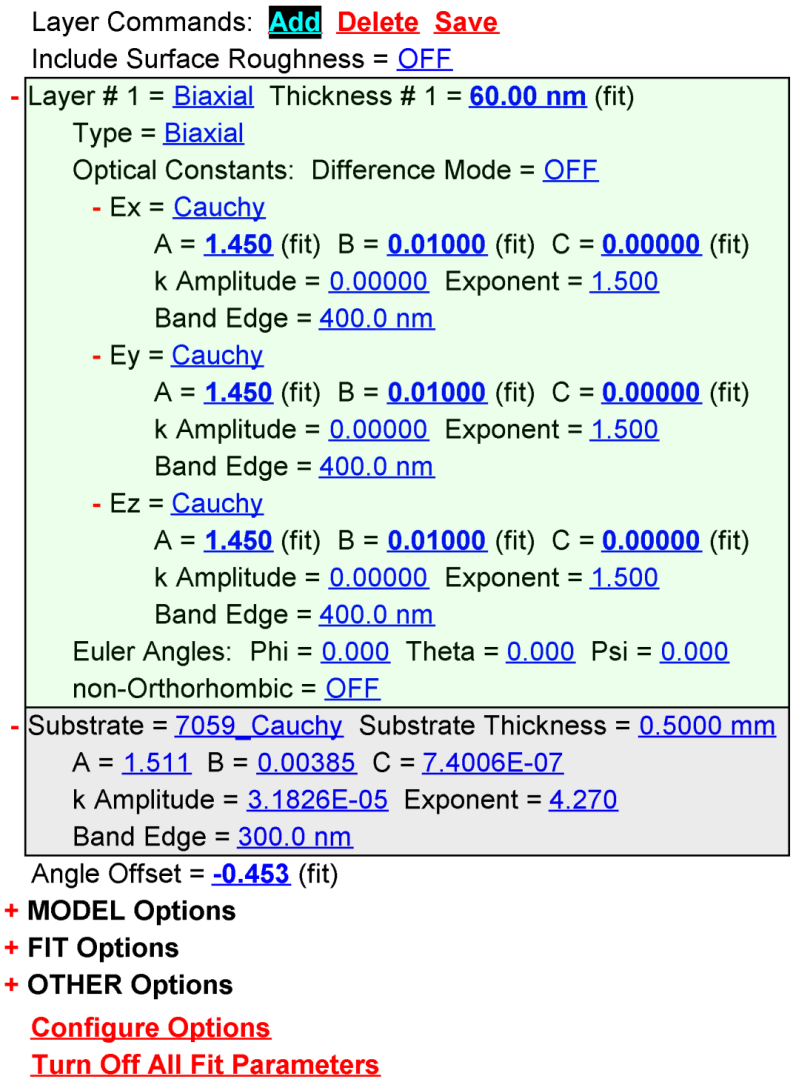

Figure 5.15: VASE Model for OAD TiO_2 single layer with fit on thickness, angle offset and Cauchy parameters of *A*, *B*, *C* in E_x-, E_y-, E_z-directions.

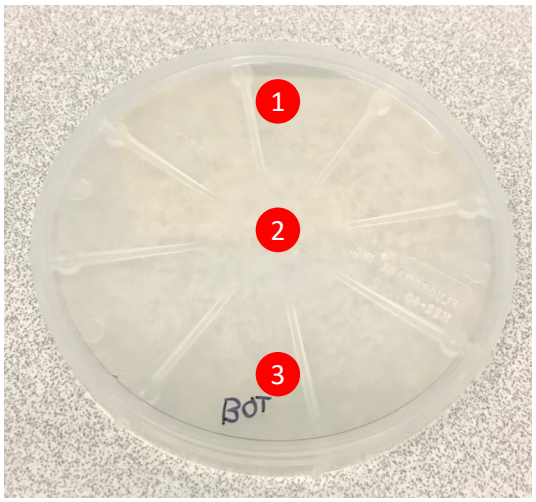

Figure 5.16: Three different spots 1, 2, 3 are measured along the film color variation.

the 'Euler Angles' were set to zero in order to extract permittivities in x-, y-, z-directions of laboratory frame in order to apply the permittivities into EMA theory (Sec. 2.6) for BHMM. Since the OAD TiO_2 layer on the wafer is not uniform because of the 70-degree stage, three measurements on different spot along the film color variation direction were required to check which spot is well matched with the input thickness (Fig. 5.16). After the measurements, optical constants of each of 'E_x', 'E_y', 'E_z' were saved separately in order to apply these data into EMA model in the biaxial HMM model. The fit results are described in Table 5.4. For the measurements on three different spots, thickness was fitted as 69.8 $\pm$ 0.7 nm with MSE of 2.22 for spot 1, 52.5 $\pm$ 1.3 nm with MSE of 3.19 for spot 2, and 47.2 $\pm$ 2.3 nm with MSE of 2.60 for spot 3. Δ and Ψ values of the three measurement spots are described in Figures 5.17-5.19. *N*, *C*, and *S* data of the three measurement spots are described in Figures 5.20-5.22. Optical constants of normal TiO_2 single layer were extracted as shown in Figures 5.23-5.25. Uniqueness fit on thickness was conducted as shown in Figures 5.26-5.28. The three results are similar one another with low MSE except thickness, and the target thickness of 60 nm exists between spot 1 and 2, so the results are reliable and applicable to BHMM fabrication.

Table 5.4: Fit results of OAD TiO_2 single layer.

	Measurement Spot 1	**Measurement Spot 2**	**Measurement Spot 3**
MSE	2.22	3.19	2.60
Thickness	69.8 ± 0.7 nm	52.5 ± 1.3 nm	47.2 ± 2.3 nm
$E_x(A)$	1.674 ± 0.02	1.619 ± 0.04	1.586 ± 0.04
$E_x(B)$	-0.0025 ± 0.006	0.0066 ± 0.01	0.0053 ± 0.01
$E_x(C)$	0.0037 ± 0.0007	0.0019 ± 0.001	0.0018 ± 0.001
$E_y(A)$	1.597 ± 0.02	1.517 ± 0.04	1.501 ± 0.05
$E_y(B)$	0.0169 ± 0.006	0.0310 ± 0.01	0.0263 ± 0.01
$E_y(C)$	0.0014 ± 0.0007	0.0002 ± 0.001	-0.0003 ± 0.001
$E_z(A)$	1.702 ± 0.06	1.657 ± 0.12	1.619 ± 0.13
$E_z(B)$	-0.0033 ± 0.02	-0.0020 ± 0.05	0.0007 ± 0.04
$E_z(C)$	0.0034 ± 0.003	0.0027 ± 0.005	0.0022 ± 0.004
Angle Offset	-0.5° ± 0.03°	-0.4° ± 0.02°	-0.4° ± 0.01°

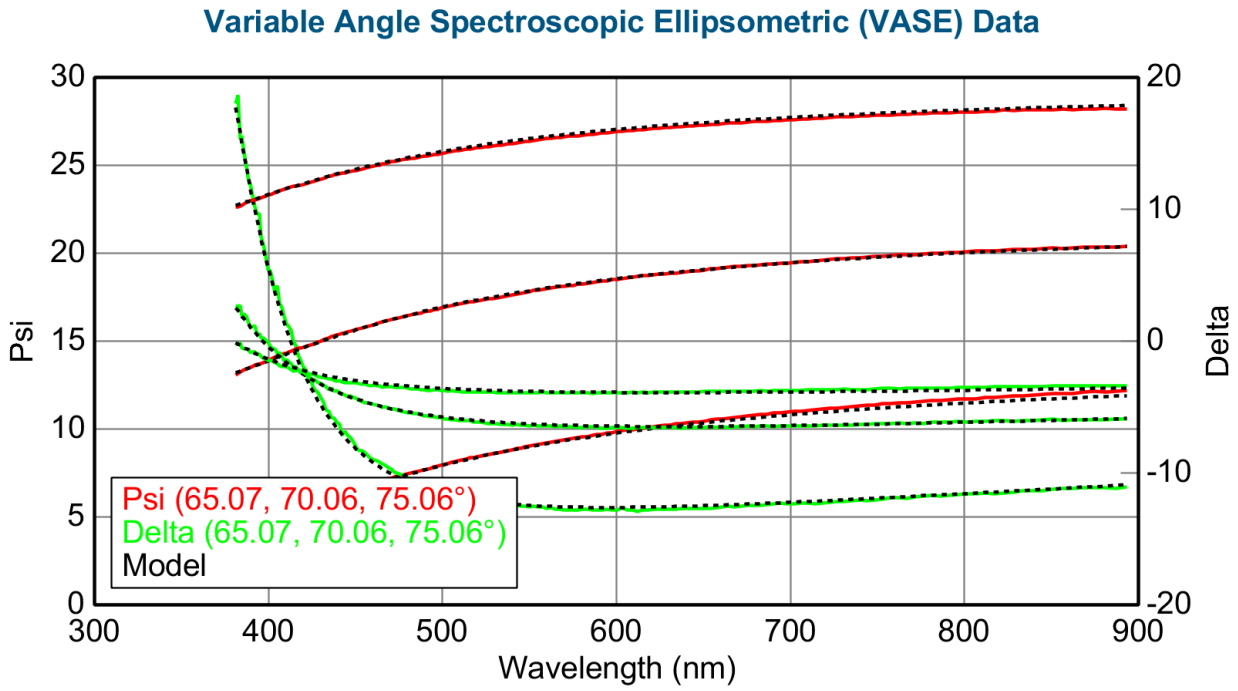

Figure 5.17: Δ and Ψ of OAD TiO_2 single layer at measurement spot 1.

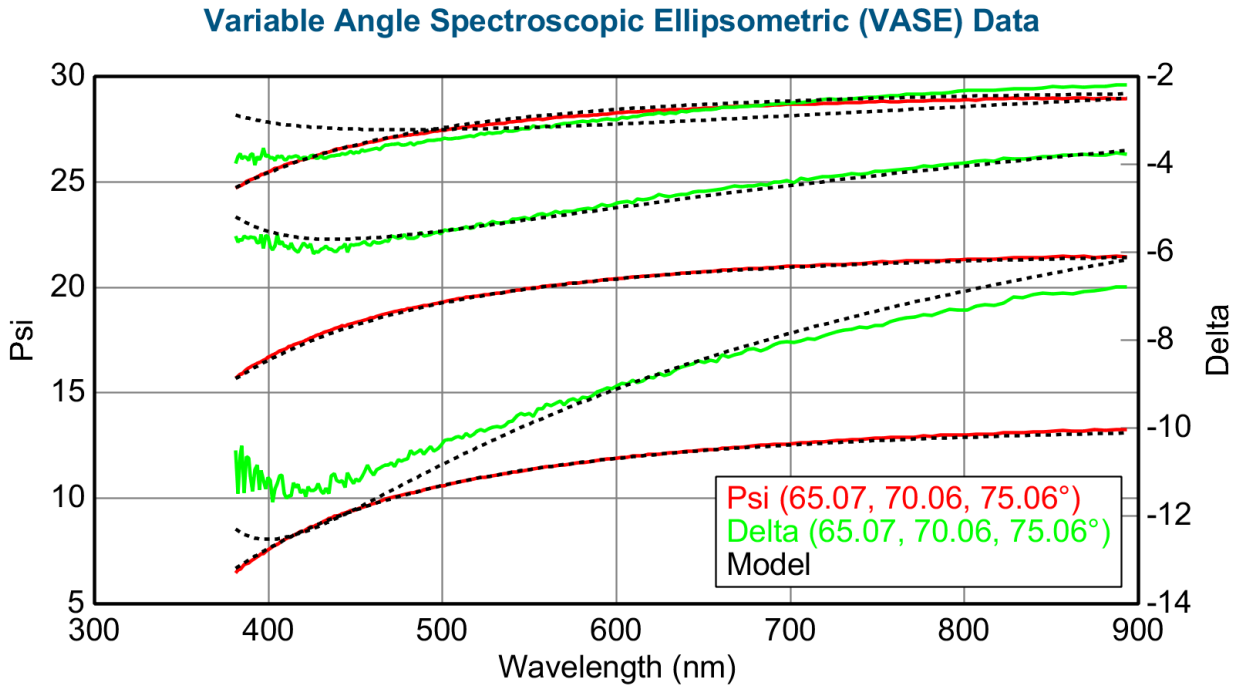

Figure 5.18: Δ and Ψ of OAD TiO_2 single layer at measurement spot 2.

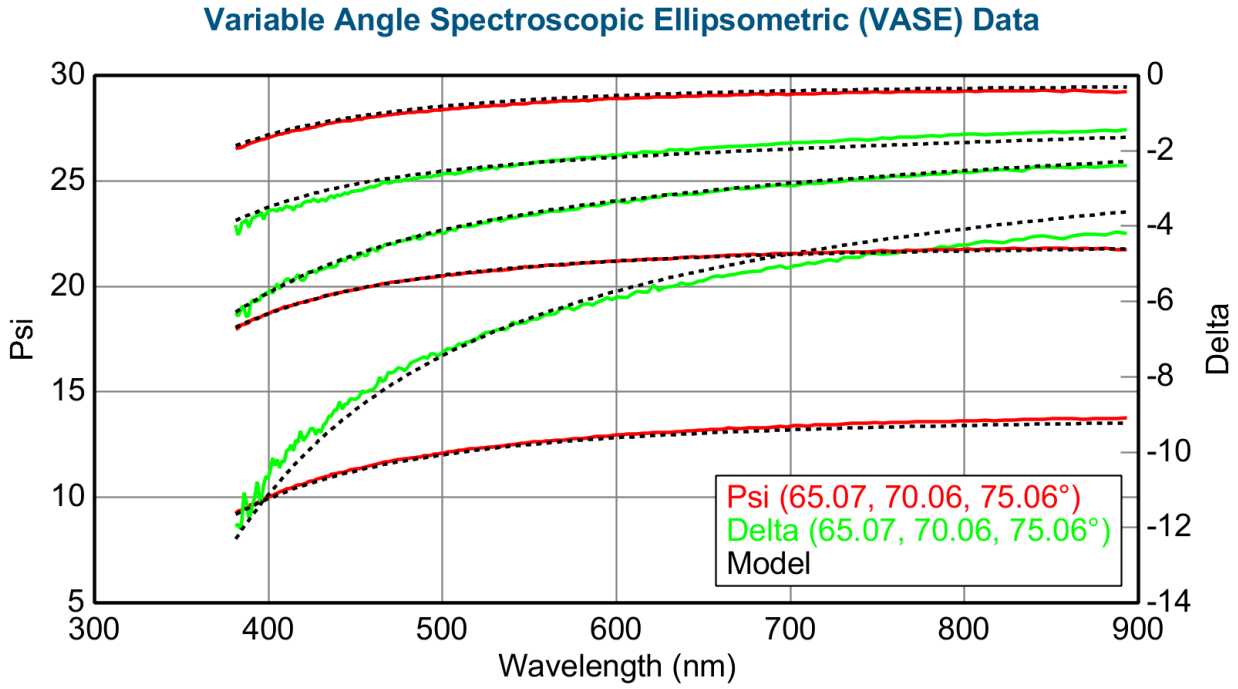

Figure 5.19: Δ and Ψ of OAD TiO_2 single layer at measurement spot 3.

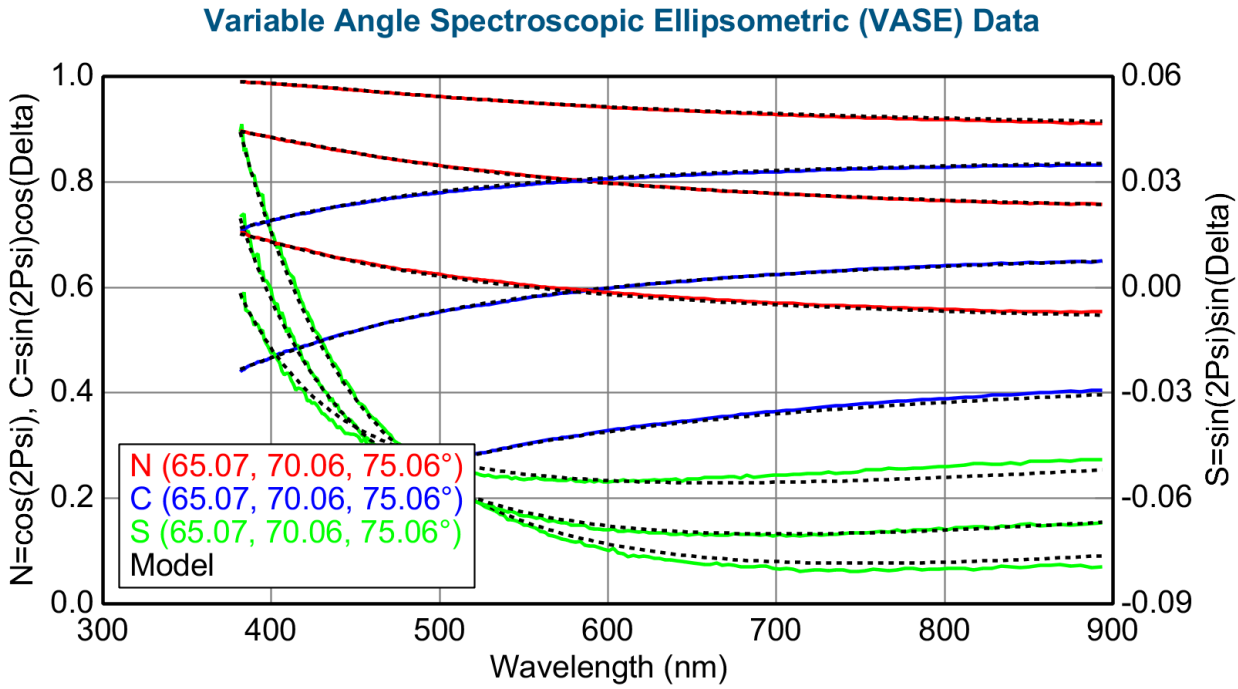

Figure 5.20: *N*, *C*, *S* data of OAD TiO_2 single layer at measurement spot 1.

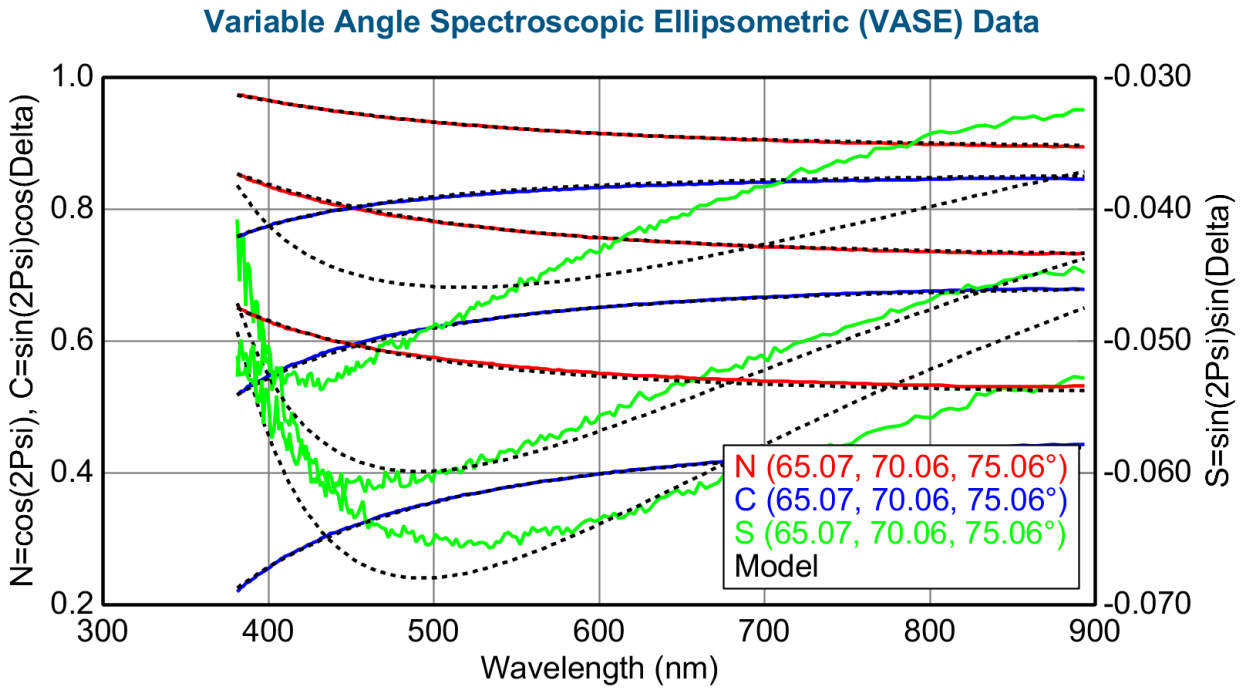

Figure 5.21: *N*, *C*, *S* **data of OAD TiO_2 single layer at measurement spot 2.**

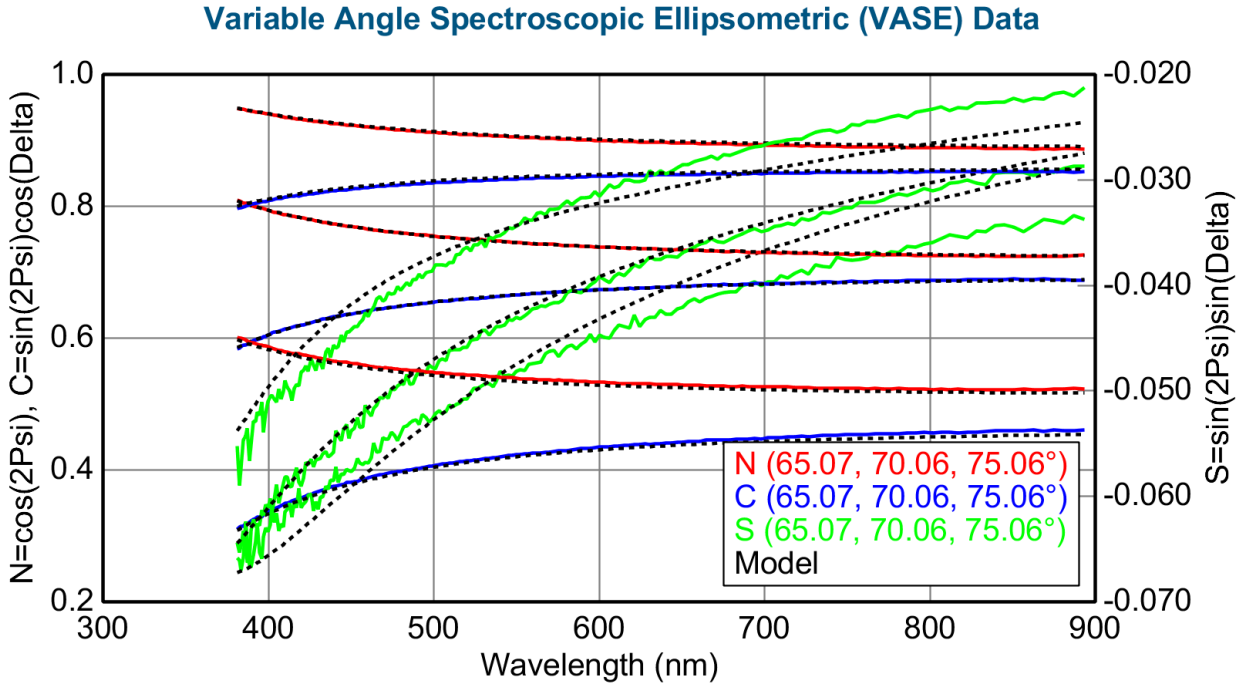

Figure 5.22: *N*, *C*, *S* **data of OAD TiO_2 single layer at measurement spot 3.**

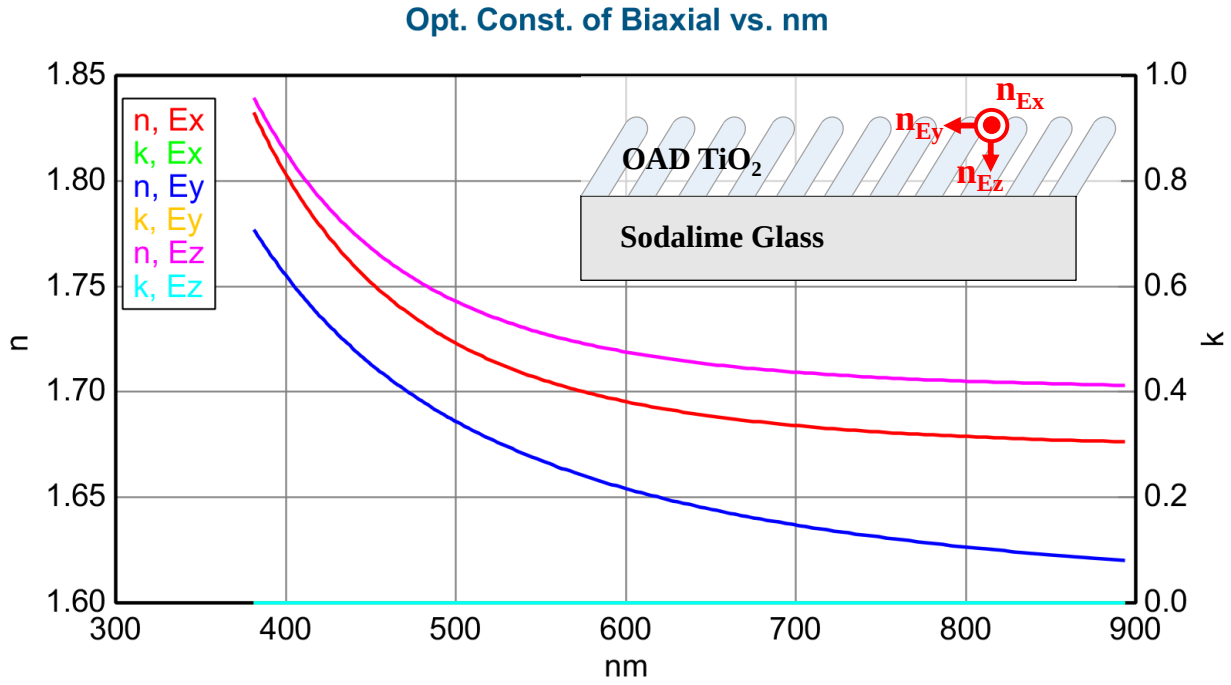

Figure 5.23: Optical constants of OAD TiO_2 single layer at measurement spot 1.

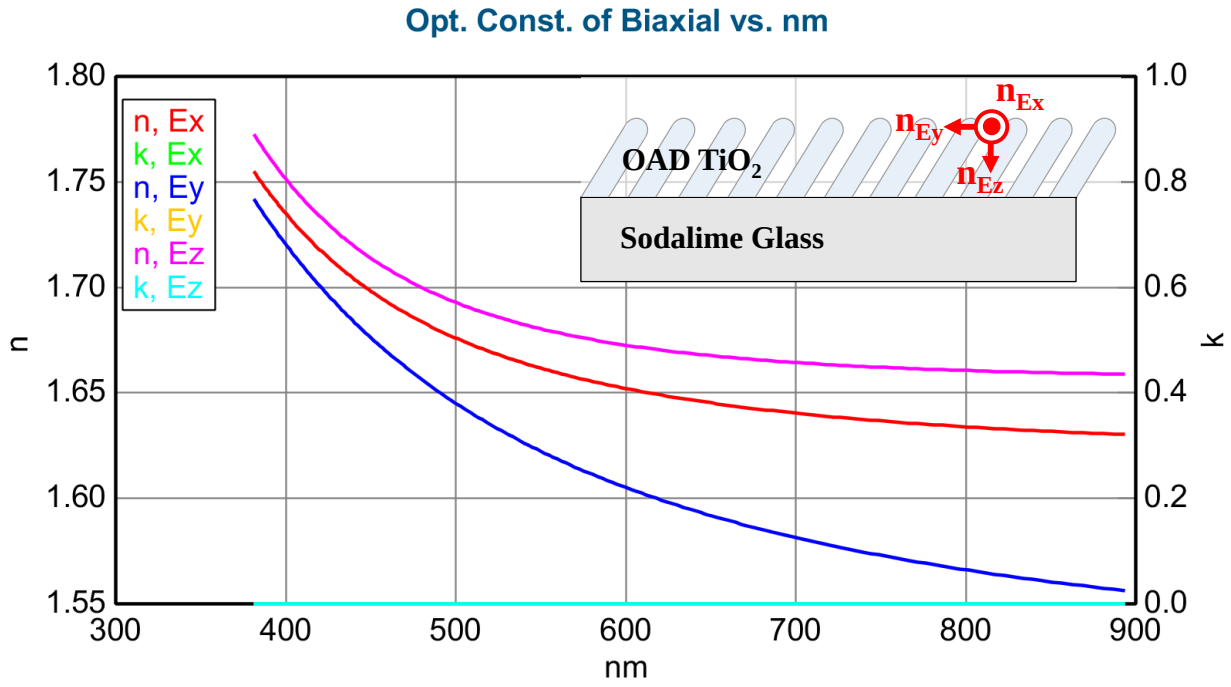

Figure 5.24: Optical constants of OAD TiO_2 single layer at measurement spot 2.

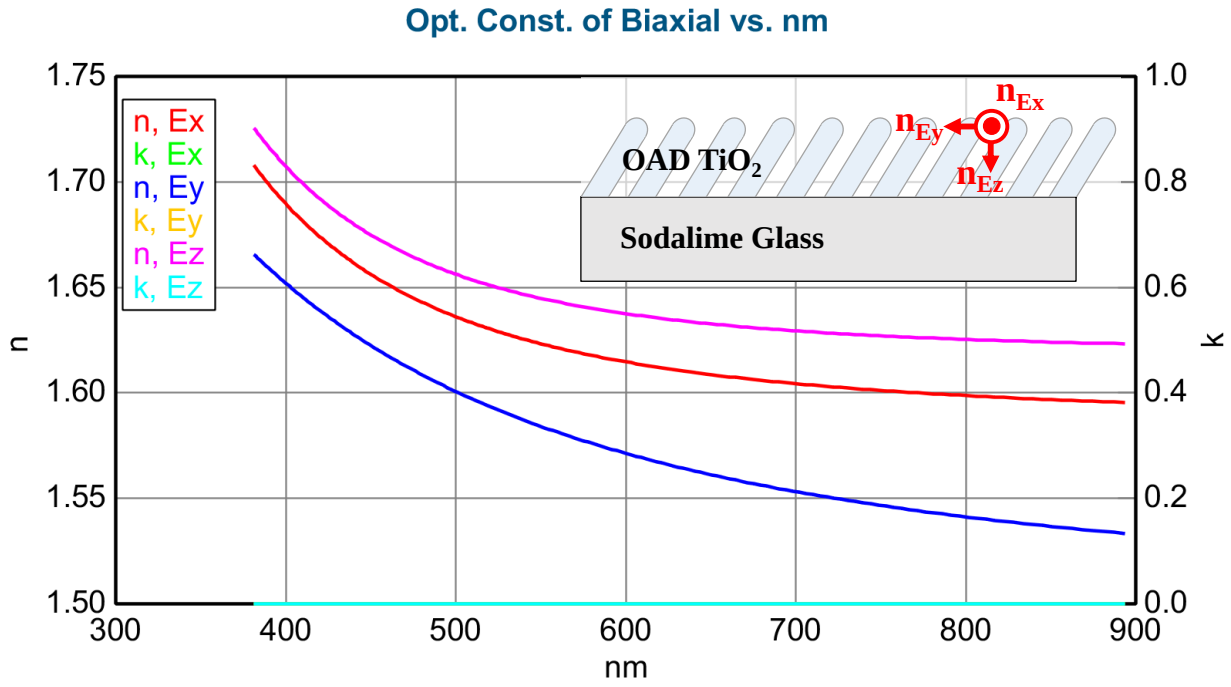

Figure 5.25: Optical constants of OAD TiO_2 single layer at measurement spot 3.

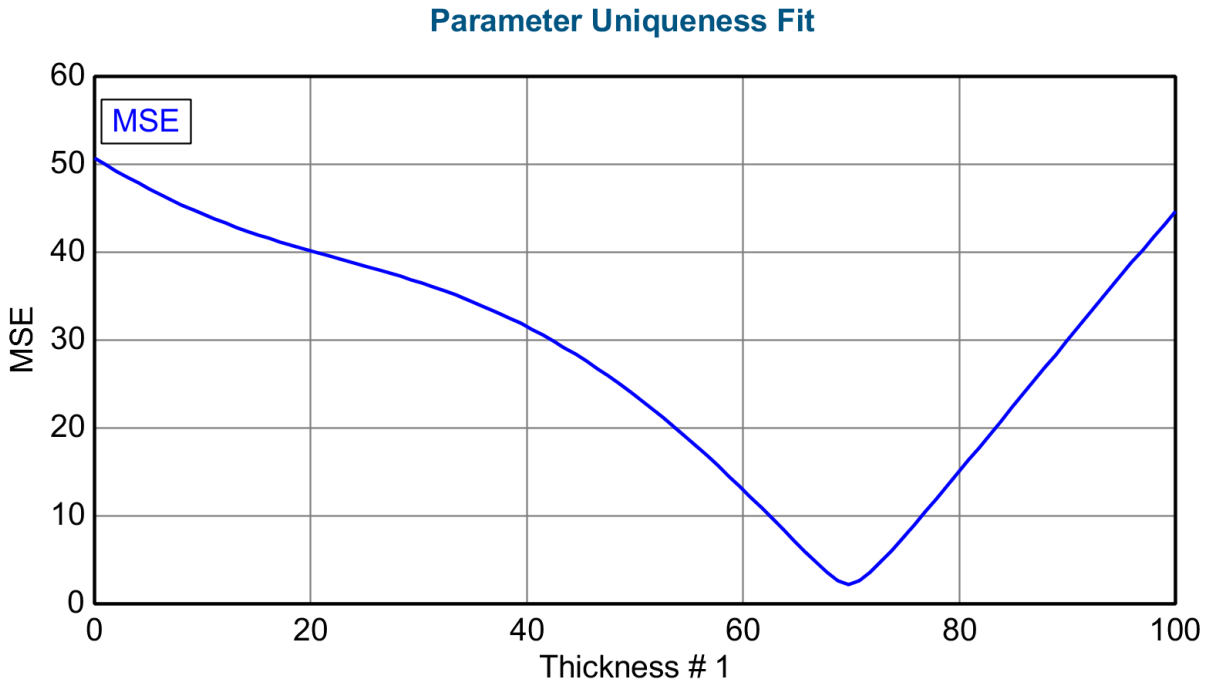

Figure 5.26: Uniqueness fit of OAD TiO_2 single layer from 0 to 100 nm at measurement spot 1.

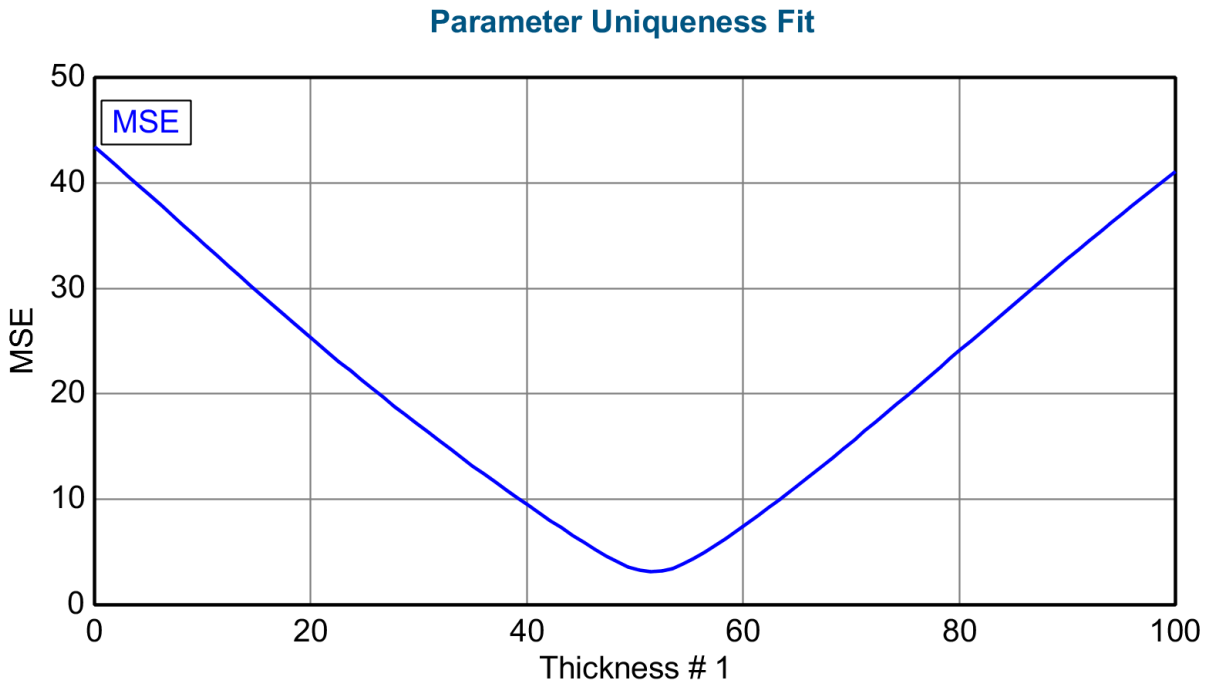

Figure 5.27: Uniqueness fit of OAD TiO_2 single layer from 0 to 100 nm at measurement spot 2.

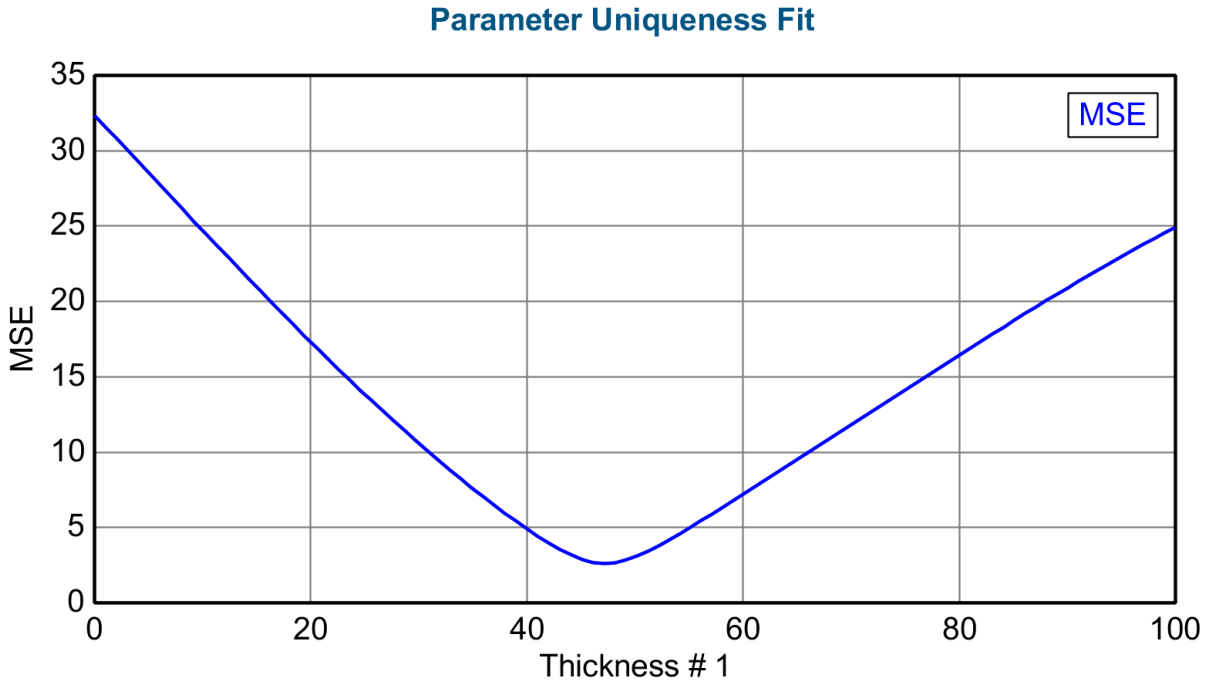

Figure 5.28: Uniqueness fit of OAD TiO_2 single layer from 0 to 100 nm at measurement spot 3.

5.1.3. Measurements of single Cu layer

In the design of biaxial HMM, 15 nm of ultra-thin Cu layer is required. However, absorbing ultra-thin materials such as the 15 nm Cu layer used to have different optical constants with those of bulk materials [49]. To overcome this problem, supplementing the spectroscopic ellipsometry (SE) data with intensity transmission data (T) is good solution since the extra data could give more unique results and reduce the model ambiguity for thickness and optical constants [26, 41]. A 15 nm Cu layer was deposited onto the transparent sodalime glass wafer, so the T measurement can be conducted via VASE system. Three angle measurement was carried out for SE data first, and then T data was measured via 'Transmission' mode at normal incidence in the VASE system. A total of three measurements on three different spots on the sample were conducted for data reliability. Details of the model parameters are provided in Fig. 5.29 and Table 5.5. After the SE measurements with the T data, 'Glass with Absorbing Film (with Backside reflection)' model was used in the model. The substrate of the transparent sodalime glass wafer was set to '7059_Cauchy' with 0.5 mm thickness in the 'Substrate' of the model. Default 'Cu.mat (From Palik I: pp. 284-

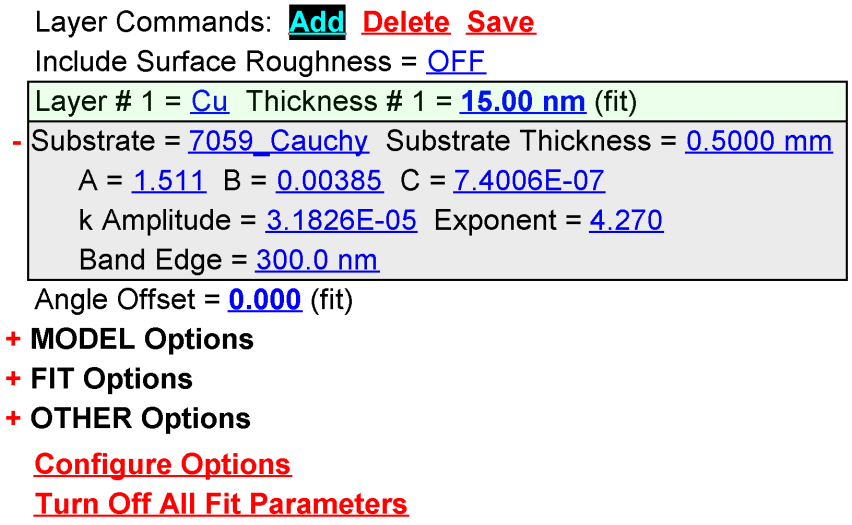

Figure 5.29: VASE Model for Cu single layer with fit on thickness and angle offset.

Table 5.5: VASE Model for Cu single layer.

Basic Model	Glass with Absorbing Film (with Backside reflection).mod
Layer 1	Cu.mat (From Palik I: pp. 284-285, 207-1823 nm)
Substrate	7059_Cauchy substrate, thickness : 0.5 mm
Angle Offset	Fit on

285, 207-1823 nm)' in the program was applied to the 'Layer 1' in the model. Then, 'Append Data' function in the program was utilized to add T data onto the SE data in order to fit on SE data and T data at the same time. Thickness of the 'Cu.mat' and 'Angle Offset' were being fitted. The fit results are described in Table 5.6. For the measurements on three different spots, thickness was fitted as 14.5 $\pm$ 0.02 nm with MSE of 9.06 for spot 1, 14.6 $\pm$ 0.02 nm with MSE of 9.15 for spot 2, and 14.3 $\pm$ 0.02 nm with MSE of 8.94 for spot 3. Δ and Ψ values of the three measurement spots are described in Figures 5.30-5.32. *N*, *C*, and *S* data of the three measurement spots are described in Figures 5.33-5.35. Transmission intensity data of the three measurement spots are shown in Figures 5.36-5.38. Optical constants of Cu single layer were extracted as shown in Figures 5.39-5.41. Uniqueness fit on thickness was conducted as shown in Figures 5.42-5.44. The three results are similar one another with low MSE except thickness, and the target thickness of 15 nm is well matched with ellipsometric measurements, so the results are reliable and applicable to BHMM fabrication.

Table 5.6: Fit results of Cu single layer.

	Measurement Spot 1	**Measurement Spot 2**	**Measurement Spot 3**
MSE	9.06	9.15	8.94
Thickness	14.5 $\pm$ 0.02 nm	14.6 $\pm$ 0.02 nm	14.3 $\pm$ 0.02 nm
Angle Offset	0.6° $\pm$ 0.01°	0.7° $\pm$ 0.01°	0.7° $\pm$ 0.01°

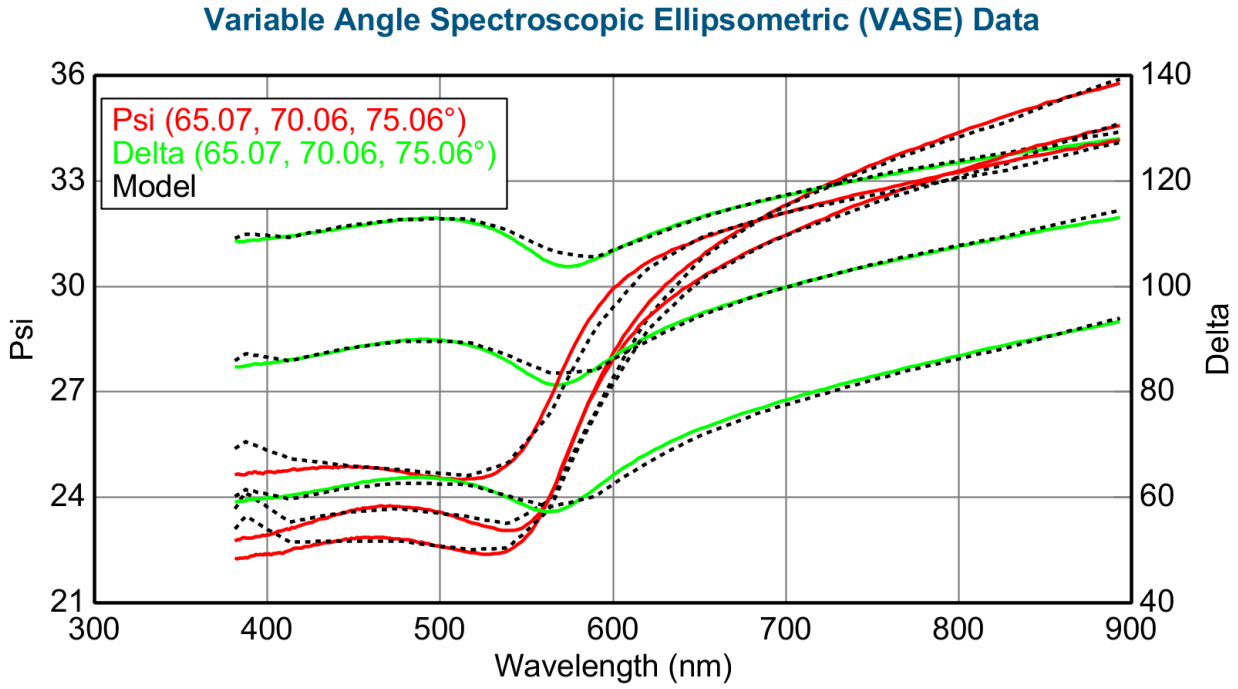

Figure 5.30: Δ and Ψ of Cu single layer at measurement spot 1.

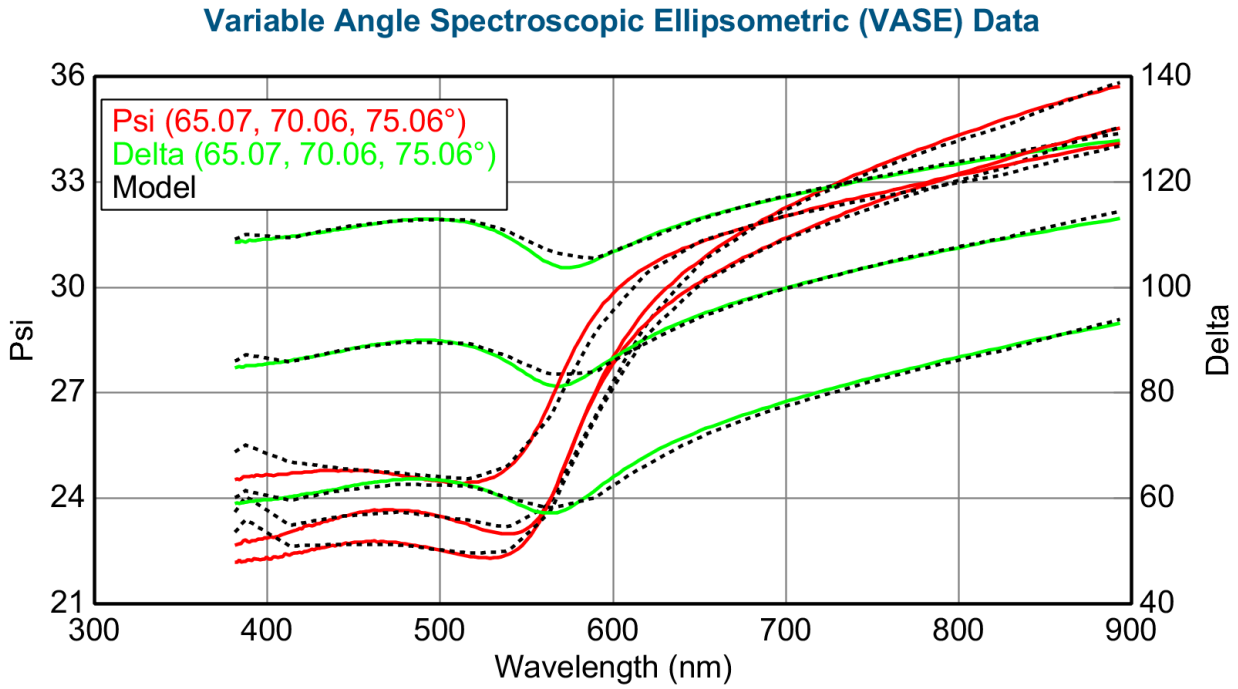

Figure 5.31: Δ and Ψ of Cu single layer at measurement spot 2.

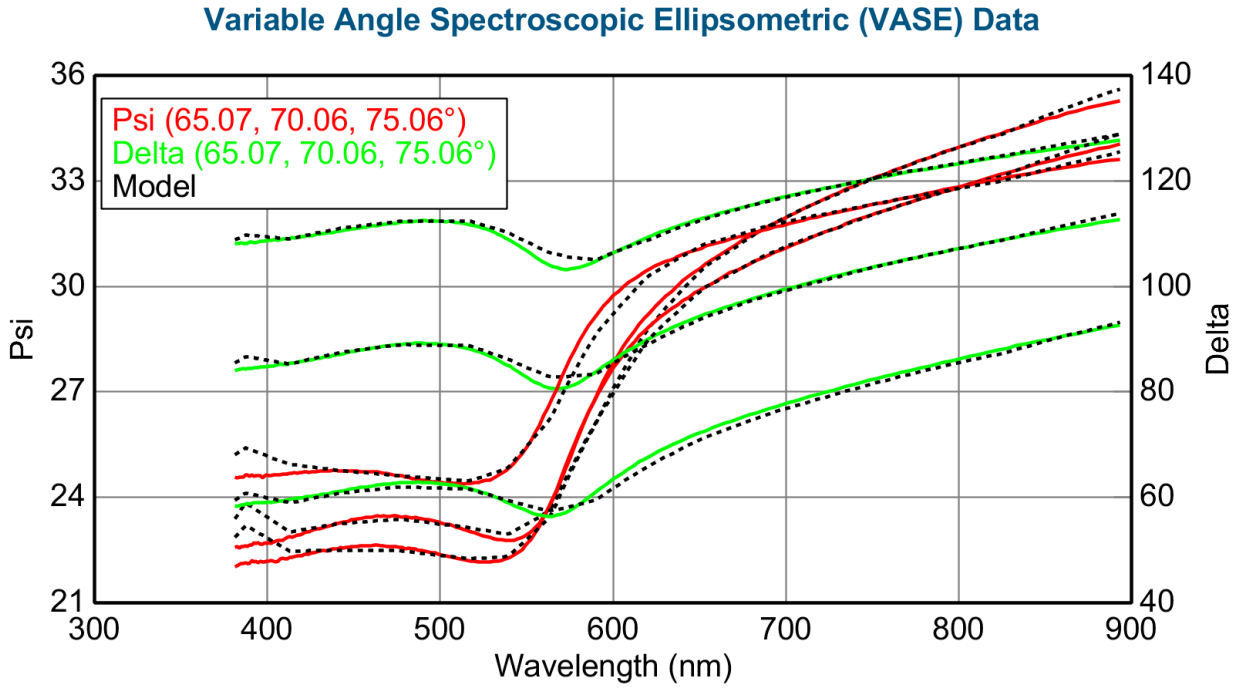

Figure 5.32: Δ and Ψ of Cu single layer at measurement spot 3.

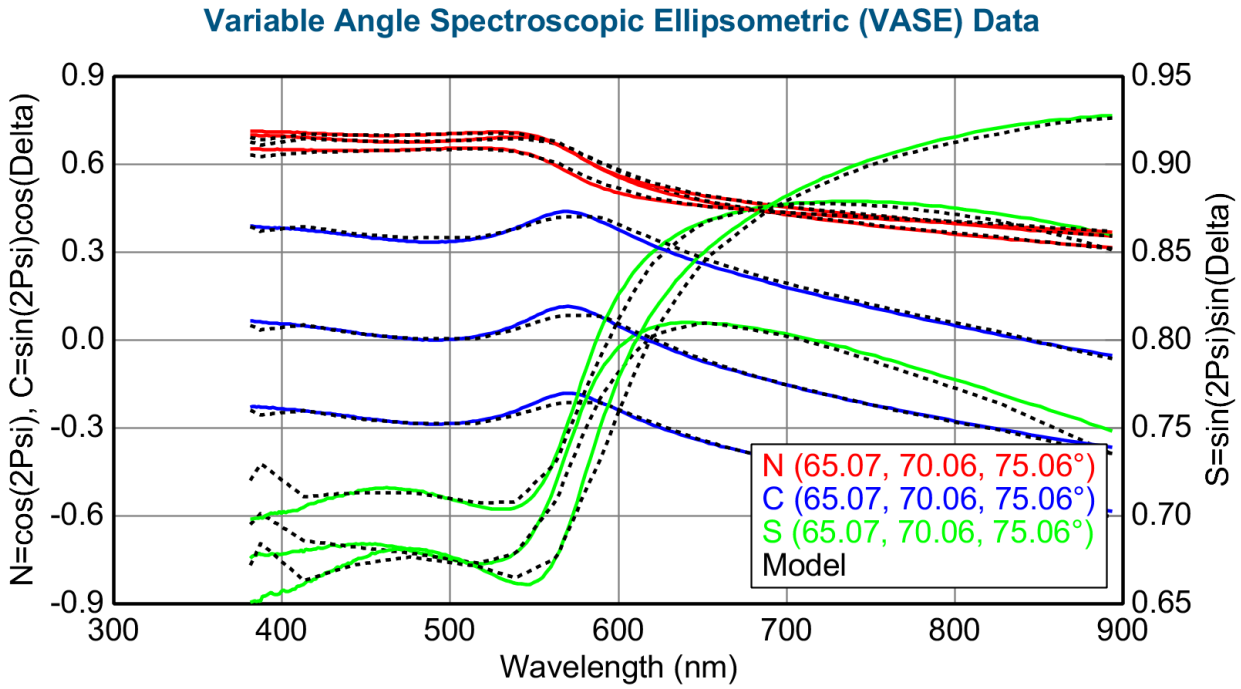

Figure 5.33: *N*, *C*, *S* data of Cu single layer at measurement spot 1.

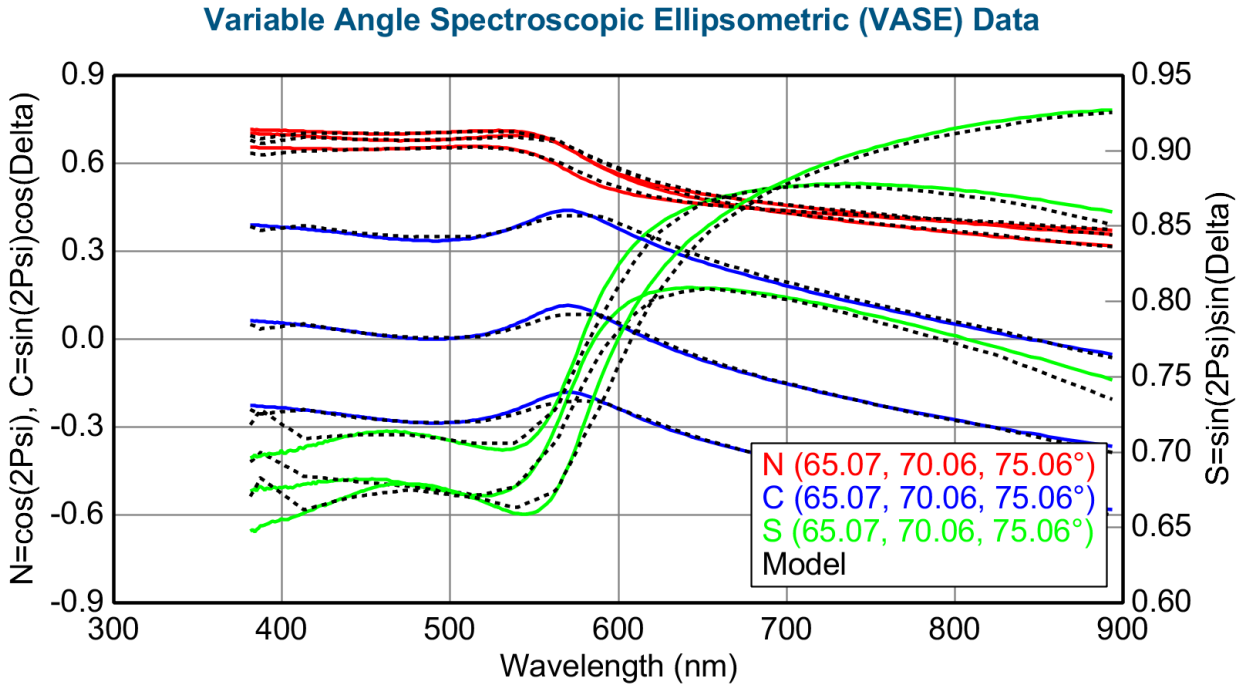

Figure 5.34: *N*, *C*, *S* **data of Cu single layer at measurement spot 2.**

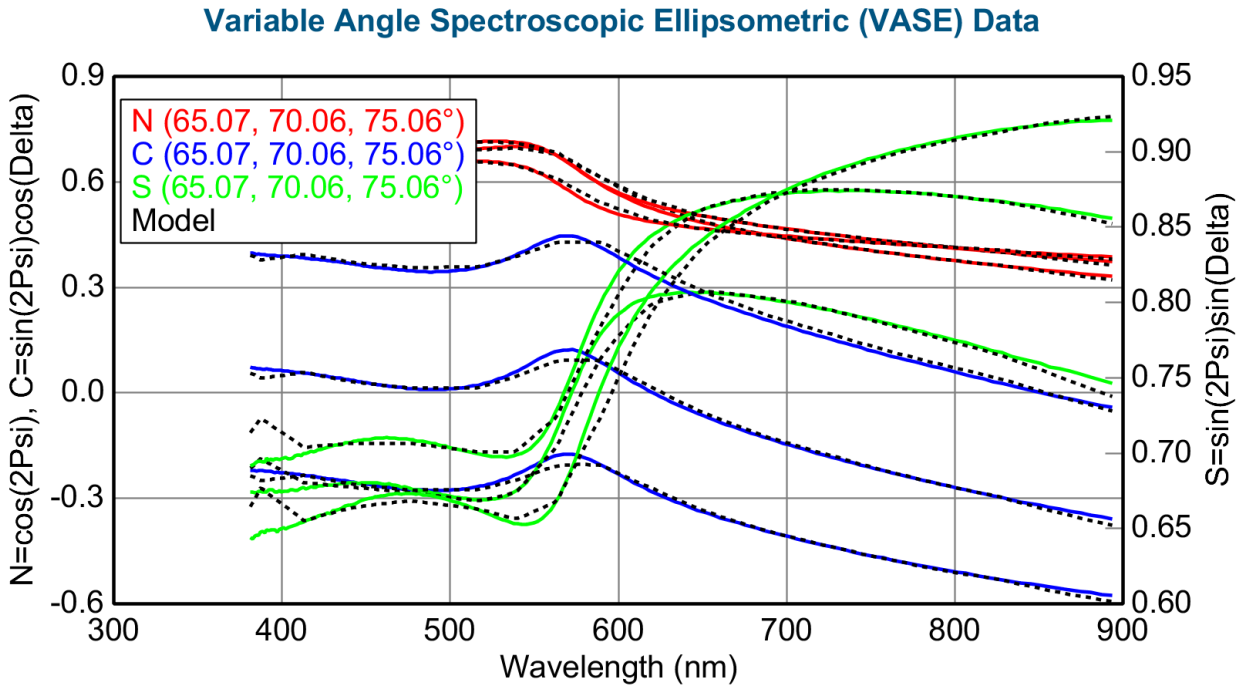

Figure 5.35: *N*, *C*, *S* **data of Cu single layer at measurement spot 3.**

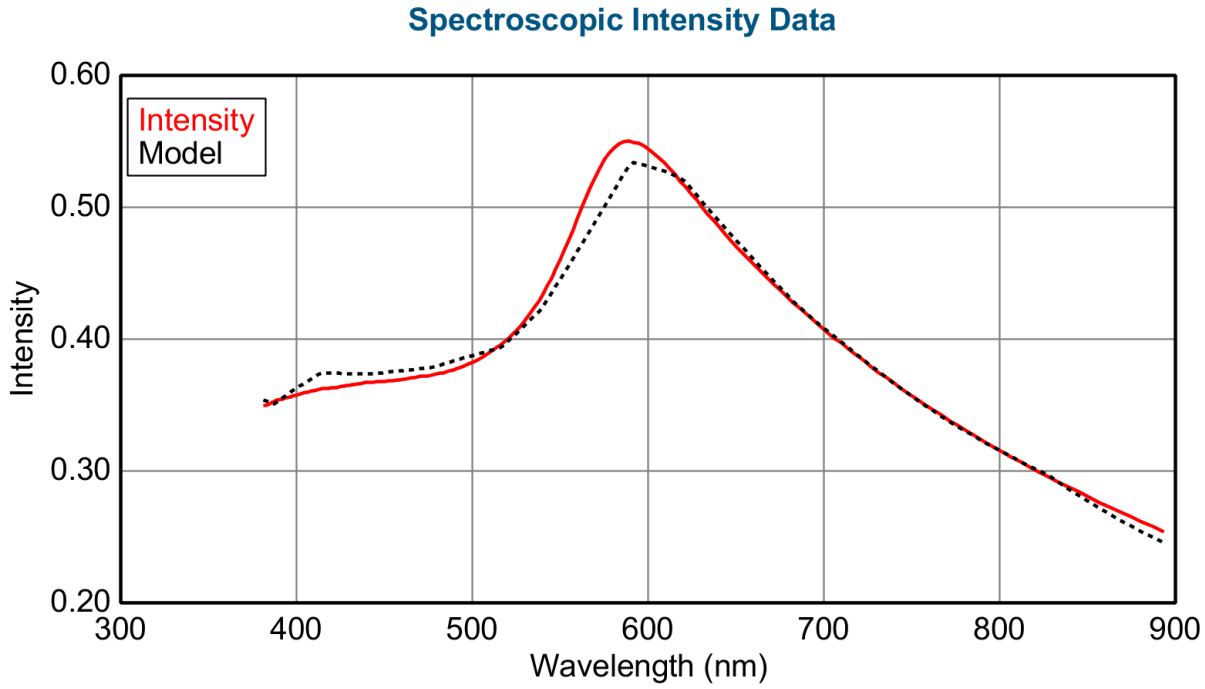

Figure 5.36: Transmission Intensity data of Cu single layer at measurement spot 1.

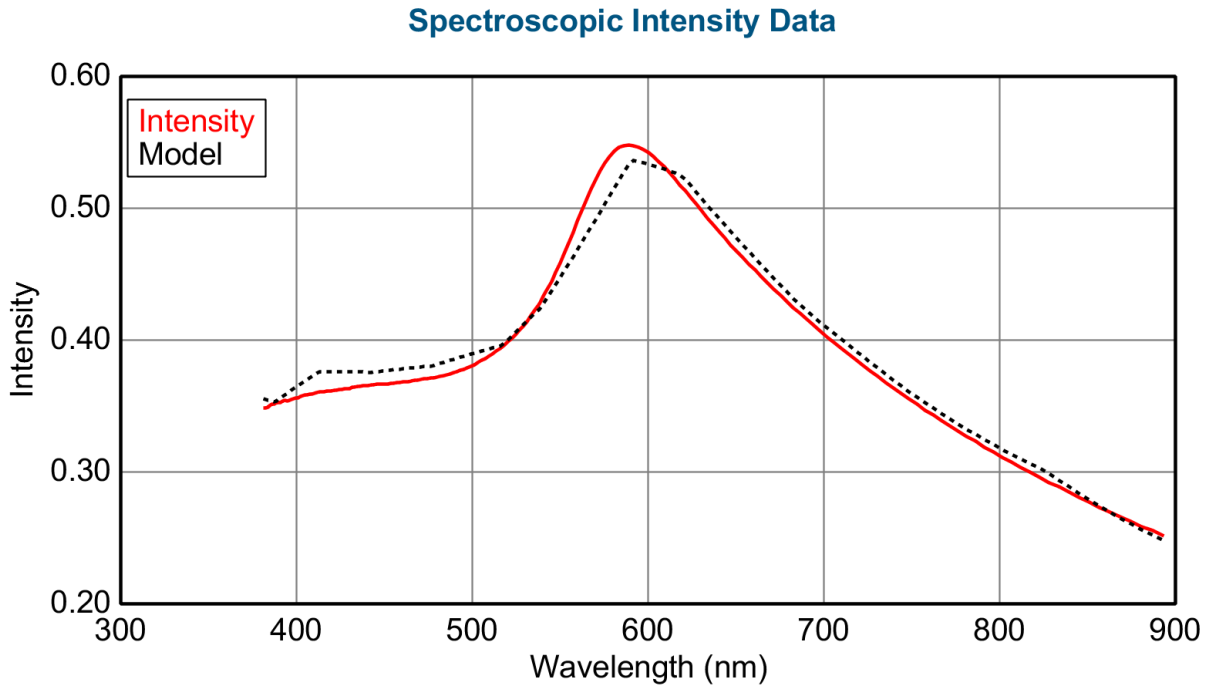

Figure 5.37: Transmission Intensity data of Cu single layer at measurement spot 2.

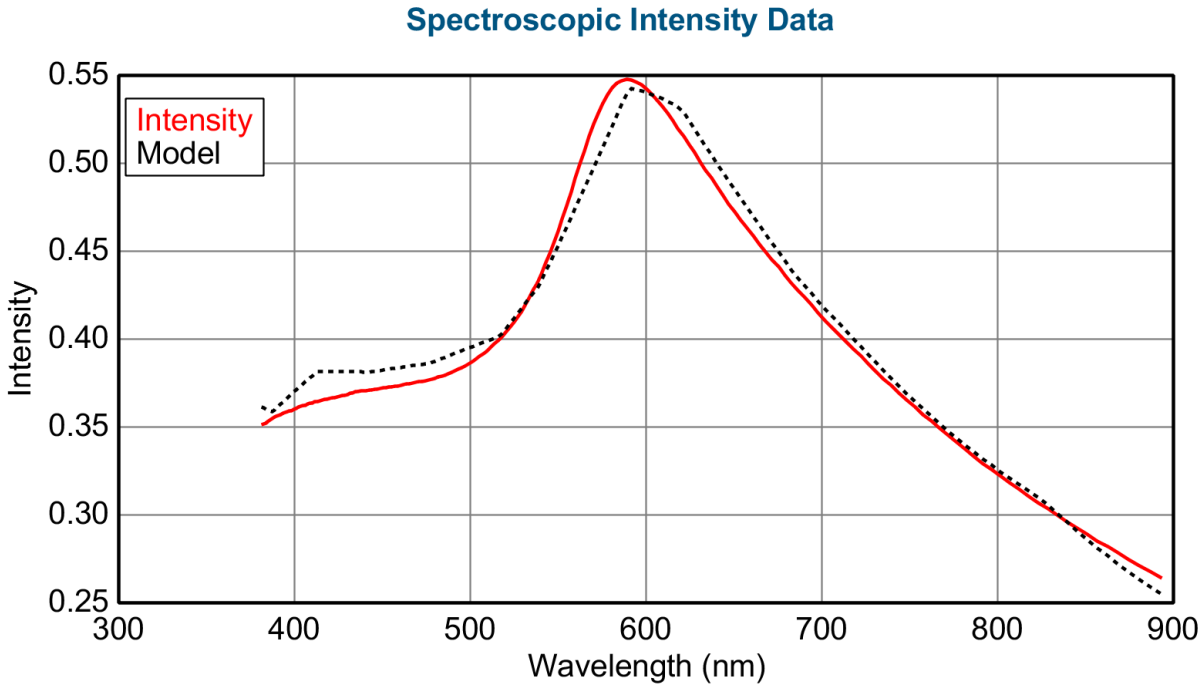

Figure 5.38: Transmission Intensity data of Cu single layer at measurement spot 3.

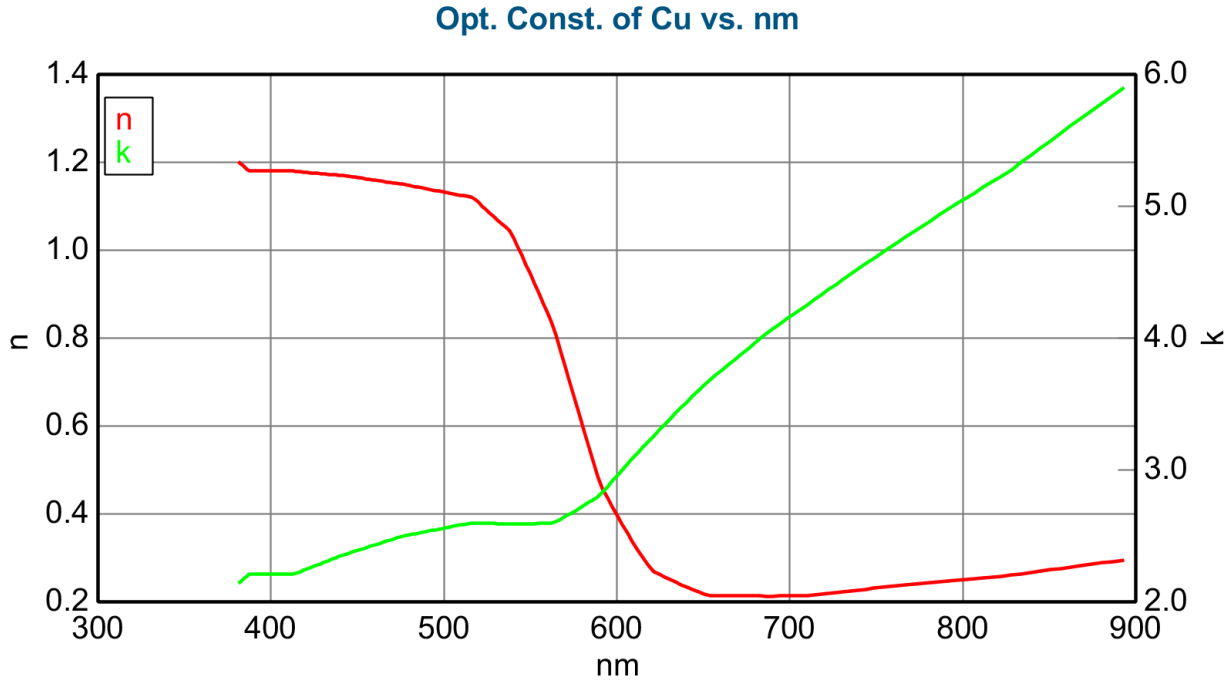

Figure 5.39: Optical constants of Cu single layer at measurement spot 1.

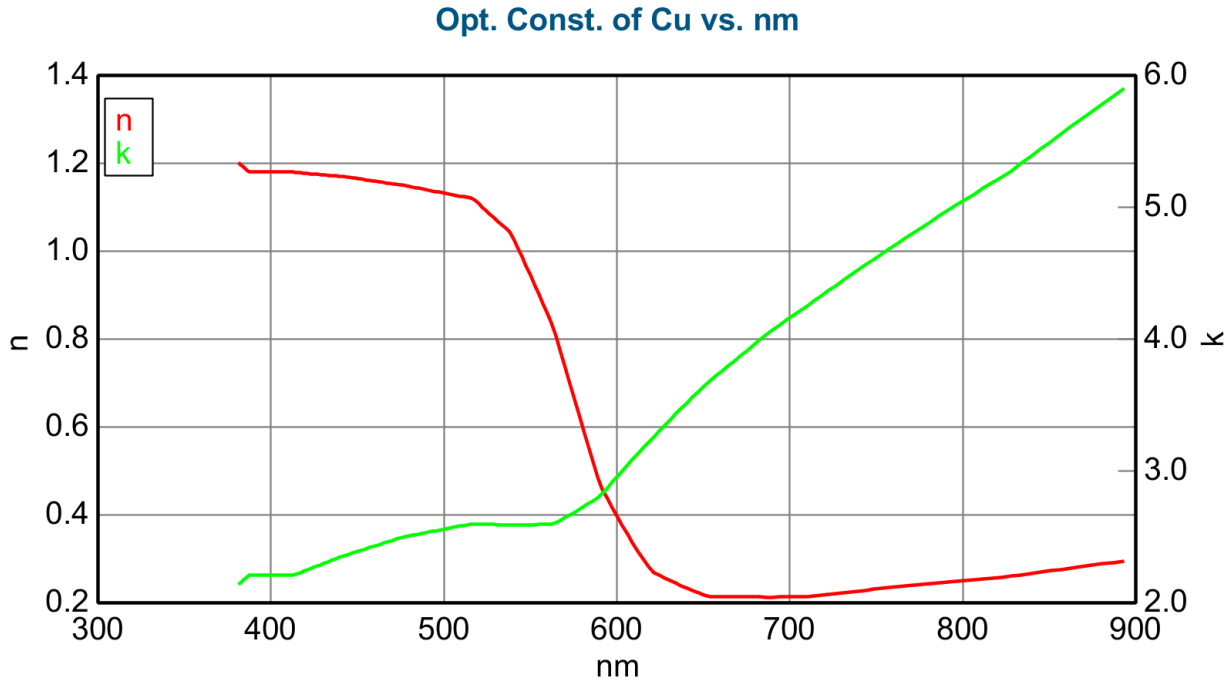

Figure 5.40: Optical constants of Cu single layer at measurement spot 2.

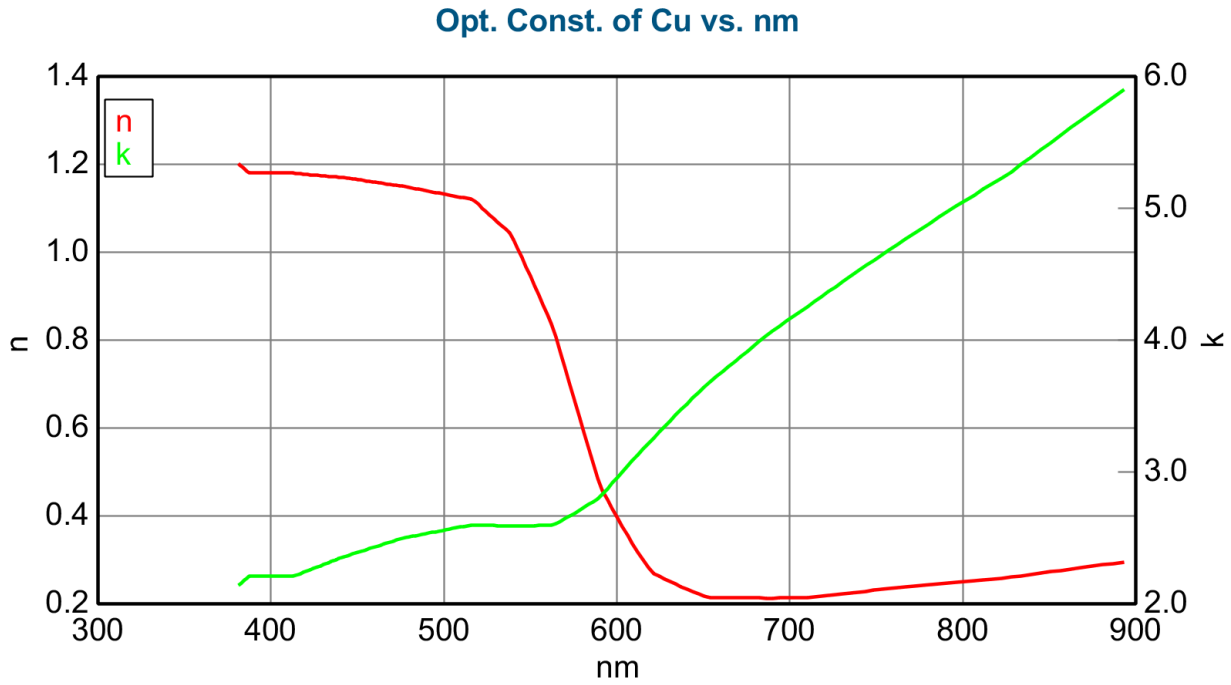

Figure 5.41: Optical constants of Cu single layer at measurement spot 3.

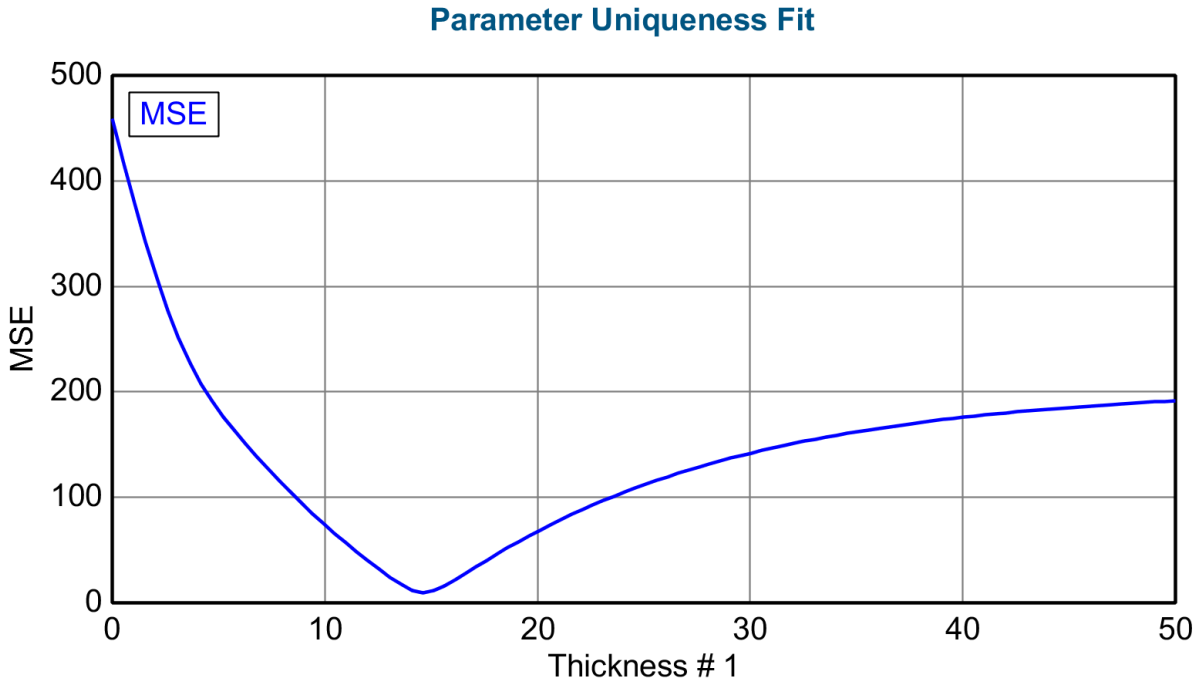

Figure 5.42: Uniqueness fit of Cu single layer from 0 to 50 nm at measurement spot 1.

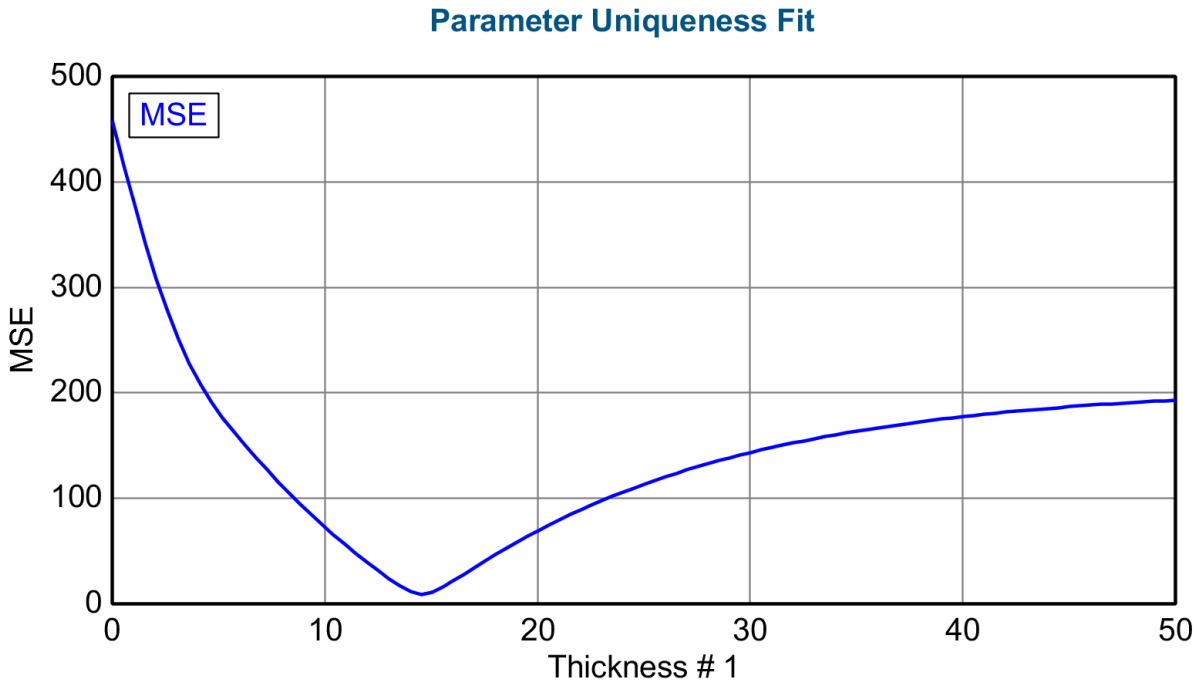

Figure 5.43: Uniqueness fit of Cu single layer from 0 to 50 nm at measurement spot 2.

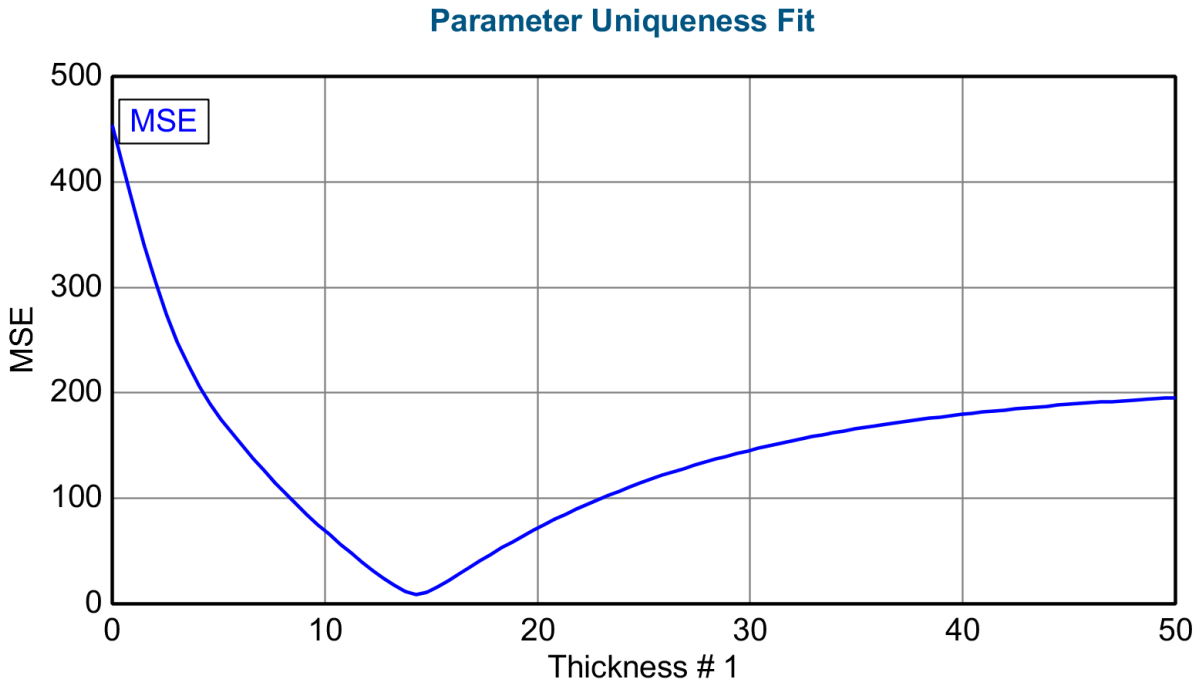

Figure 5.44: Uniqueness fit of Cu single layer from 0 to 50 nm at measurement spot 3.

5.1.4. Measurements of Biaxial Hyperbolic Metamaterials (BHMMs)

Fabricated biaxial hyperbolic metamaterial (BHMM) composed of OAD TiO_2 and Cu on top of a Si wafer was measured via VASE. Among the fabrication process, 15 nm of Cu layer was firstly deposited onto the Si wafer. Just after the deposition, the Cu layer was measured and analyzed with VASE three angle measurement for the credibility of the layer. Then, OAD TiO_2 layer was deposited onto the Cu layer and biaxial HMM was finally fabricated. The model parameters are provided in Fig. 5.45 and Table 5.7. Three angle measurement (65-, 70-, 75-degree) was conducted and a large number of VASE data was gathered along the direction of color variation in order to find out designed thickness of 75 nm (15 nm of Cu and 60 nm of OAD TiO_2). In the model, substrate was set as default Si substrate in the CompleteEASE program called 'Si_JAW.mat (Si substrate, Herzinger et al., (multi-wavelength, multi-sample analysis))'. Next, 'Biaxial' was applied to the 'Layer 1' and 'E_x', 'E_y', 'E_z' terms can be seen in the 'Biaxial' layer. Then, 'EMA'

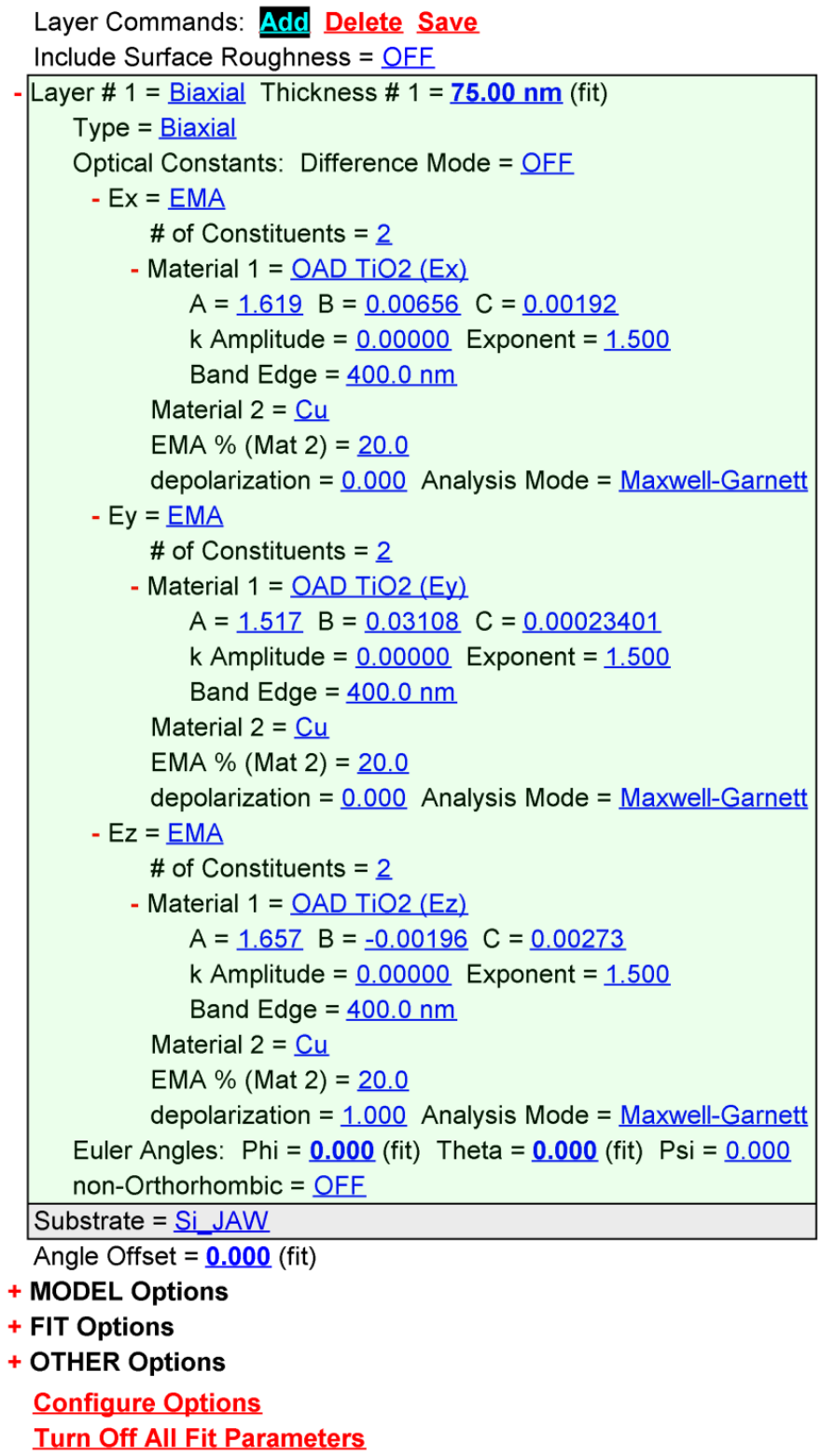

Figure 5.45: VASE Model for fabricated BHMM with fit on thickness, angle offset, phi and theta.

Table 5.7: VASE Model for fabricated BHMM.

Layer 1	Biaxial E_x = EMA (# of Consitituents = 2, Material 1 = OAD TiO_2 (E_x) (Fig. 5.23), Material 2 = Cu, EMA % = 20.0, Depolarization = 0, Analysis Mode = Maxwell-Garnett) E_y = EMA (# of Consitituents = 2, Material 1 = OAD TiO_2 (E_y) (Fig. 5.23), Material 2 = Cu, EMA % = 20.0, Depolarization = 0, Analysis Mode = Maxwell-Garnett) E_z = EMA (# of Consitituents = 2, Material 1 = OAD TiO_2 (E_z) (Fig. 5.23), Material 2 = Cu, EMA % = 20.0, Depolarization = 1, Analysis Mode = Maxwell-Garnett)
Substrate	Si_JAW
Euler Angles	Fit on ϕ (Phi) and θ (Theta)
Angle Offset	Fit on

was put to all the 'E_x', 'E_y', 'E_z' terms. ' of Constituents' was filled with '2' since the biaxial HMM is composed of Cu and OAD TiO_2. As optical constants of 'E_x', 'E_y', 'E_z' of OAD TiO_2 single layer were previously extracted in the Sec. 5.1.2, each of these data was applied to 'E_x', 'E_y', 'E_z' in the 'Material 1' of the 'Biaxial' layer. In the 'Material 2', default 'Cu.mat (From Palik I: pp. 284-285, 207-1823 nm)' was used to all the 'E_x', 'E_y', 'E_z'. 'EMA % (Mat 2)' in the 'E_x', 'E_y', 'E_z' was all set to '20.0' since designed thicknesses for Cu and OAD TiO_2 are 15 nm and 60 nm each. The 'depolarization' in the 'E_x', 'E_y', 'E_z' is screening factor which was covered in the Sec. 2.6. '0' was put into the 'E_x'-, 'E_y'-directions which are parallel to the planar structure, and '1' was put into the 'E_z'-direction which are normal to the planar structure. 'Maxwell-Garnett' EMA model was applied to 'Analysis Mode' in the 'E_x', 'E_y', 'E_z'. 'Phi' and 'Theta' in 'Euler Angles' and 'Angle Offset' were being fitted. Total five measurements were conducted for the data reliability (Fig. 5.46). The fit results are described in Table 5.8.

For the measurements on the five different spots, thickness was fitted as 78.8 $\pm$ 0.2 nm with MSE of 19.58 for spot 1, 77.9 $\pm$ 0.2 nm with MSE of 19.04 for spot 2, 78.3 $\pm$ 0.2 nm with MSE

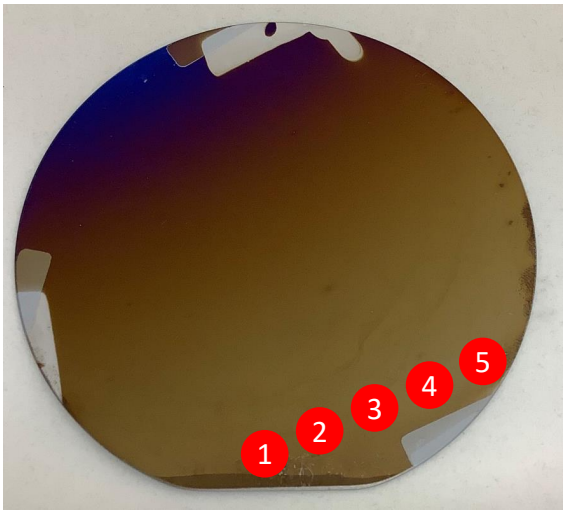

Figure 5.46: VASE measurements on five spots of the fabricated BHMM.

Table 5.8: Fit results of fabricated BHMM.

	Measurement Spot 1	**Measurement Spot 2**	**Measurement Spot 3**	**Measurement Spot 4**	**Measurement Spot 5**
MSE	19.58	19.04	18.99	19.01	18.72
Thickness	78.8 ± 0.2 nm	77.9 ± 0.2 nm	78.3 ± 0.2 nm	78.9 ± 0.2 nm	78.6 ± 0.2 nm
Phi	-23.9° ± 0.5°	-24.4° ± 0.5°	-23.7° ± 0.5°	-22.6° ± 0.5°	-22.0° ± 0.5°
Theta	-32.8° ± 0.1°	-32.4° ± 0.1°	-32.4° ± 0.1°	-32.4° ± 0.1°	-32.1° ± 0.1°
Angle Offset	1.4° ± 0.1°	1.4° ± 0.1°	1.5° ± 0.1°	1.5° ± 0.1°	1.5° ± 0.1°

of 18.99 for spot 3, 78.9 ± 0.2 nm with MSE of 19.01 for spot 4, and 78.6 ± 0.2 nm with MSE of 18.72 for spot 5. The measured thicknesses are well matched with designed thickness of 75 nm. The MSE values around 19 are acceptable for biaxial sample since biaxial materials used to be more complex than isotropic or uniaxial materials.

The Euler angles were obtained as ϕ = -23.9° ± 0.5° and θ = -32.8° ± 0.1° for spot 1, ϕ = -24.4° ± 0.5° and θ = -32.4° ± 0.1° for spot 2, ϕ = -23.7° ± 0.5° and θ = -32.4° ± 0.1° for spot 3, ϕ = -22.6° ± 0.5° and θ = -32.4° ± 0.1° for spot 4, and ϕ = -22.0° ± 0.5° and θ = -32.1° ± 0.1° for spot 5. As Euler angles were covered in Sec. 2.8, the ϕ is related to x- and y-axes rotation around z-axis. Thus, fitted ϕ data which was obtained in the VASE measurements could be explained as sample misalignment on the VASE stage, and the fitted ϕ values are relatively small, so the values are acceptable. The θ data is related to rotation of y'- and z-axes about x'-axis (Fig. 2.9). The fitted θ values might come from non-uniform thickness of OAD TiO_2 layer throughout the wafer because of the 70-degree stage, or surface roughness of nanocolumnar structures, or the 51° slanted OAD TiO_2 nanocolumnar structures with tilted anisotropic ellipsoid (Fig. 2.1). For the Euler angles measurements, it is suggested to conduct rotational Mueller Matrix scan in VASE measurements [41], however, our group does not have VASE with the rotational Mueller Matrix scan function. Δ and Ψ values of the five measurement spots are described in Fig-

ures 5.47-5.51. *N*, *C*, and *S* data of the five measurement spots are described in Figures 5.52-5.56. Permittivities of BHMM were extracted as shown in Figures 5.57-5.61. In the figures, Epsilon-Near-Zero (ENZ) is placed at around 625 nm and the difference between E_x and E_y values at 625 nm is 0.13 ± 0.001. In addition, dual ENZ regions which are separated by 6.7 nm were observed. Above 625 nm, the fabricated BHMM acts as Type II biaxial hyperbolic metamaterials as its real in-plane permittivities (x- and y-directions) are negative and out-of-plane permittivity (z-direction) is positive. Uniqueness fit on thickness was conducted as shown in Figures 5.62-5.66. The five results are similar one another with acceptable MSE, so the fit results are reliable.

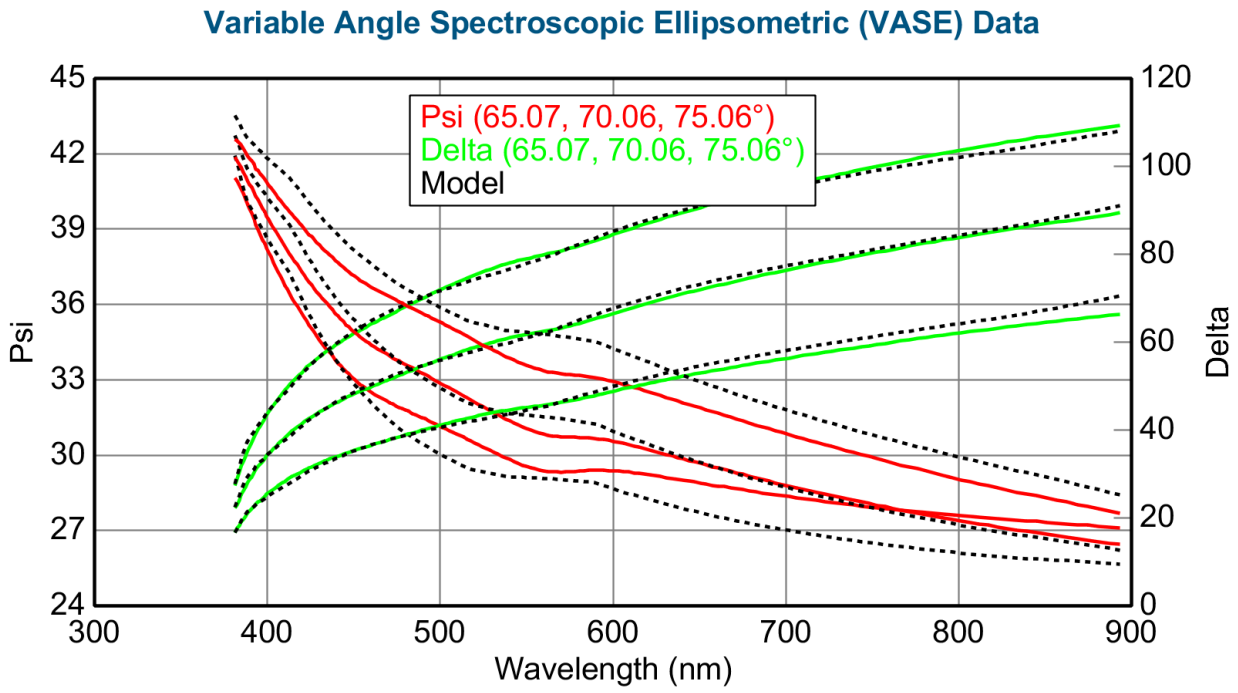

Figure 5.47: Δ and Ψ of fabricated BHMM at measurement spot 1.

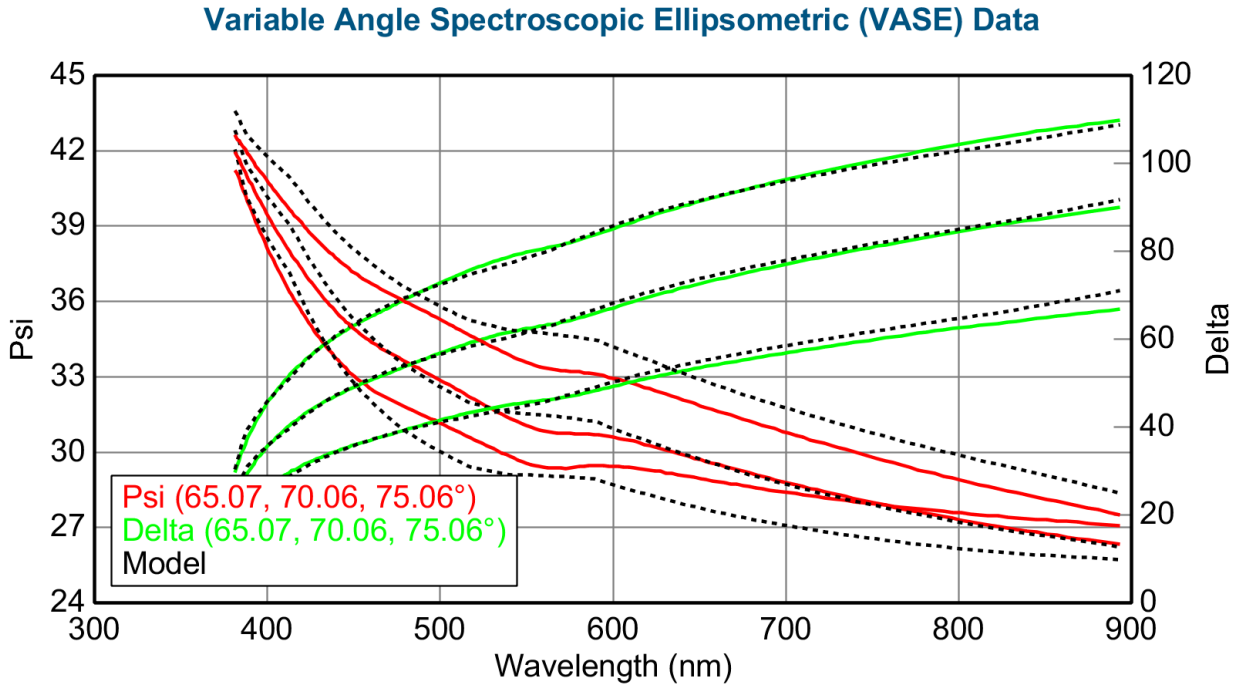

Figure 5.48: Δ and Ψ of fabricated BHMM at measurement spot 2.

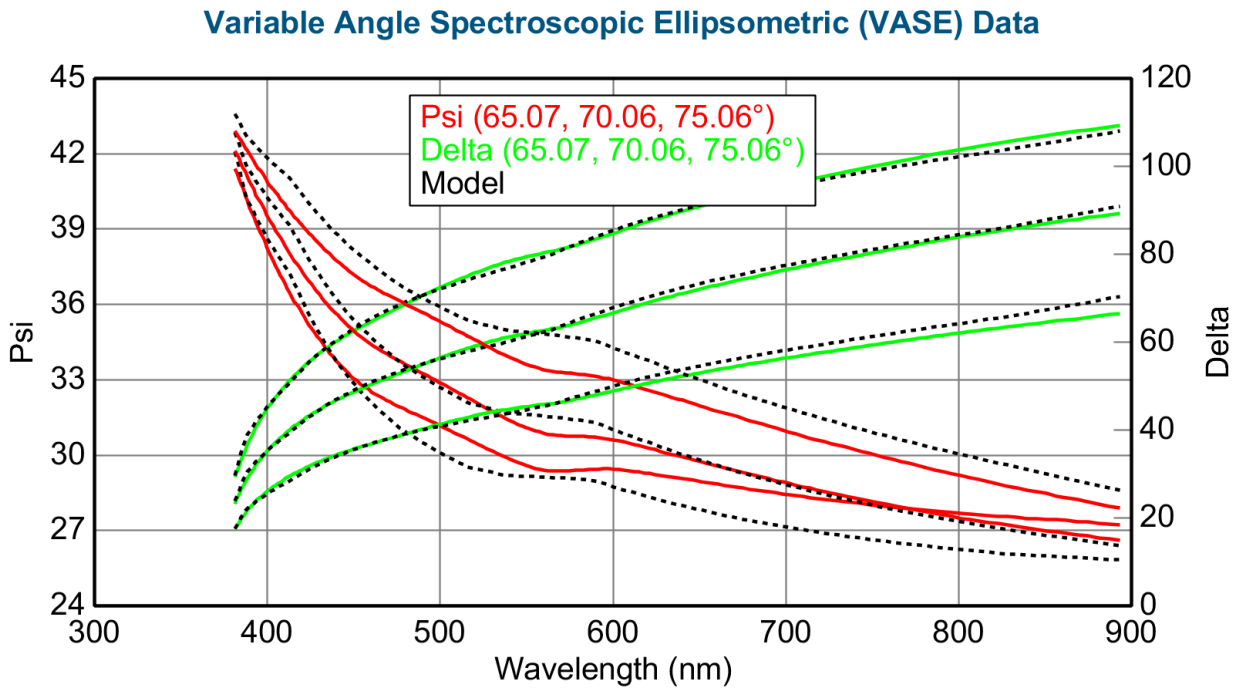

Figure 5.49: Δ and Ψ of fabricated BHMM at measurement spot 3.

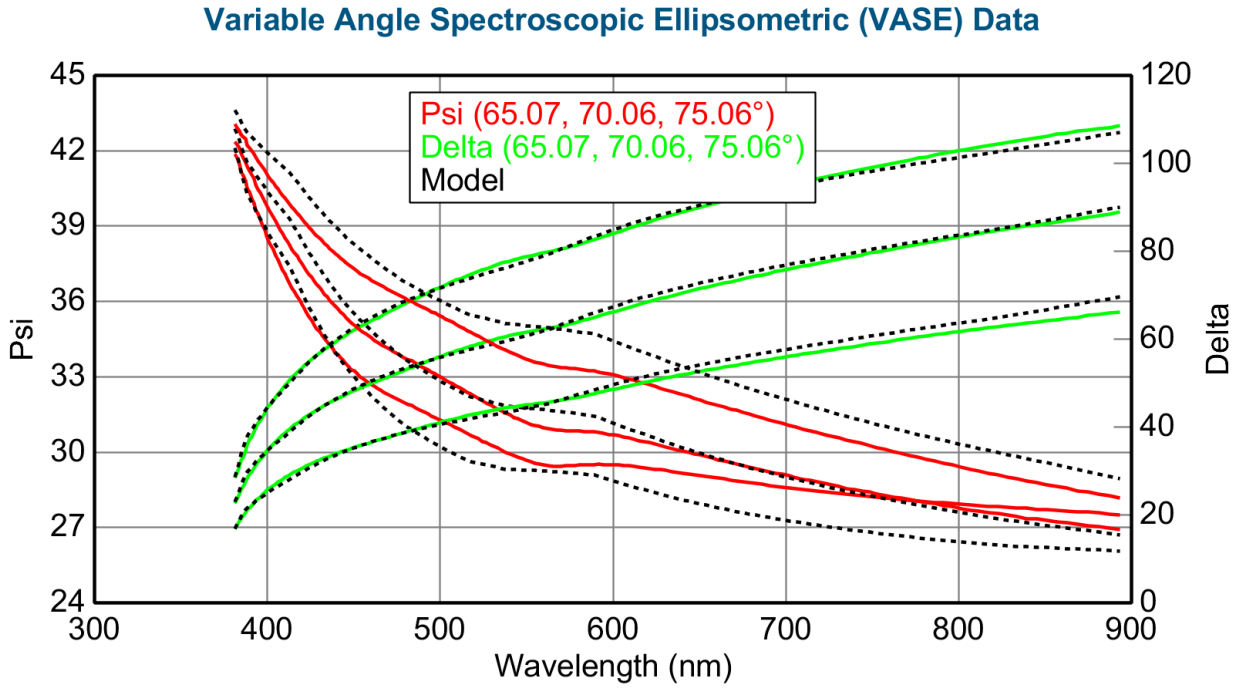

Figure 5.50: Δ and Ψ of fabricated BHMM at measurement spot 4.

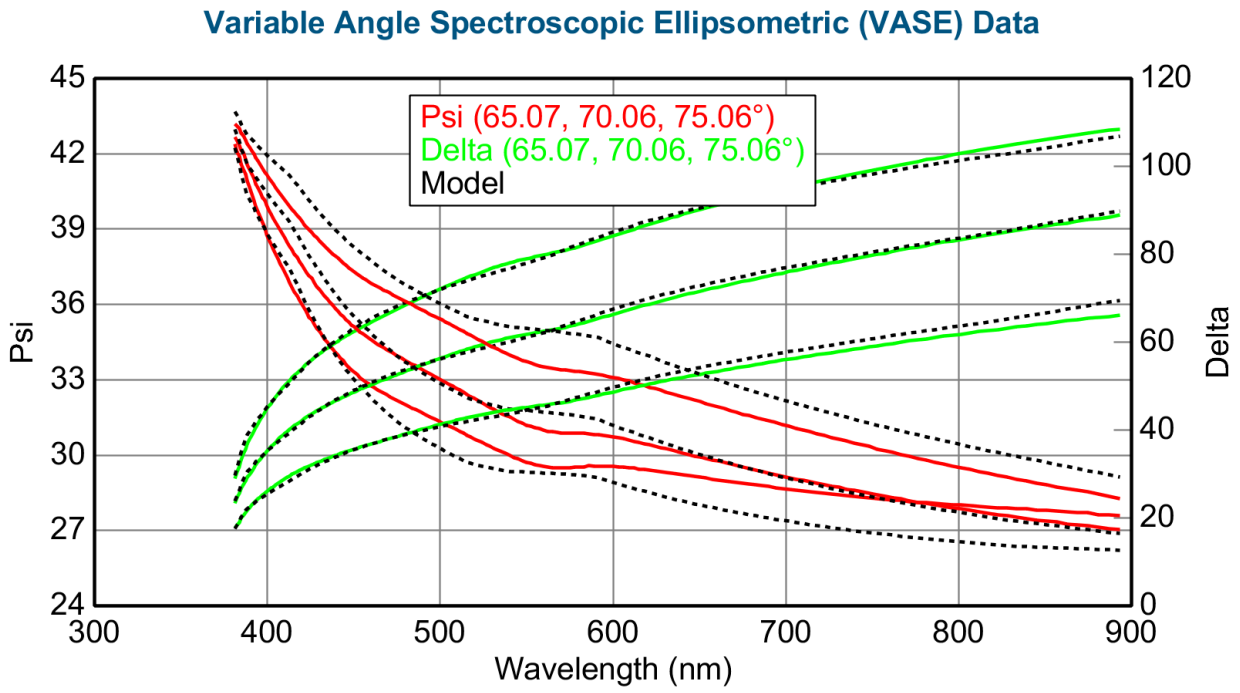

Figure 5.51: Δ and Ψ of fabricated BHMM at measurement spot 5.

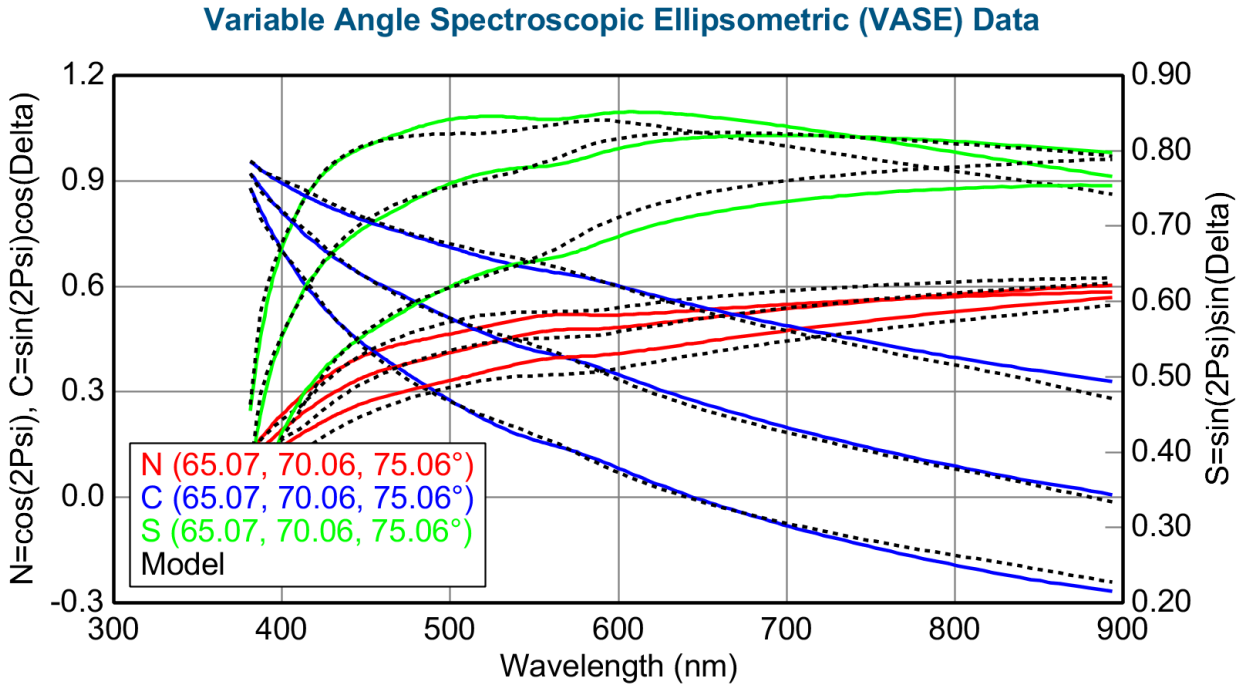

Figure 5.52: *N*, *C*, *S* data of fabricated BHMM at measurement spot 1.

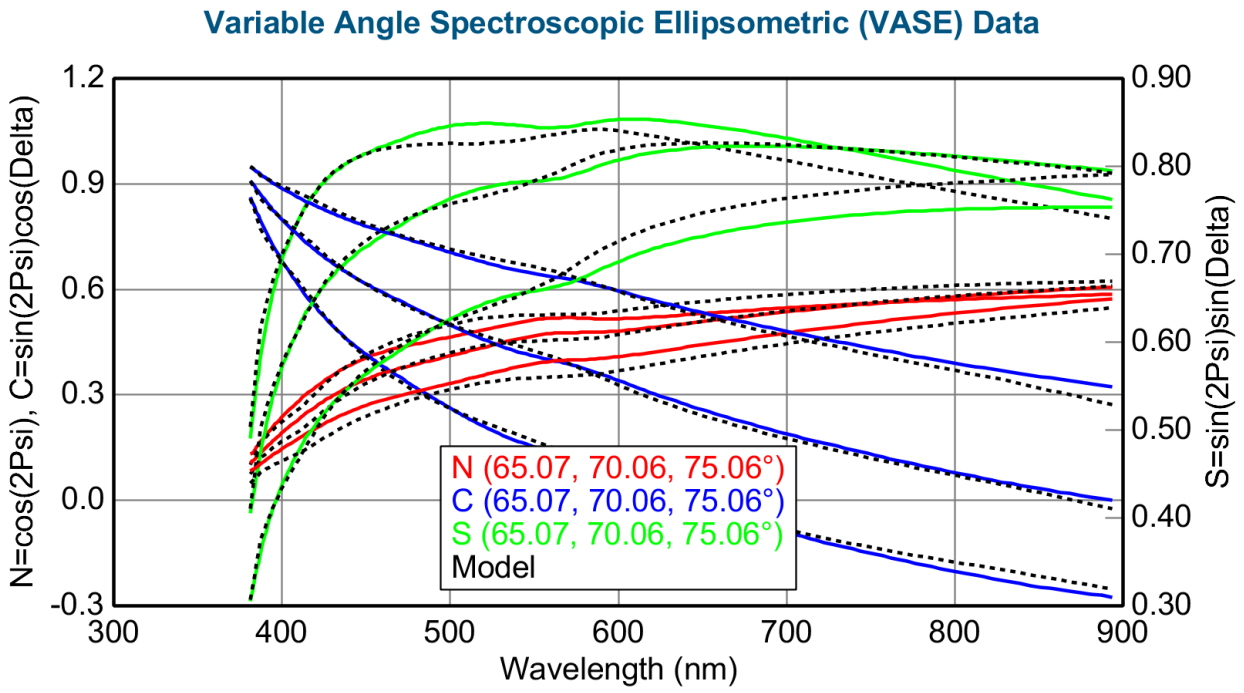

Figure 5.53: *N*, *C*, *S* **data of fabricated BHMM at measurement spot 2.**

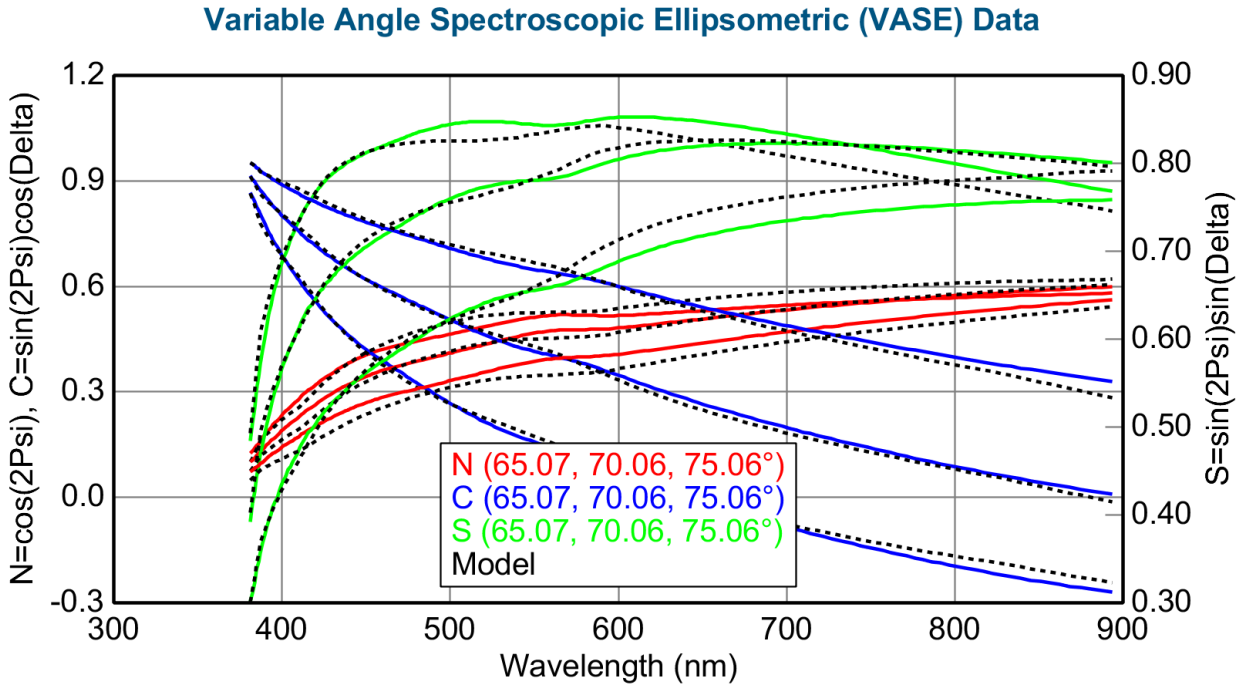

Figure 5.54: *N*, *C*, *S* **data of fabricated BHMM at measurement spot 3.**

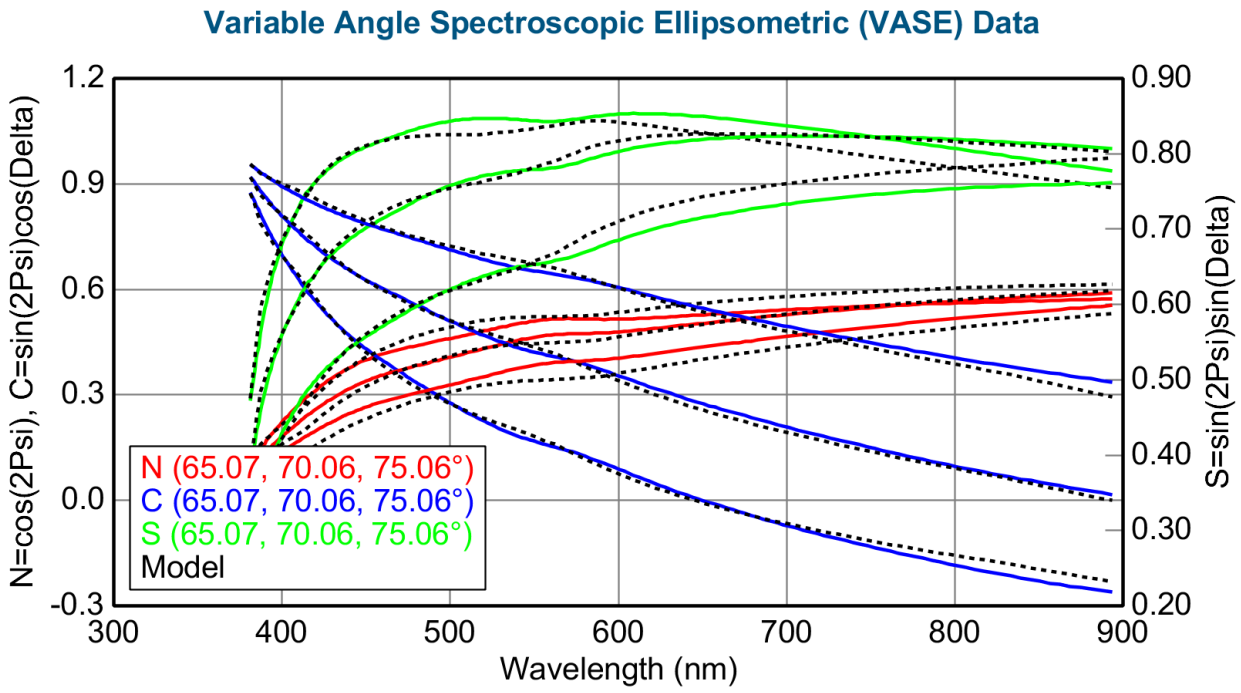

Figure 5.55: *N*, *C*, *S* **data of fabricated BHMM at measurement spot 4.**

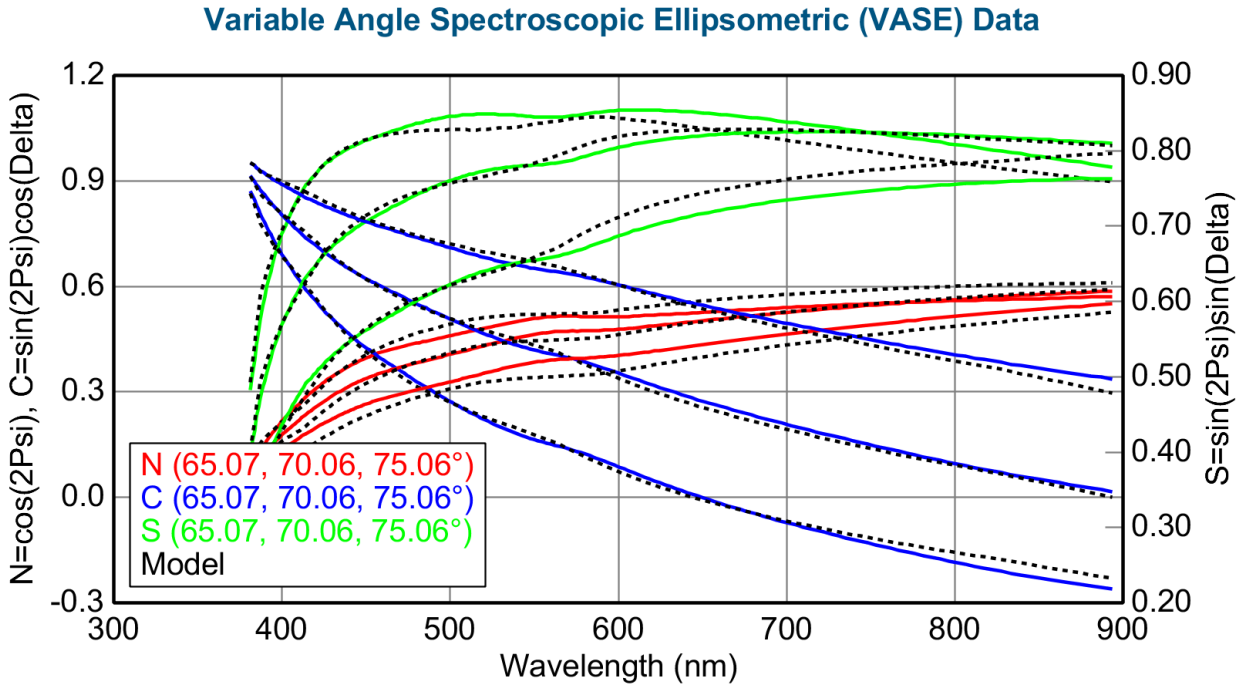

Figure 5.56: *N*, *C*, *S* **data of fabricated BHMM at measurement spot 5.**

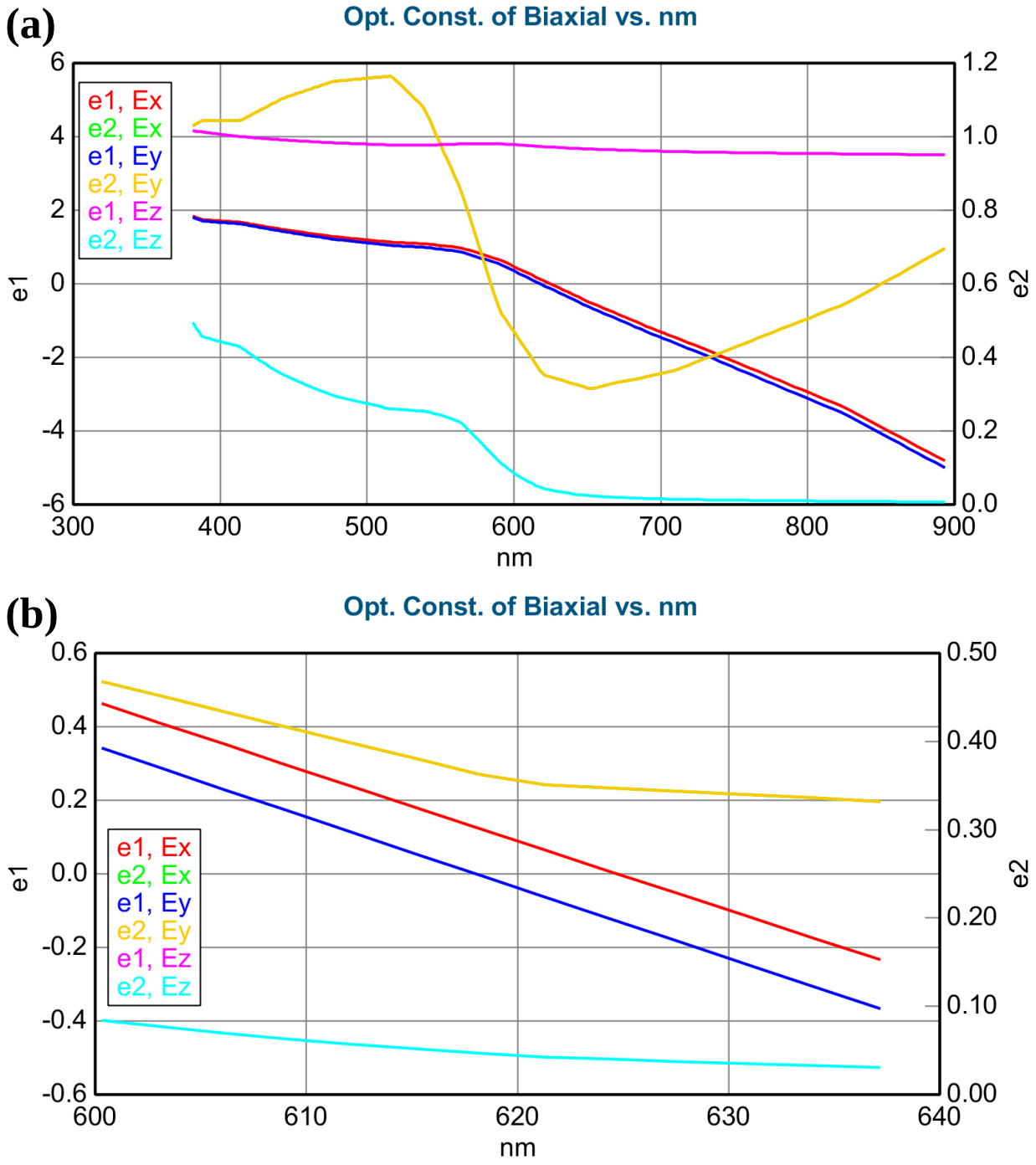

Figure 5.57: (a) Permittivities of fabricated BHMM at measurement spot 1. (b) Zoomed graph of (a) from 600 nm to 640 nm. After 625 nm, the BHMM acts as Type II hyperbolic metamaterial with in-plane permittivity difference of 0.13.

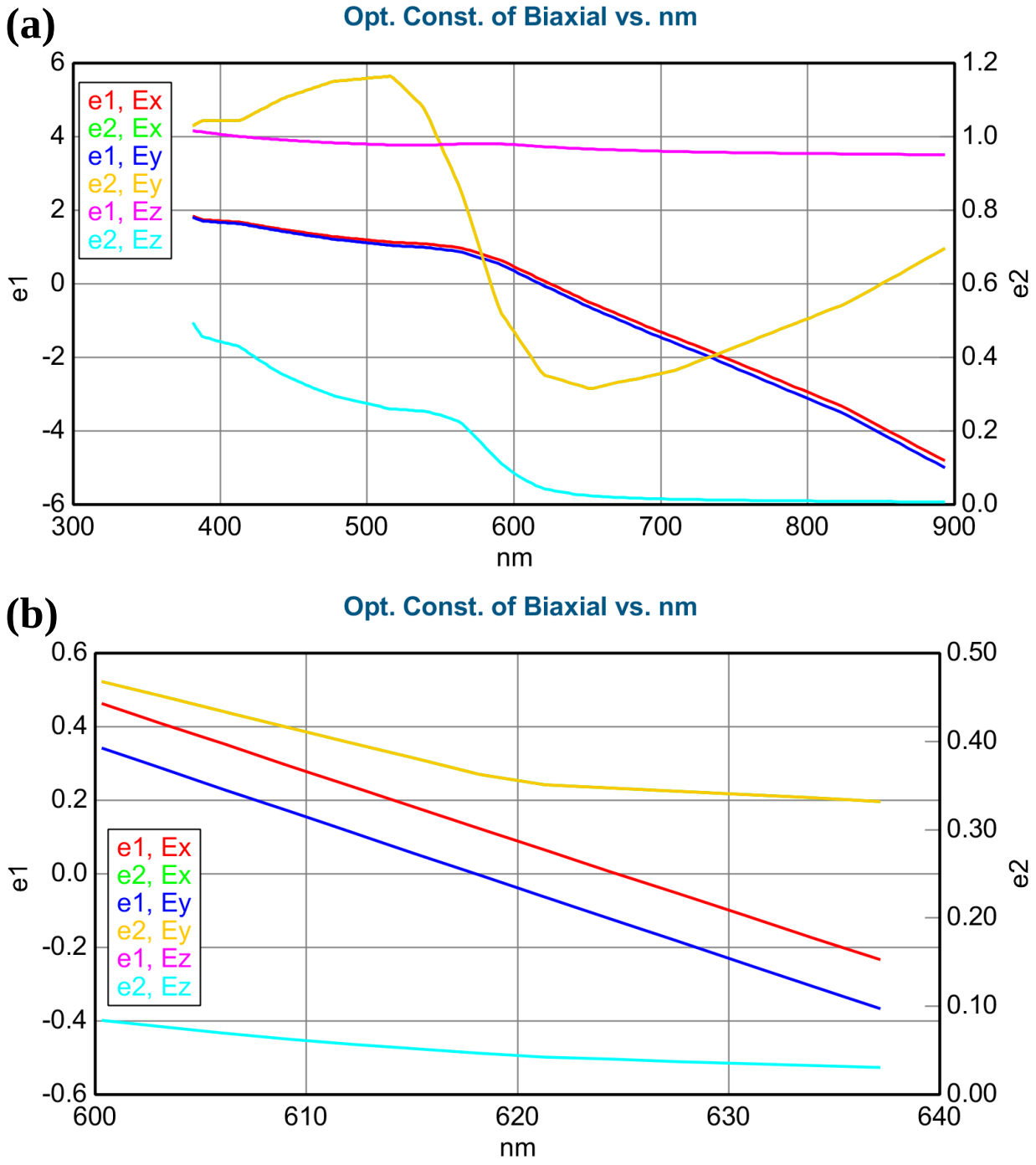

Figure 5.58: (a) Permittivities of fabricated BHMM at measurement spot 2. (b) Zoomed graph of (a) from 600 nm to 640 nm. After 625 nm, the BHMM acts as Type II hyperbolic metamaterial with in-plane permittivity difference of 0.13.

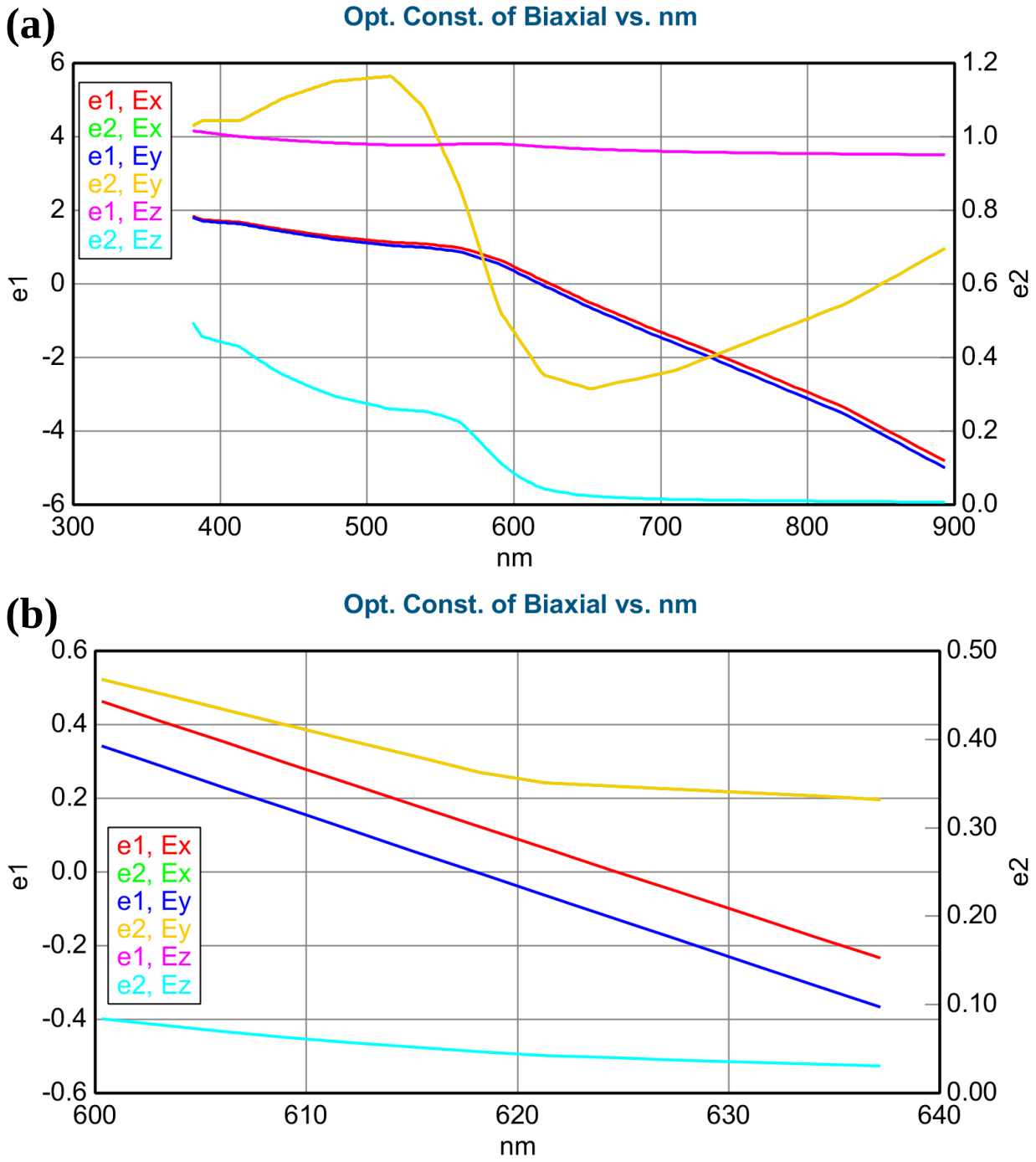

Figure 5.59: (a) Permittivities of fabricated BHMM at measurement spot 3. (b) Zoomed graph of (a) from 600 nm to 640 nm. After 625 nm, the BHMM acts as Type II hyperbolic metamaterial with in-plane permittivity difference of 0.13.

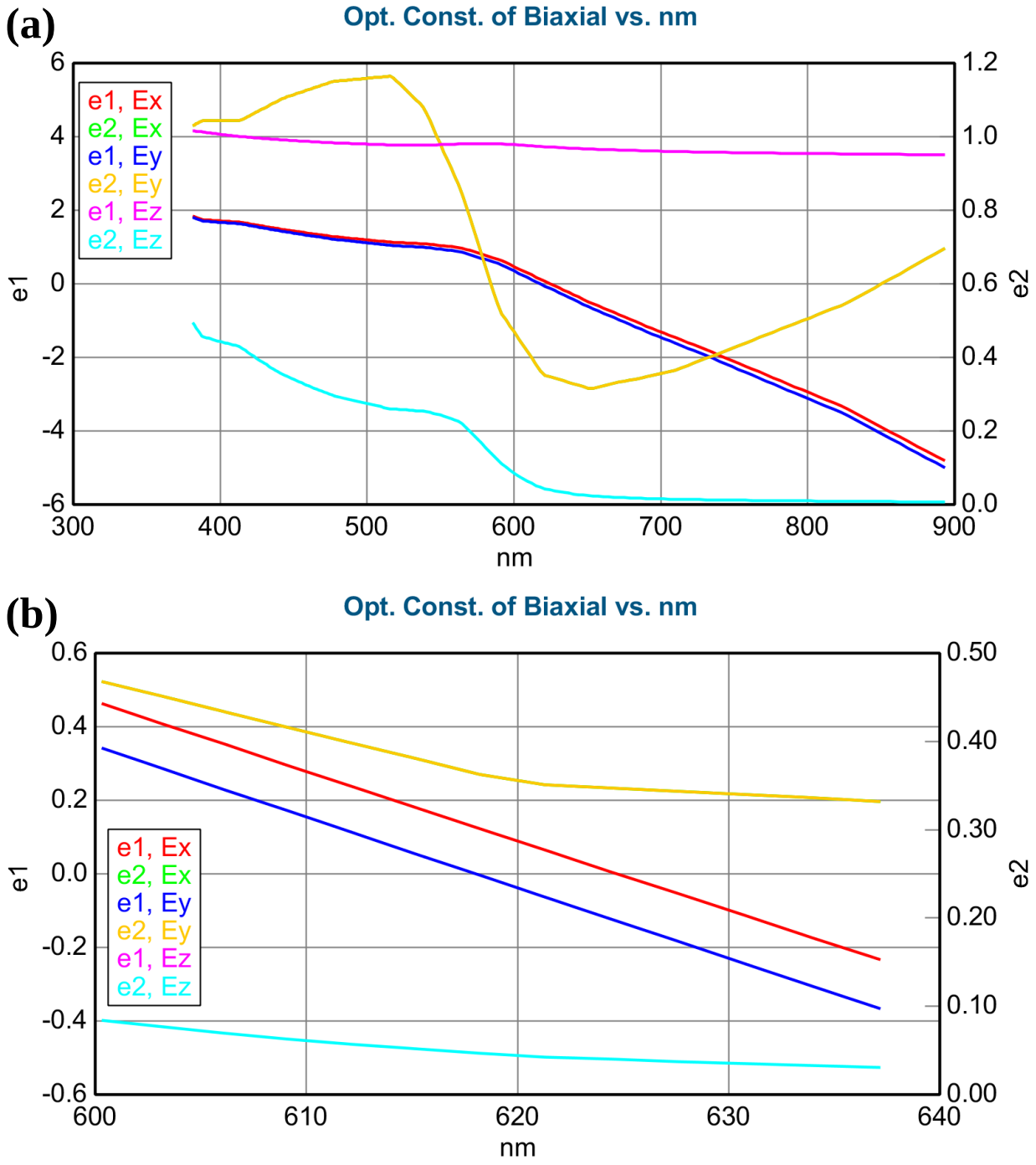

Figure 5.60: (a) Permittivities of fabricated BHMM at measurement spot 4. (b) Zoomed graph of (a) from 600 nm to 640 nm. After 625 nm, the BHMM acts as Type II hyperbolic metamaterial with in-plane permittivity difference of 0.13.

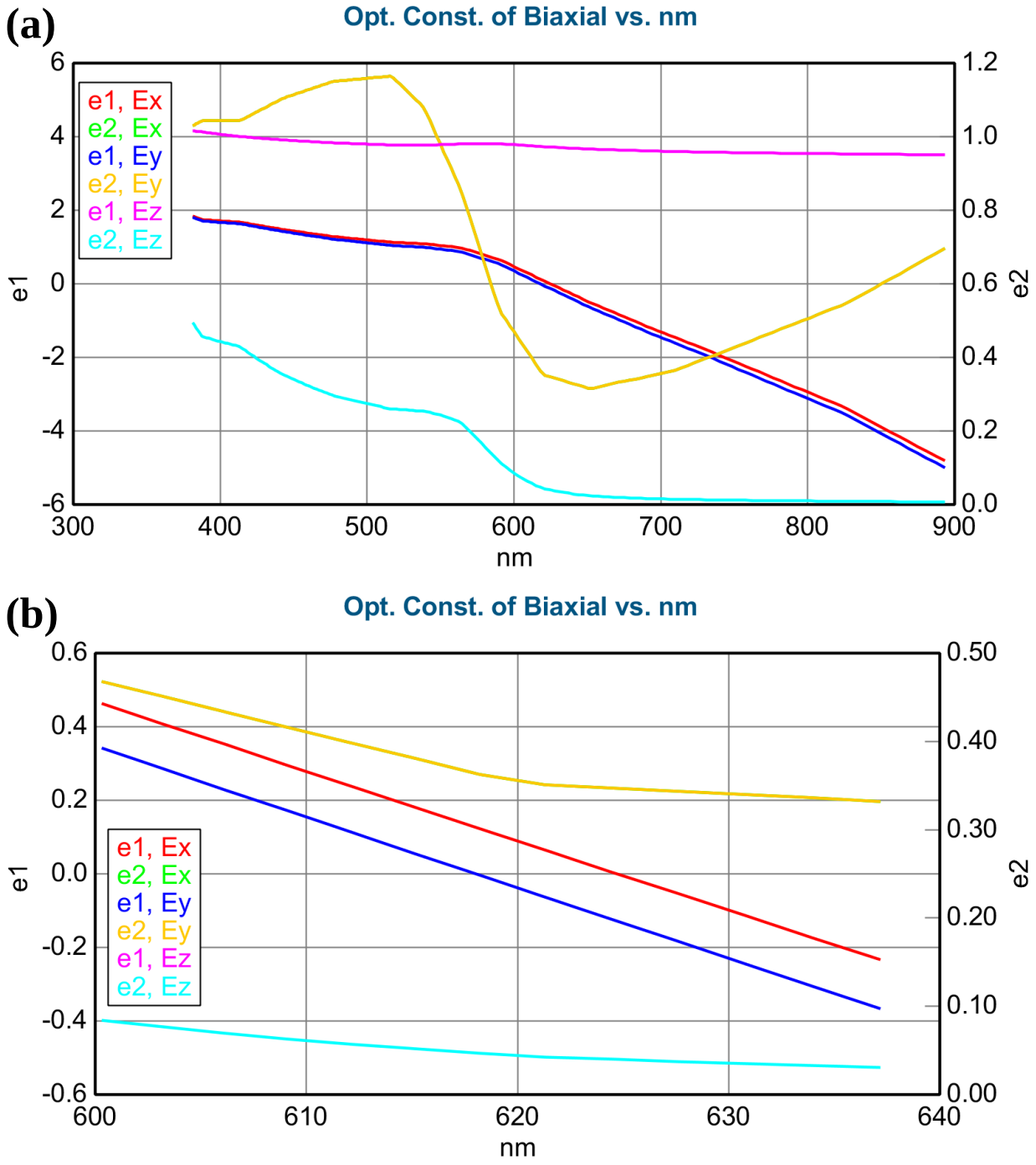

Figure 5.61: (a) Permittivities of fabricated BHMM at measurement spot 5. (b) Zoomed graph of (a) from 600 nm to 640 nm. After 625 nm, the BHMM acts as Type II hyperbolic metamaterial with in-plane permittivity difference of 0.13.

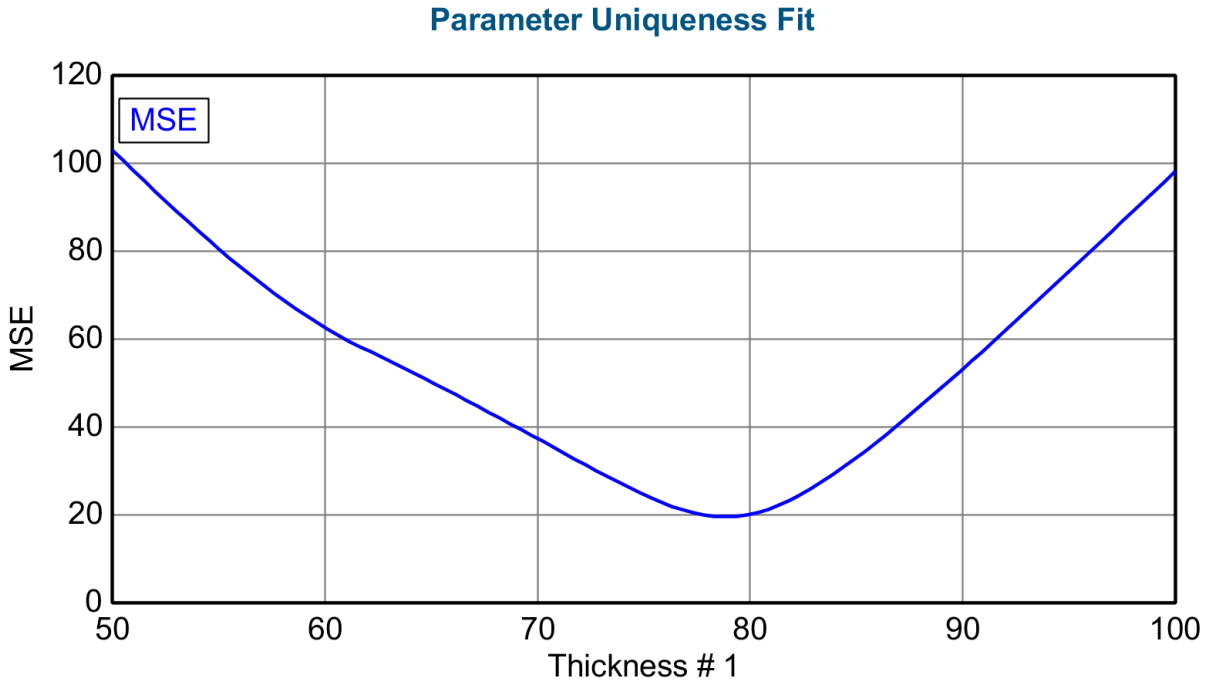

Figure 5.62: Uniqueness fit of fabricated BHMM from 50 to 100 nm at measurement spot 1.

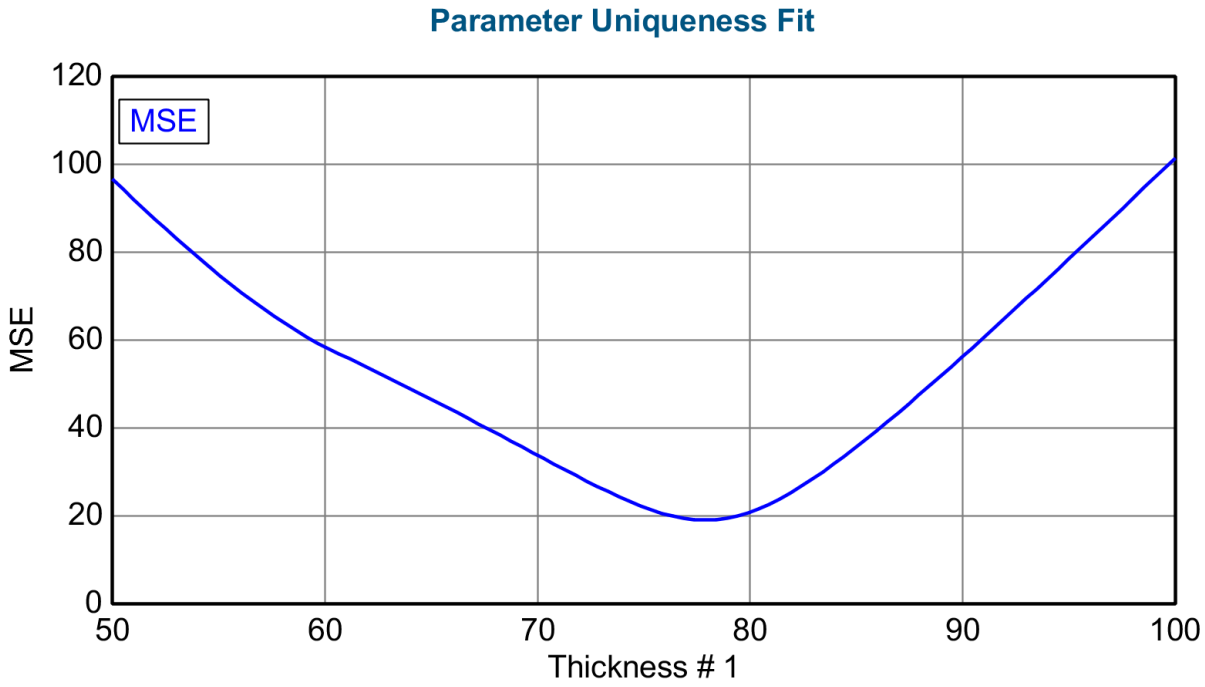

Figure 5.63: Uniqueness fit of fabricated BHMM from 50 to 100 nm at measurement spot 2.

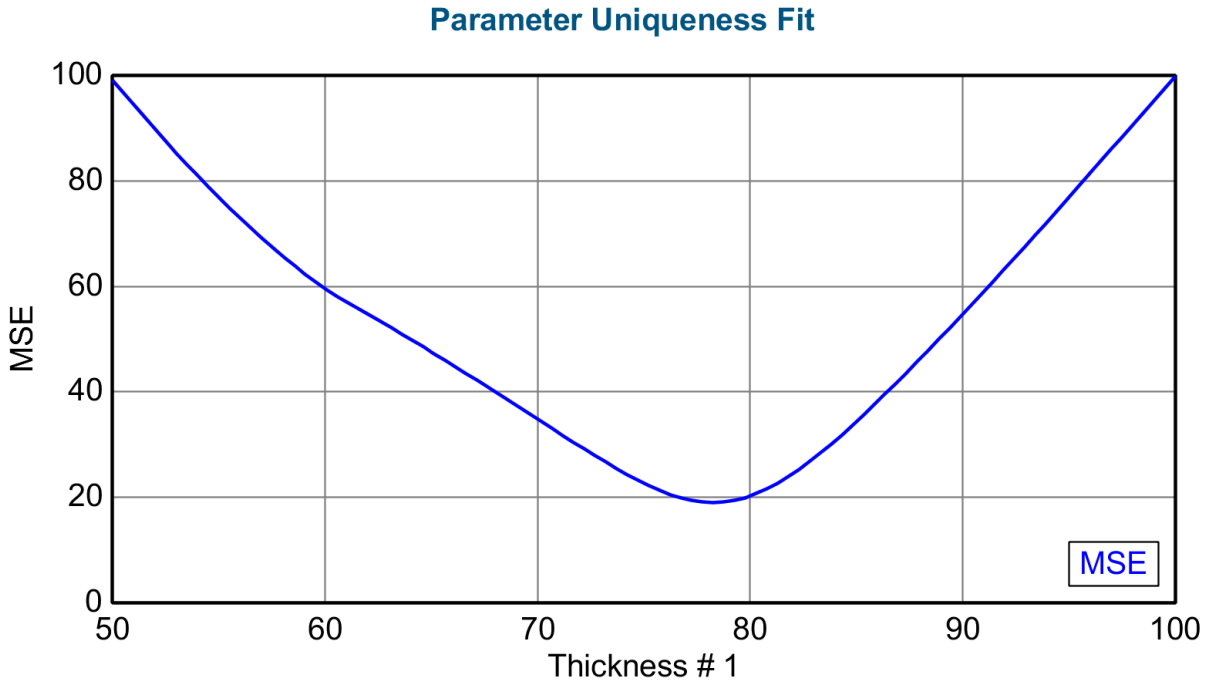

Figure 5.64: Uniqueness fit of fabricated BHMM from 50 to 100 nm at measurement spot 3.

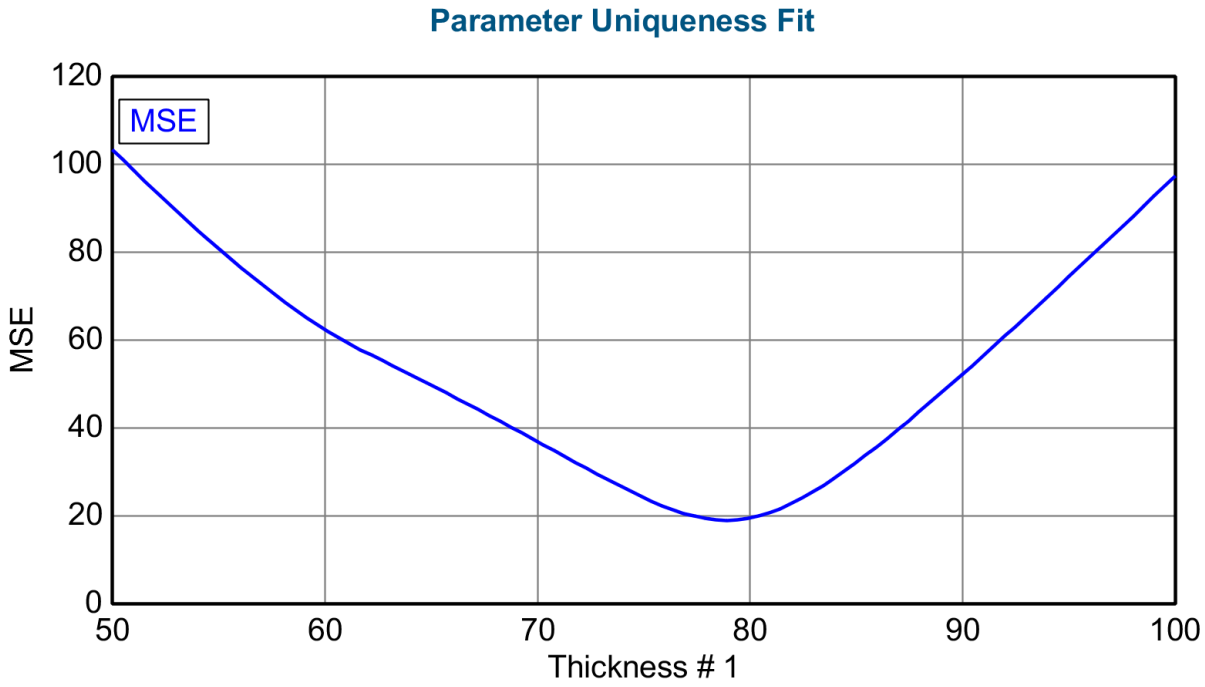

Figure 5.65: Uniqueness fit of fabricated BHMM from 50 to 100 nm at measurement spot 4.

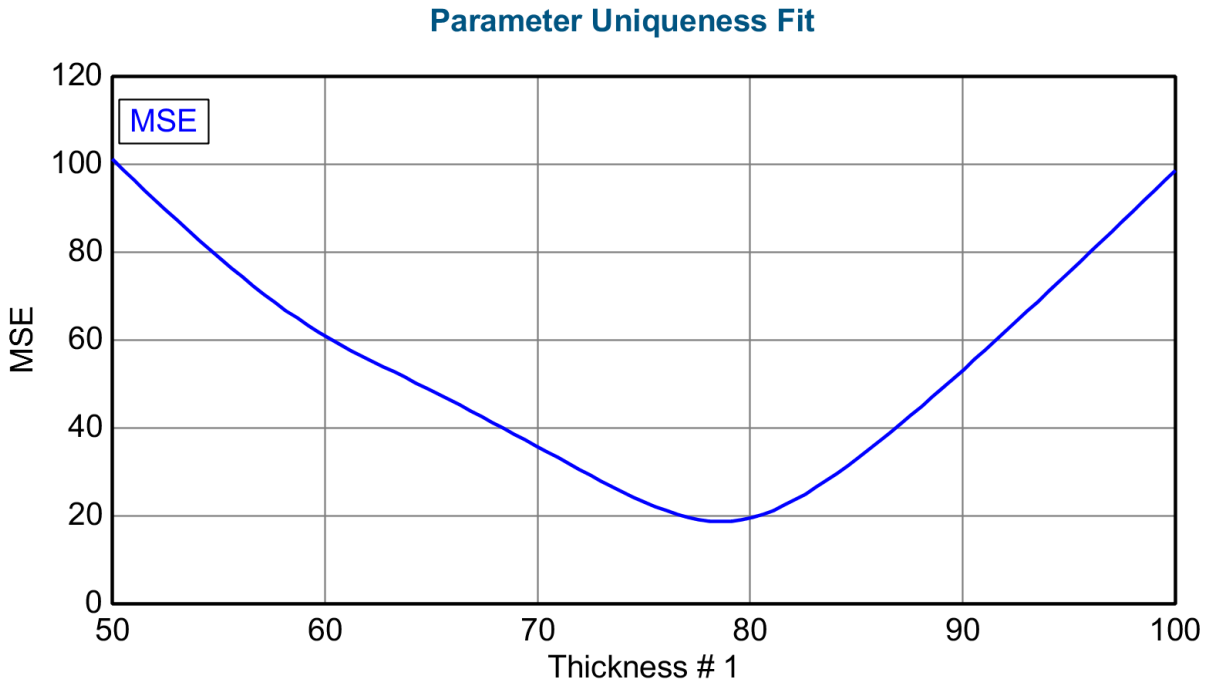

Figure 5.66: Uniqueness fit of fabricated BHMM from 50 to 100 nm at measurement spot 5.

5.2. Profilometer

A profilometer was used to measure the thickness physically from the Si substrate to the height of biaxial HMM (Fig. 5.67). In the fabrication process, the Si wafer was fixed with three clips in order to hold it onto the stage, so the three portions covered with the clips were not deposited with materials. Thus, the profilometer probe tip was placed at these portions and measured the thicknesses. The measurement spot is described in Fig. 5.68. Two profilometer results were obtained as Fig. 5.69. The first measurement shows the sample has thickness of 83.7 $\pm$ 3.6 nm and the second measurement indicates the thickness of 73.3 $\pm$ 2.6 nm. The two values are nearly matched with our target BHMM thickness of 75 nm as well as VASE measured thickness.

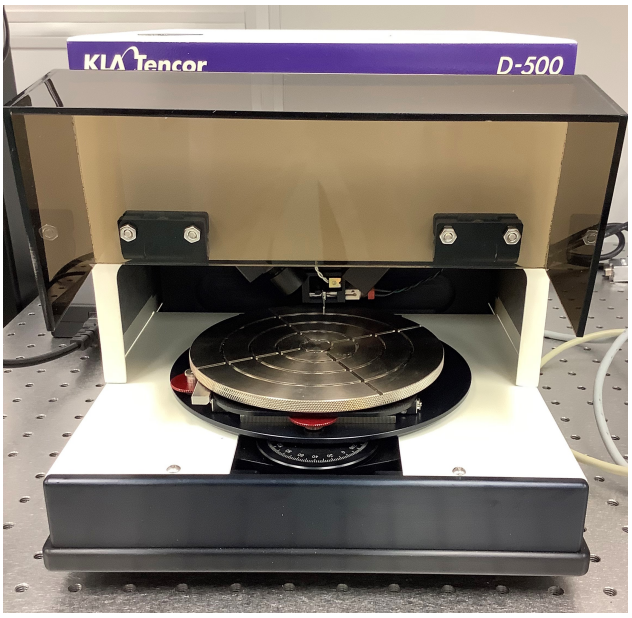

Figure 5.67: D-500 profilometer system (KLA Tencor) for physical measurement of the thickness.

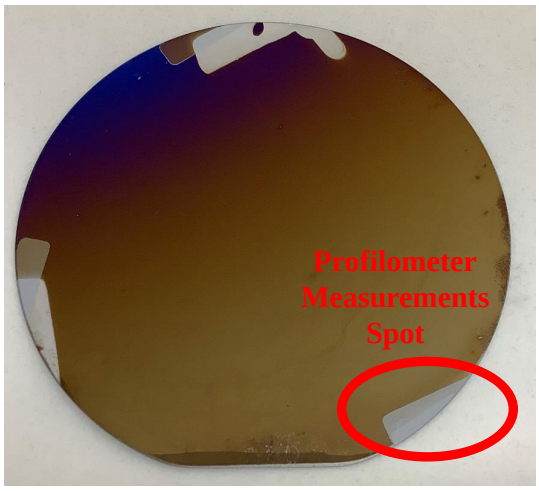

Figure 5.68: Profilometer measurement spot on the fabricated BHMM.

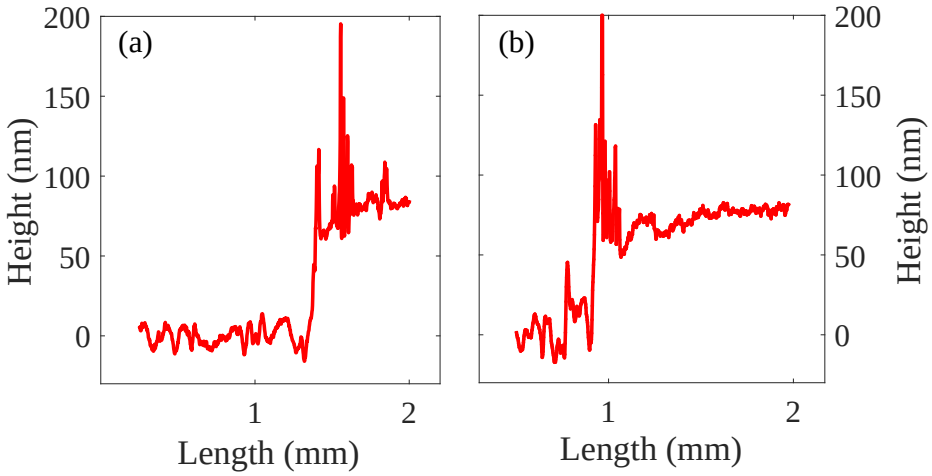

Figure 5.69: The results of the thickness of BHMM through profilometer. (a) 83.7 $\pm$ 3.6 nm for the first measurement and (b) 73.3 $\pm$ 2.6 nm for the second measurement.

6. DISCUSSION OF RESULTS

For the final comparison, the permittivities of the BHMM sample of the EMA calculation and VASE measurements are described in Table 6.1. The profilometer measurements of 83.7 $\pm$ 3.6 nm for the first measurement and 73.3 $\pm$ 2.6 nm for the second measurement (Fig. 5.69) are well matched with VASE thickness measurements of 78.8 $\pm$ 0.2 nm with MSE of 19.58 for spot 1, 77.9 $\pm$ 0.2 nm with MSE of 19.04 for spot 2, 78.3 $\pm$ 0.2 nm with MSE of 18.99 for spot 3, 78.9 $\pm$ 0.2 nm with MSE of 19.01 for spot 4, and 78.6 $\pm$ 0.2 nm with MSE of 18.72 for spot 5 (Table 5.8).

It is observed that the experimental results obtained for the fabricated BHMM is in good agreement with the predictions of the effective medium approximation (Fig. 3.7). The five VASE measurements indicate that average MSE value of 19.1 $\pm$ 0.2 which is acceptable value for biaxial sample, average thickness of 78.5 $\pm$ 0.4 nm which is well matched with target thickness of 75 nm, average ϕ of -23.3° $\pm$ 0.5° and average θ of -32.4° $\pm$ 0.1° which are acceptable as described in Sec. 5.1.4. Thus, the fitted model resulted in an effective thickness of 63.5 nm for OAD TiO_2 ($p = 0.236$) in the fabricated BHMM. Therefore, the fabricated BHMM is remarkably similar to the designed BHMM with only p difference of 0.036. In addition, Epsilon-Near-Zero (ENZ) is placed at around 625 nm and the difference between ε_x and ε_y values at 625 nm is 0.13 $\pm$ 0.001, which enables biaxial hyperbolic dispersion. Dual ENZ regions which are separated by 6.7 nm was observed as well. Above the 625 nm, the Type II biaxial hyperbolic dispersion is obtained as its real in-plane permittivities (x- and y-directions) are negative and out-of-plane permittivity (z-direction) is positive. The fitted Euler angles might occur from tilted biaxial ellipsoid of OAD TiO_2 nanocolumnar structures Fig. 2.1. More specifically, fitted ϕ might be related to the sample

misalignment on the VASE measurement stage, and fitted θ of might be related to non-uniform thickness of OAD TiO_2 layer throughout the wafer because of the 70 degree stage, or surface roughness of nanocolumnar structures, or the 51° column axis angle of OAD TiO_2 layer. The five measurements of the BHMM sample proved to have great repeatability and reproducibility (Table 6.1). Therefore, the fabrication of a practical BHMM has been successfully demonstrated.

Table 6.1: Comparison of EMA calculation, VASE measurements, and profilometer measurements.

EMA Calculation	VASE Measurements
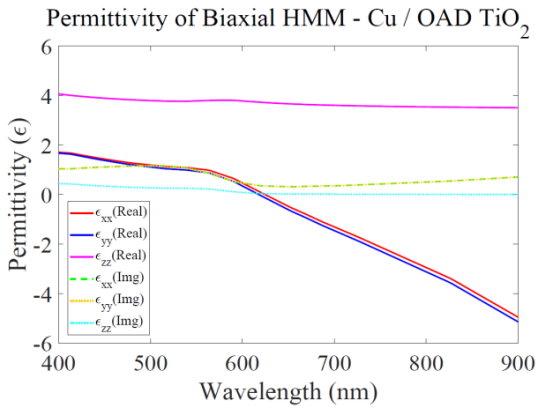	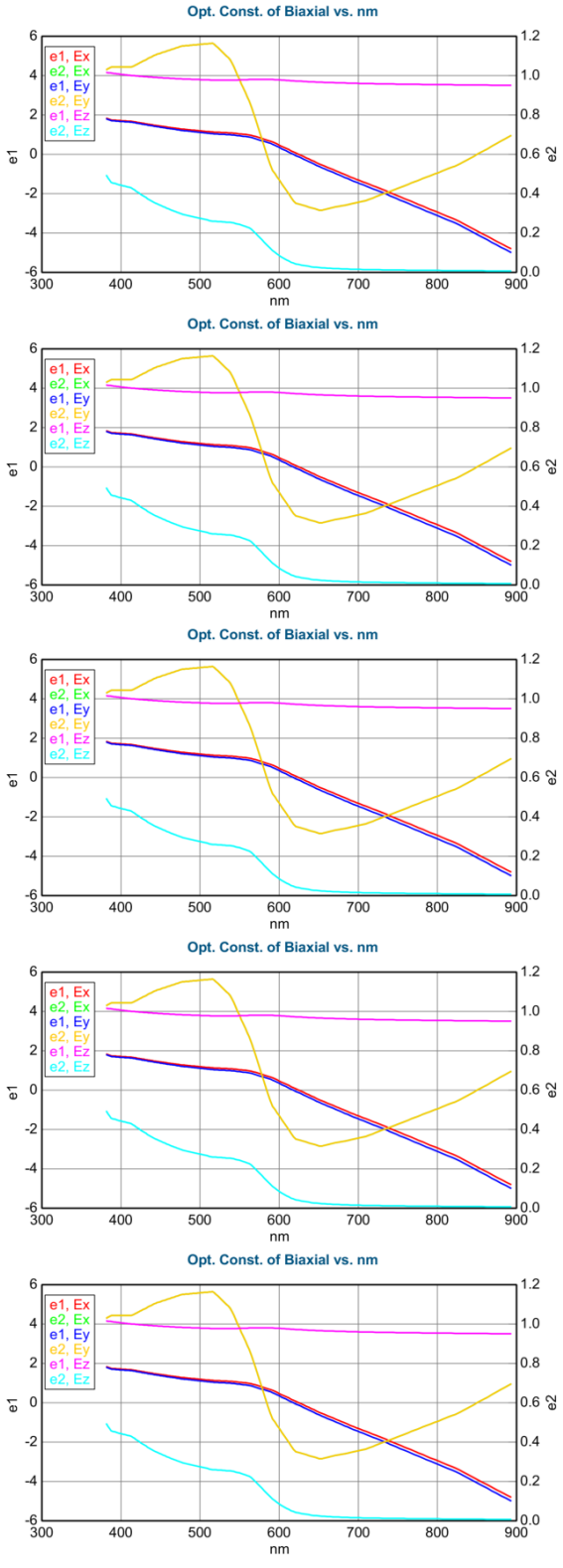
Profilometer Mesurements	
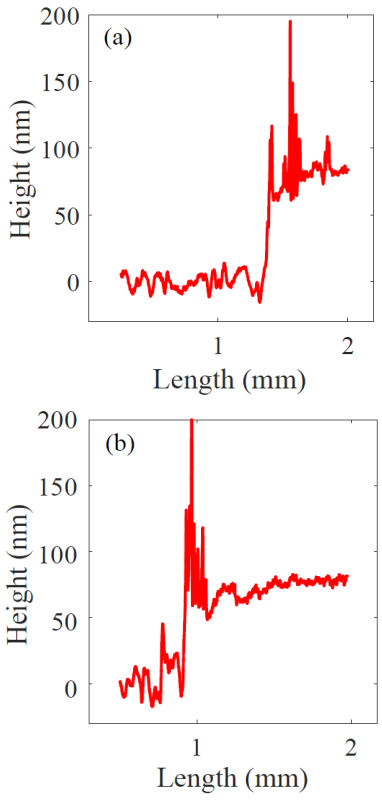	

7. CONCLUSIONS

In conclusion, the researcher have successfully fabricated a biaxial hyperbolic metamaterial (BHMM) using oblique deposition of TiO_2 on Cu at subwavelength scale. By using 80% (60 nm) of OAD TiO_2 in a period (75 nm), a noticeable in-plane permittivity difference of 0.13 $\pm$ 0.001 was obtained near 632.8 nm with dual epsilon-near-zero (ENZ) regions which are separated by 6.7 nm. The fabricated BHMM acts as Type II BHMM after 625 nm. To the best of our knowledge, this is the first time a biaxial hyperbolic metamaterial has been fabricated with this approach. The fabricated device was characterized using variable angle spectroscopic ellipsometry (VASE) for extraction of the permittivity tensor. The results of experimental characterization via VASE is significantly close to the predictions by effective medium approximation with average MSE value of 19.1 $\pm$ 0.16. The thickness measurements by VASE and profilometer are all well matched with target thickness of 75 nm. For future works, VASE measurements with rotation mode would yield better results for Euler angle characterization of the biaxial materials. In addition, increasing the number of unit cell have an effect on high-*k* modes, which is bulk polaritonic modes having large momentum to light-matter coupling [50]. Thus, BHMM with large number of unit cell should be investigated for the high-*k* modes. Our approach in achieving BHMMs provides an advantageous path for rapid fabrication of such devices and implementation of their exotic properties in a variety of applications in nanophotonics such as vortex beam generation carrying an orbital angular momentum [20] and for the spin-controllable excitation of surface waves [21]. As research on BHMMs is in an early stage, hopefully this research provides inspirations to future research on BHMM.

LIST OF REFERENCES

[1] Lorenzo Ferrari et al. “Hyperbolic metamaterials and their applications”. In: *Progress in Quantum Electronics* 40 (2015), pp. 1–40.

[2] Yongmin Liu and Xiang Zhang. “Metamaterials: a new frontier of science and technology”. In: *Chemical Society Reviews* 40.5 (2011), pp. 2494–2507.

[3] David R Smith et al. “Partial focusing of radiation by a slab of indefinite media”. In: *Applied physics letters* 84.13 (2004), pp. 2244–2246.

[4] BDF Casse et al. “Super-resolution imaging using a three-dimensional metamaterials nanolens”. In: *Applied Physics Letters* 96.2 (2010), p. 023114.

[5] Rui Zang et al. “Broadband hyperbolic metamaterial covering the whole visible-light region”. In: *Optics letters* 44.12 (2019), pp. 2970–2973.

[6] Wei Wang, Xiaodong Yang, and Jie Gao. “Scaling law of Purcell factor in hyperbolic metamaterial cavities with dipole excitation”. In: *Optics letters* 44.3 (2019), pp. 471–474.

[7] Dylan Lu et al. “Enhancing spontaneous emission rates of molecules using nanopatterned multilayer hyperbolic metamaterials”. In: *Nature nanotechnology* 9.1 (2014), p. 48.

[8] Osamu Takayama et al. “Photonic spin Hall effect in hyperbolic metamaterials at visible wavelengths”. In: *Optics letters* 43.19 (2018), pp. 4602–4605.

[9] Patrick Sohr, Chi Ian Ip, and Stephanie Law. “Far-field thermal emission from a semiconductor hyperbolic metamaterial”. In: *Optics letters* 44.5 (2019), pp. 1138–1141.

[10] OA Makarova et al. “Patterned multilayer metamaterial for fast and efficient photon collection from dipolar emitters”. In: *Optics letters* 42.19 (2017), pp. 3968–3971.

[11] Igor I Smolyaninov. “Giant Unruh effect in hyperbolic metamaterial waveguides”. In: *Optics letters* 44.9 (2019), pp. 2224–2227.

[12] IA Kolmychek et al. “Magneto-optical effects in hyperbolic metamaterials”. In: *Optics letters* 43.16 (2018), pp. 3917–3920.

[13] Alexander K Popov and Sergey A Myslivets. “Generation, amplification, frequency conversion, and reversal of propagation of THz photons in nonlinear hyperbolic metamaterial”. In: *Optics letters* 42.20 (2017), pp. 4151–4154.

[14] Akash Kannegulla and Li-Jing Cheng. “Subwavelength focusing of terahertz waves in silicon hyperbolic metamaterials”. In: *Optics letters* 41.15 (2016), pp. 3539–3542.

[15] Zubin Jacob, Leonid V Alekseyev, and Evgenii Narimanov. “Optical hyperlens: far-field imaging beyond the diffraction limit”. In: *Optics express* 14.18 (2006), pp. 8247–8256.

[16] Zhaowei Liu et al. “Far-field optical hyperlens magnifying sub-diffraction-limited objects”. In: *science* 315.5819 (2007), pp. 1686–1686.

[17] Harish NS Krishnamoorthy et al. “Topological transitions in metamaterials”. In: *Science* 336.6078 (2012), pp. 205–209.

[18] Kandammathe Valiyaveedu Sreekanth, Antonio De Luca, and Giuseppe Strangi. “Experimental demonstration of surface and bulk plasmon polaritons in hypergratings”. In: *Scientific reports* 3 (2013), p. 3291.

[19] James Dilts et al. “Low-MSE extraction of permittivity in optical hyperbolic metamaterials”. In: *Optics letters* 44.17 (2019), pp. 4303–4306.

[20] Jingbo Sun, Jinwei Zeng, and Natalia M Litchinitser. “Twisting light with hyperbolic metamaterials”. In: *Optics express* 21.12 (2013), pp. 14975–14981.

[21] Wen-Long Gao et al. “Chiral surface waves supported by biaxial hyperbolic metamaterials”. In: *Light: Science & Applications* 4.9 (2015), e328.

[22] Xianglian Song et al. “Biaxial hyperbolic metamaterials using anisotropic few-layer black phosphorus”. In: *Optics express* 26.5 (2018), pp. 5469–5477.

[23] Sumei Wang et al. “Structural and optical properties of nanostructured TiO_2 thin films fabricated by glancing angle deposition”. In: *Journal of Alloys and Compounds* 431.1-2 (2007), pp. 287–291.

[24] Ehsan Ordouie, Hossein Alisafaee, and Azad Siahmakoun. “Ultracompact polarizing beam splitter based on single-material birefringent photonic crystal”. In: *Optics letters* 43.17 (2018), pp. 4288–4291.

[25] Cheng Zhang et al. “Robust extraction of hyperbolic metamaterial permittivity using total internal reflection ellipsometry”. In: *ACS photonics* 5.6 (2018), pp. 2234–2242.

[26] R Secondo et al. “Reliable modeling of ultrathin alternative plasmonic materials using spectroscopic ellipsometry”. In: *Optical Materials Express* 9.2 (2019), pp. 760–770.

[27] James N Hilfiker et al. “Survey of methods to characterize thin absorbing films with spectroscopic ellipsometry”. In: *Thin Solid Films* 516.22 (2008), pp. 7979–7989.

[28] Bahaa EA Saleh and Malvin Carl Teich. *Fundamentals of photonics*. john Wiley & sons, 2019.

[29] MS Dresselhaus. “Solid state physics part ii optical properties of solids”. In: *Lecture Notes (Massachusetts Institute of Technology, Cambridge, MA)* 17 (2001).

[30] Matthew M Hawkeye, Michael T Taschuk, and Michael J Brett. *Glancing angle deposition of thin films: engineering the nanoscale*. John Wiley & Sons, 2014.

[31] JM Nieuwenhuizen and HBi Haanstra. “Microfractography of thin films”. In: *Philips Tech Rev* 27.3 (1966), pp. 87–91.

[32] RN Tait, T Smy, and MJ Brett. “Modelling and characterization of columnar growth in evaporated films”. In: *Thin Solid Films* 226.2 (1993), pp. 196–201.

[33] Angel Barranco et al. “Perspectives on oblique angle deposition of thin films: From fundamentals to devices”. In: *Progress in Materials Science* 76 (2016), pp. 59–153.

[34] Wenshan Cai and Vladimir M Shalaev. *Optical metamaterials*. Vol. 10. 6011. Springer, 2010.

[35] James Dilts. “Design, Fabrication, and Characterization of Multilayer Hyperbolic Metamaterials”. In: *Rose-Hulman Institute of Technology Graduate Theses - Physics and Optical Engineering. 5.* (2019).

[36] Peter Uhd Jepsen et al. “Metal-insulator phase transition in a VO_2 thin film observed with terahertz spectroscopy”. In: *Physical Review B* 74.20 (2006), p. 205103.

[37] HS Choi et al. “Mid-infrared properties of a VO_2 film near the metal-insulator transition”. In: *Physical Review B* 54.7 (1996), p. 4621.

[38] Maria Losurdo and Kurt Hingerl. *Ellipsometry at the Nanoscale*. Springer, 2013.

[39] B Wood, JB Pendry, and DP Tsai. “Directed subwavelength imaging using a layered metal-dielectric system”. In: *Physical Review B* 74.11 (2006), p. 115116.

[40] Alexander Poddubny et al. “Hyperbolic metamaterials”. In: *Nature photonics* 7.12 (2013), p. 948.

[41] J. A. Woollam Co. *CompleteEASE Data Analysis Manual Version 4.63*. J. A. Woollam Co., Inc, 2011.

[42] Andrew Martin. *”Session 3A, Non-idealities”*. Available at: `https://www.seas.upenn.edu/~nanosop/documents/Session3A_UPenn_WVASE_Feb_2014.pdf` (Accessed: 10 April 2020). J. A. Woollam Co., Inc. (2014).

[43] Hiroyuki Fujiwara. *Spectroscopic ellipsometry: principles and applications*. John Wiley & Sons, 2007.

[44] GE Jellison Jr. “The calculation of thin film parameters from spectroscopic ellipsometry data”. In: *Thin Solid Films* 290 (1996), pp. 40–45.

[45] Edward D Palik. *Handbook of optical constants of solids*. Vol. 1. Academic press, 1985.

[46] N Bundaleski et al. “Adsorption dynamics of water on the surface of TiO_2 (110)”. In: *Journal of Physics: Conference Series*. Vol. 257. 1. IOP Publishing. 2010, p. 012008.

[47] Stefan Wendt et al. “Oxygen vacancies on TiO_2 (110) and their interaction with H2O and O2: A combined high-resolution STM and DFT study”. In: *Surface Science* 598.1-3 (2005), pp. 226–245.

[48] *”α-SE Variable Angle Spectroscopic Ellipsometry (VASE)”*. Available at: `https://www.jawoollam.com/products/alpha-se-ellipsometer` (Accessed: 13 April 2020). J. A. Woollam Co., Inc.

[49] Junbo Gong et al. “Thickness dispersion of surface plasmon of Ag nano-thin films: Determination by ellipsometry iterated with transmittance method”. In: *Scientific reports* 5.1 (2015), pp. 1–5.

[50] Yu Guo et al. “Applications of hyperbolic metamaterial substrates”. In: *Advances in Opto-Electronics* 2012 (2012).

APPENDICES

APPENDIX A - MATLAB CODES

A.1. Calculation for Asymmetric Hyperbolic Dispersion Relations of Biaxial Hyperbolic Metamaterials

```
%% MATLAB code for calculation of asymmetric hyperbolic dispersion
   relations of biaxial hyperbolic metamaterials

clear all; clc; close all;

%% a. Type 1 - kx=0 TE                              exx=0.4 eyy=0.2 ezz=-0.5
z1TE1 = @(y) sqrt(0.4-y.^2); % function handle to anonymous function
figure(1)
subplot(2,3,1);
fsurf(z1TE1,'EdgeColor','r','LineWidth',3)

hold on

z1TE2 = @(y) -sqrt(0.4-y.^2);
fsurf(z1TE2,'EdgeColor','r','LineWidth',3)

view([0 1 0])
hold on
%% a. Type 1 - kx=0 TM                              exx=0.4 eyy=0.2 ezz=-0.5
z1TM1 = @(y) sqrt(0.2+0.4*y.^2); % function handle to anonymous function
fsurf(z1TM1,'EdgeColor','b','LineWidth',3)

```

```
22 hold on
23
24 z1TM2 = @(y) -sqrt(0.2+0.4*y.^2);
25 fsurf(z1TM2,'EdgeColor','b','LineWidth',3)
26
27 view([0 1 0])
28
29 xlim([-2 2])
30 zlim([-2 2])
31
32 %% b. Type 1 - ky=0 TE                              exx=0.4 eyy=0.2 ezz=-0.5
33 z2TE1 = @(x) sqrt(0.2-x.^2); % function handle to anonymous function
34 figure(1)
35 subplot(2,3,2);
36 fsurf(z2TE1,'EdgeColor','r','LineWidth',3)
37
38 hold on
39
40 z2TE2 = @(x) -sqrt(0.2-x.^2);
41 fsurf(z2TE2,'EdgeColor','r','LineWidth',3)
42
43 view([0 1 0])
44 hold on
45 %% b. Type 1 - ky=0 TM                              exx=0.4 eyy=0.2 ezz=-0.5
46 z2TM1 = @(x) sqrt(0.4+0.8*x.^2); % function handle to anonymous function
47 fsurf(z2TM1,'EdgeColor','b','LineWidth',3)
48
49 hold on
```

```
50
51 z2TM2 = @(x) -sqrt(0.4+0.8*x.^2);
52 fsurf(z2TM2,'EdgeColor','b','LineWidth',3)
53
54 view([0 1 0])
55
56 xlim([-2 2])
57 zlim([-2 2])
58
59 %% c. Type 1 - kz=0 TM                              exx=0.4 eyy=0.2 ezz=-0.5
60 z3TE1 = @(x) sqrt(-0.5-x.^2); % function handle to anonymous function
61 figure(1)
62 subplot(2,3,3);
63 fsurf(z3TE1,'EdgeColor','b','LineWidth',3)
64
65 hold on
66
67 z3TE2 = @(x) -sqrt(-0.5-x.^2);
68 fsurf(z3TE2,'EdgeColor','b','LineWidth',3)
69
70 view([0 1 0])
71 hold on
72 %% c. Type 1 - kz=0 TE                              exx=0.4 eyy=0.2 ezz=-0.5
73 z3TM1 = @(x) sqrt(0.4-2*x.^2); % function handle to anonymous function
74 fsurf(z3TM1,'EdgeColor','r','LineWidth',3)
75
76 hold on
77
```

```
78  z3TM2 = @(x) -sqrt(0.4-2*x.^2);
79  fsurf(z3TM2,'EdgeColor','r','LineWidth',3)
80
81  view([0 1 0])
82
83  xlim([-2 2])
84  zlim([-2 2])
85
86  %% d. Type 2 - kx=0 TE                              exx=-0.4 eyy=-0.2 ezz=0.5
87  z4TE1 = @(y) sqrt(-0.4-y.^2); % function handle to anonymous function
88  figure(1)
89  subplot(2,3,4);
90  fsurf(z4TE1,'EdgeColor','r','LineWidth',3)
91
92  hold on
93
94  z4TE2 = @(y) -sqrt(-0.4-y.^2);
95  fsurf(z4TE2,'EdgeColor','r','LineWidth',3)
96
97  view([0 1 0])
98  hold on
99  %% d. Type 2 - kx=0 TM                              exx=-0.4 eyy=-0.2 ezz=0.5
100 z1TM1 = @(y) sqrt(-0.2+0.4*y.^2); % function handle to anonymous function
101 fsurf(z1TM1,'EdgeColor','b','LineWidth',3)
102
103 hold on
104
105 z4TM2 = @(y) -sqrt(-0.2+0.4*y.^2);
```

```
106 fsurf(z4TM2,'EdgeColor','b','LineWidth',3)
107
108 view([0 1 0])
109
110 xlim([-2 2])
111 zlim([-2 2])
112
113 %% e. Type 2 - ky=0 TE                              exx=-0.4 eyy=-0.2 ezz=0.5
114 z5TE1 = @(x) sqrt(-0.2-x.^2); % function handle to anonymous function
115 figure(1)
116 subplot(2,3,5);
117 fsurf(z5TE1,'EdgeColor','r','LineWidth',3)
118
119 hold on
120
121 z5TE2 = @(x) -sqrt(-0.2-x.^2);
122 fsurf(z5TE2,'EdgeColor','r','LineWidth',3)
123
124 view([0 1 0])
125 hold on
126 %% e. Type 2 - ky=0 TM                              exx=-0.4 eyy=-0.2 ezz=0.5
127 z5TM1 = @(x) sqrt(-0.4+0.8*x.^2); % function handle to anonymous function
128 fsurf(z5TM1,'EdgeColor','b','LineWidth',3)
129
130 hold on
131
132 z5TM2 = @(x) -sqrt(-0.4+0.8*x.^2);
133 fsurf(z5TM2,'EdgeColor','b','LineWidth',3)
```

```
134
135 view([0 1 0])
136
137 xlim([-2 2])
138 zlim([-2 2])
139
140 %% f. Type 2 - kz=0 TM                              exx=-0.4 eyy=-0.2 ezz=0.5
141 z6TE1 = @(x) sqrt(0.5-x.^2); % function handle to anonymous function
142 figure(1)
143 subplot(2,3,6);
144 fsurf(z6TE1,'EdgeColor','b','LineWidth',3)
145
146 hold on
147
148 z6TE2 = @(x) -sqrt(0.5-x.^2);
149 fsurf(z6TE2,'EdgeColor','b','LineWidth',3)
150
151 view([0 1 0])
152 hold on
153 %% f. Type 2 - kz=0 TE                              exx=-0.4 eyy=-0.2 ezz=0.5
154 z6TM1 = @(x) sqrt(-0.4-2*x.^2); % function handle to anonymous function
155 fsurf(z6TM1,'EdgeColor','r','LineWidth',3)
156
157 hold on
158
159 z6TM2 = @(x) -sqrt(-0.4-2*x.^2);
160 fsurf(z6TM2,'EdgeColor','r','LineWidth',3)
161
```

```
162 view([0 1 0])
163
164 xlim([-2 2])
165 zlim([-2 2])
```

A.2. Calculation for Permittivities of Unaxial Hyperbolic Metamaterials

```
%% MATLAB code for calculation of effective permittivities of uniaxial
   hyperbolic metamaterials

clc;clear;close all;
set(0,'defaultAxesFontSize',10);

%% STEP 1: Normal Deposition TiO2 - Refractive Index Data nx, ny, nz from
   Ellipsometer

wl = linspace(400,900,500);

N = xlsread('NTiO2_Single_Layer.xlsx');
wl = N(:,1); %% Measurement Wavelength
n = N(:,2); %% Refractive index of normal TiO2 single layer
k = N(:,3); %% Extinction coefficient of normal TiO2 single layer

figure(1)
plot(wl,n,'Color','[1 0 0]','LineWidth',2);

xlabel('Wavelength (nm)','FontSize',16);
ylabel('Refractive Index (n)','FontSize',16);
title('Refractive Index of Normal TiO_{2} Single Layer','fontsize',16);
L = legend('n','Location','southeastoutside');
set(L,'FontSize',16);

e_real = n.^2 - k.^2; %% Conversion from refractive index to real
```

```
    permittivity e_real
e_img = 2.*n.*k; %% Conversion from refractive index to imaginary
    permittivity e_img

figure(2)
plot(wl,e_real,'Color','[1 0 0]','LineWidth',2);
hold on
plot(wl,e_img,'--','Color','[0 1 0]','LineWidth',2);

xlabel('Wavelength (nm)','FontSize',16);
ylabel('Permittivity (\epsilon)','FontSize',16);
title('Permittivity of Normal TiO_{2} Single Layer','fontsize',16);
L = legend('\epsilon(Real)','\epsilon(Img)','Location','southeastoutside')
    ;
set(L,'FontSize',16);

e_real = interp1(wl,e_real,wl,'pchip'); %% Piecewise Cubic Hermite
    Interpolating Polynomial
e_img = interp1(wl,e_img,wl,'pchip');

%% STEP 2: Cu - Refractive Index Data (From Palik I: pp. 284-285, 207-1823
     nm)

Cu=xlsread('Cu_Single_Layer.xlsx');
wl_cu = Cu(:,1); %% Measurement wavelength
n_cu = Cu(:,2); %% Refractive index n of single Cu layer
k_cu = Cu(:,3); %% Extinction coefficient of single Cu layer

```

```
48 e_cu_real = n_cu.^2 - k_cu.^2; %% Conversion from refractive index to real
       permittivity e_real
49 e_cu_img = 2.*n_cu.*k_cu; %% Conversion from refractive index to imaginary
       permittivity e_img
50
51 figure(3)
52
53 xlabel('Wavelength (nm)','FontSize',16);
54
55 yyaxis left
56 plot(wl_cu,n_cu,'Color','[1 0 0]','LineWidth',2);
57 hold on
58 ylabel('Refractive Index (n)','FontSize',16);
59
60 yyaxis right
61 plot(wl,k_cu,'Color','[0 1 0]','LineWidth',2);
62 ylabel('Extinction Coefficient (k)','FontSize',16);
63
64 title('Refractive Index of Cu Single Layer','fontsize',16);
65 L = legend('n','k','Location','southeastoutside');
66 set(L,'FontSize',16);
67
68 figure(4)
69 plot(wl_cu,e_cu_real,'Color','[1 0 0]','LineWidth',2);
70 hold on
71 plot(wl_cu,e_cu_img,'Color','[0 0 1]','LineWidth',2);
72
73 xlabel('Wavelength (nm)','FontSize',16);
```

```
74 ylabel('Permittivity (\epsilon)','FontSize',16);
75 title('Permittivity of Cu Single Layer','fontsize',16);
76 L = legend('\epsilon(Real)','\epsilon(Img)','Location','southeastoutside')
       ;
77 set(L,'FontSize',16);
78
79 e_CU_real = interp1(wl_cu,e_cu_real,wl,'pchip'); %% Piecewise Cubic
       Hermite Interpolating Polynomial
80 e_CU_img = interp1(wl_cu,e_cu_img,wl,'pchip');
81
82 %% STEP 3: Application of Equations of Biaxial Permittivities - Effective
       Permittivity
83 p = 15/60 % % Fill factor: Cu / Normal TiO2
84
85 e_CU = complex(e_CU_real,e_CU_img);
86 e_NTiO2 = complex(e_real,e_img);
87
88 Exx = (e_CU.*p + e_NTiO2)./(p+1); %% Eq. (2.33)
89 Ezz = (p+1)./((p./e_CU)+(1./e_NTiO2)); %% Eq. (2.34)
90
91 figure(5)
92 plot(wl,real(Exx),'DisplayName','Exx(Real)','LineWidth',1,'Color','[1 0 0]
       ');
93 hold on
94 plot(wl,real(Ezz),'DisplayName','Ezz(Real)','LineWidth',1,'Color','[1 0 1]
       ');
95 hold on
96 plot(wl,imag(Exx),'--','DisplayName','Exx(Img)','LineWidth',2,'Color','[0
```

```
    1 0]');
hold on
plot(wl,imag(Ezz),':','DisplayName','Ezz(Img)','LineWidth',2,'Color','[0 1
    1]');

xlabel('Wavelength (nm)','FontSize',16);
ylabel('Permittivity (\epsilon)','FontSize',16);
title('Permittivity of Normal HMM - Cu / TiO_{2}','fontsize',16);
L = legend('\epsilon_{xx}(Real), \epsilon_{yy}(Real)','\epsilon_{zz}(Real)
    ','\epsilon_{xx}(Img), \epsilon_{yy}(Img)','\epsilon_{zz}(Img)','
    Location','southeastoutside');
set(L,'FontSize',16);

%% STEP 4: Refractive Index using Above Permittivity Results

nx = sqrt((sqrt(real(Exx).^2 + imag(Exx).^2) + real(Exx))/2);
kx = sqrt((sqrt(real(Exx).^2 + imag(Exx).^2) - real(Exx))/2);

nz = sqrt((sqrt(real(Ezz).^2 + imag(Ezz).^2) + real(Ezz))/2);
kz = sqrt((sqrt(real(Ezz).^2 + imag(Ezz).^2) - real(Ezz))/2);

figure(6)
xlabel('Wavelength (nm)','FontSize',16);

yyaxis left
ylabel('Refractive Index (n)','FontSize',16);
hold on
plot(wl,nx,'-','DisplayName','nx','LineWidth',1,'Color','[1 0 0]');
```

```
121 hold on
122 plot(wl,nz,'-','DisplayName','nz','LineWidth',1,'Color','[1 0 1]');
123 hold on
124
125 yyaxis right
126 ylabel('Extinction Coefficient (k)','FontSize',16);
127 hold on
128 plot(wl,kx,':','DisplayName','kx','LineWidth',2,'Color','[0 1 0]');
129 hold on
130 plot(wl,kz,':','DisplayName','kz','LineWidth',2,'Color','[0 1 1]');
131
132 title('Refractive Index of Biaxial HMM - Cu / OAD TiO_{2}','fontsize',16);
133 L = legend('n_{x}, n_{y}','n_{z}','k_{x} ,k_{y}','k_{z}','Location','
      southeastoutside');
134 set(L,'FontSize',16);
```

A.3. Calculation for Permittivities of Biaxial Hyperbolic Metamaterials

```
%% MATLAB code for calculation of effective permittivities of biaxial
   hyperbolic metamaterials

clc;clear;close all;
set(0,'defaultAxesFontSize',10);

%% STEP 1: OAD TiO2 - Refractive Index Data nx. ny, nz from Ellipsometer

wl = linspace(400,900,500);

OAD = xlsread('OADTiO2_Single_Layer.xlsx'); %% Import optical constants of
    single OAD TiO2 layer
wl_oad = OAD(:,1); %% Measurement Wavelength
nx_oad = OAD(:,2); %% Refractive index nx of single OAD TiO2 layer
kx_oad = OAD(:,3); %% Extinction coefficient kx of single OAD TiO2 layer
ny_oad = OAD(:,4); %% Refractive index ny of single OAD TiO2 layer
ky_oad = OAD(:,5); %% Extinction coefficient ky of single OAD TiO2 layer
nz_oad = OAD(:,6); %% Refractive index nz of single OAD TiO2 layer
kz_oad = OAD(:,7); %% Extinction coefficient kz of single OAD TiO2 layer

figure(1)
plot(wl_oad,nx_oad,'Color','[1 0 0]','LineWidth',2);
hold on
plot(wl_oad,ny_oad,'Color','[0 0 1]','LineWidth',2);
hold on
plot(wl_oad,nz_oad,'Color','[1 0 1]','LineWidth',2);
```

```
25
26 xlabel('Wavelength (nm)','FontSize',16);
27 ylabel('Refractive Index (n)','FontSize',16);
28 title('Refractive Index of OAD TiO_{2} Single Layer','fontsize',16);
29 L = legend('n_{x}','n_{y}','n_{z}','Location','southeastoutside');
30 set(L,'FontSize',16);
31
32 ex_oad_real = nx_oad.^2 - kx_oad.^2; %% Conversion from refractive index
      to real permittivity ex_real
33 ex_oad_img = 2.*nx_oad.*kx_oad; %% Conversion from refractive index to
      imaginary permittivity ex_imaginary
34 ey_oad_real = ny_oad.^2 - ky_oad.^2; %% Conversion from refractive index
      to real permittivity ey_real
35 ey_oad_img = 2.*ny_oad.*ky_oad; %% Conversion from refractive index to
      imaginary permittivity ey_imaginary
36 ez_oad_real = nz_oad.^2 - kz_oad.^2; %% Conversion from refractive index
      to real permittivity ez_real
37 ez_oad_img = 2.*nz_oad.*kz_oad; %% Conversion from refractive index to
      imaginary permittivity ez_imaginary
38
39 figure(2)
40 plot(wl_oad,ex_oad_real,'Color','[1 0 0]','LineWidth',2);
41 hold on
42 plot(wl_oad,ey_oad_real,'Color','[0 0 1]','LineWidth',2);
43 hold on
44 plot(wl_oad,ez_oad_real,'Color','[1 0 1]','LineWidth',2);
45 hold on
46 plot(wl_oad,ex_oad_img,'--','Color','[0 1 0]','LineWidth',2);
```

```
47 hold on
48 plot(wl_oad,ey_oad_img,'-','Color','[1 0.8 0]','LineWidth',2);
49 hold on
50 plot(wl_oad,ez_oad_img,':','Color','[0 1 1]','LineWidth',2);
51
52 xlabel('Wavelength (nm)','FontSize',16);
53 ylabel('Permittivity (\epsilon)','FontSize',16);
54 title('Permittivity of OAD TiO_{2} Single Layer','fontsize',16);
55 L = legend('\epsilon_{xx}(Real)','\epsilon_{yy}(Real)','\epsilon_{zz}(Real
       )','\epsilon_{xx}(Img)','\epsilon_{yy}(Img)','\epsilon_{zz}(Img)','
       Location','southeastoutside');
56 set(L,'FontSize',16);
57
58 ex_OAD_real = interp1(wl_oad,ex_oad_real,wl,'pchip'); %% Piecewise Cubic
       Hermite Interpolating Polynomial
59 ex_OAD_img = interp1(wl_oad,ex_oad_img,wl,'pchip');
60 ey_OAD_real = interp1(wl_oad,ey_oad_real,wl,'pchip');
61 ey_OAD_img = interp1(wl_oad,ey_oad_img,wl,'pchip');
62 ez_OAD_real = interp1(wl_oad,ez_oad_real,wl,'pchip');
63 ez_OAD_img = interp1(wl_oad,ez_oad_img,wl,'pchip');
64
65 %% STEP 2: Cu - Refractive Index Data (From Palik I: pp. 284-285, 207-1823
       nm)
66
67 Cu=xlsread('Cu_Single_Layer.xlsx'); %% Import optical constants of single
       Cu layer
68 wl_cu = Cu(:,1); %% Measurement wavelength
69 n_cu = Cu(:,2); %% Refractive index n of single Cu layer
```

```
70 k_cu = Cu(:,3); %% Extinction coefficient of single Cu layer
71
72 e_cu_real = n_cu.^2 - k_cu.^2; %% Conversion from refractive index to real
       permittivity e_real
73 e_cu_img = 2.*n_cu.*k_cu; %% Conversion from refractive index to imaginary
       permittivity e_img
74
75 figure(3)
76
77 xlabel('Wavelength (nm)','FontSize',16);
78
79 yyaxis left
80 plot(wl_cu,n_cu,'Color','[1 0 0]','LineWidth',2);
81 hold on
82 ylabel('Refractive Index (n)','FontSize',16);
83
84 yyaxis right
85 plot(wl_oad,k_cu,'Color','[0 1 0]','LineWidth',2);
86 ylabel('Extinction Coefficient (k)','FontSize',16);
87
88 title('Refractive Index of Cu Single Layer','fontsize',16);
89 L = legend('n','k','Location','southeastoutside');
90 set(L,'FontSize',16);
91
92 figure(4)
93 plot(wl_cu,e_cu_real,'Color','[1 0 0]','LineWidth',2);
94 hold on
95 plot(wl_cu,e_cu_img,'Color','[0 0 1]','LineWidth',2);
```

```
96
97  xlabel('Wavelength (nm)','FontSize',16);
98  ylabel('Permittivity (\epsilon)','FontSize',16);
99  title('Permittivity of Cu Single Layer','fontsize',16);
100 L = legend('\epsilon(Real)','\epsilon(Img)','Location','southeastoutside')
        ;
101 set(L,'FontSize',16);
102
103 e_CU_real = interp1(wl_cu,e_cu_real,wl,'pchip'); %% Piecewise Cubic
        Hermite Interpolating Polynomial
104 e_CU_img = interp1(wl_cu,e_cu_img,wl,'pchip');
105
106 %% STEP 3: Application of Equations of Biaxial Permittivities - Effective
        Permittivity
107 p = 15/60 % Fill factor: Cu / OAD TiO2
108
109 e_CU = complex(e_CU_real,e_CU_img);
110 ex_OAD = complex(ex_OAD_real,ex_OAD_img);
111 ey_OAD = complex(ey_OAD_real,ey_OAD_img);
112 ez_OAD = complex(ez_OAD_real,ez_OAD_img);
113
114 Exx = (e_CU.*p + ex_OAD)./(p+1); %% Eq. (2.35)
115 Eyy = (e_CU.*p + ey_OAD)./(p+1); %% Eq. (2.36)
116 Ezz = (p+1)./((p./e_CU)+(1./ez_OAD)); %% Eq. (2.37)
117
118 figure(5)
119 plot(wl,real(Exx),'DisplayName','Exx(Real)','LineWidth',1,'Color','[1 0 0]
        ');
```

```
hold on
plot(wl,real(Eyy),'DisplayName','Eyy(Real)','LineWidth',1,'Color','[0 0 1]
    ');
hold on
plot(wl,real(Ezz),'DisplayName','Ezz(Real)','LineWidth',1,'Color','[1 0 1]
    ');
hold on
plot(wl,imag(Exx),'--','DisplayName','Exx(Img)','LineWidth',2,'Color','[0
    1 0]');
hold on
plot(wl,imag(Eyy),':','DisplayName','Eyy(Img)','LineWidth',2,'Color','[1
    0.8 0]');
hold on
plot(wl,imag(Ezz),':','DisplayName','Ezz(Img)','LineWidth',2,'Color','[0 1
     1]');

xlabel('Wavelength (nm)','FontSize',16);
ylabel('Permittivity (\epsilon)','FontSize',16);
title('Permittivity of Biaxial HMM - Cu / OAD TiO_{2}','fontsize',16);
L = legend('\epsilon_{xx}(Real)','\epsilon_{yy}(Real)','\epsilon_{zz}(Real
    )','\epsilon_{xx}(Img)','\epsilon_{yy}(Img)','\epsilon_{zz}(Img)','
    Location','southeastoutside');
set(L,'FontSize',16);

%% STEP 4: Refractive Index using Above Permittivity Results

nx = sqrt((sqrt(real(Exx).^2 + imag(Exx).^2) + real(Exx))/2);
kx = sqrt((sqrt(real(Exx).^2 + imag(Exx).^2) - real(Exx))/2);
```

```
ny = sqrt((sqrt(real(Eyy).^2 + imag(Eyy).^2) + real(Eyy))/2);
ky = sqrt((sqrt(real(Eyy).^2 + imag(Eyy).^2) - real(Eyy))/2);
nz = sqrt((sqrt(real(Ezz).^2 + imag(Ezz).^2) + real(Ezz))/2);
kz = sqrt((sqrt(real(Ezz).^2 + imag(Ezz).^2) - real(Ezz))/2);

figure(6)
xlabel('Wavelength (nm)','FontSize',16);

yyaxis left
ylabel('Refractive Index (n)','FontSize',16);
hold on
plot(wl,nx,'-','DisplayName','nx','LineWidth',1,'Color','[1 0 0]');
hold on
plot(wl,ny,'-','DisplayName','ny','LineWidth',1,'Color','[0 0 1]');
hold on
plot(wl,nz,'-','DisplayName','nz','LineWidth',1,'Color','[1 0 1]');
hold on

yyaxis right
ylabel('Extinction Coefficient (k)','FontSize',16);
hold on
plot(wl,kx,':','DisplayName','kx','LineWidth',2,'Color','[0 1 0]');
hold on
plot(wl,ky,':','DisplayName','ky','LineWidth',2,'Color','[1 0.8 0]');
hold on
plot(wl,kz,':','DisplayName','kz','LineWidth',2,'Color','[0 1 1]');

title('Refractive Index of Biaxial HMM - Cu / OAD TiO_{2}','fontsize',16);
```

```
169 L = legend('n_{x}','n_{y}','n_{z}','k_{x}','k_{y}','k_{z}','Location','
        southeastoutside');
170 set(L,'FontSize',16);
```